SECONDARY PARTICULATE MATTER EXCEED PRIMARY EMISSIONS FROM CURRENT GASOLINE VEHICLES: AIR QUALITY AND PUBLIC HEALTH IMPLICATIONS

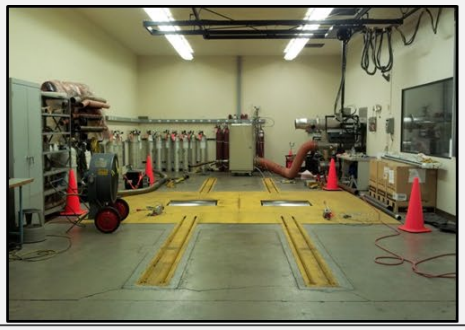

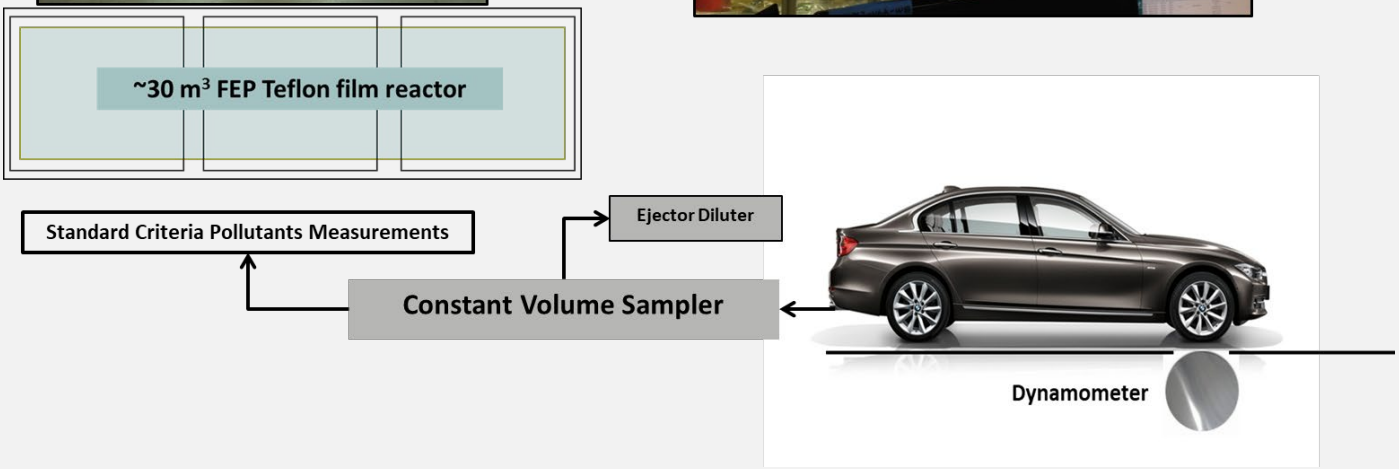

Publication Date Goes Here

CARTEEH

Center for Advancing Research in
Transportation Emissions, Energy, and Health
A USDOT University Transportation Center

Texas A&M Transportation Institute | Georgia Tech College of Engineering | Johns Hopkins Bloomberg School of Public Health | College of Engineering The University of Texas at El Paso | UC Riverside CE-CERT

Disclaimer

The contents of this report reflect the views of the authors, who are responsible for the facts and the accuracy of the information presented herein. This document is disseminated in the interest of information exchange.
The report is funded, partially or entirely, by a grant from the U.S. Department of Transportation's University Transportation Centers Program. However, the U.S. Government assumes no liability for the contents or use thereof.

TECHNICAL REPORT DOCUMENTATION PAGE

1. Report No.	2. Government Accession No.	3. Recipient's Catalog No.
4. Title and Subtitle Secondary Particulate Matter Exceed Primary Emissions from Current Gasoline Vehicles: Air Quality and Public Health Implications		5. Report Date April 2021 6. Performing Organization Code
7. Author(s) Georgios Karavalakis		8. Performing Organization Report No. UCR-01-14
9. Performing Organization Name and Address: CARTEEH UTC University of California Riverside, Center for Environmental Research and Technology 1084 Columbia Avenue, Riverside CA 92507		10. Work Unit No. 11. Contract or Grant No. 69A3551747128
12. Sponsoring Agency Name and Address Office of the Secretary of Transportation (OST) U.S. Department of Transportation (USDOT)		13. Type of Report and Period Final January 1, 2018, to November 30, 2019 14. Sponsoring Agency Code

15. Supplementary Notes

This project was funded by the Center for Advancing Research in Transportation Emissions, Energy, and Health University Transportation Center, a grant from the U.S. Department of Transportation Office of the Assistant Secretary for Research and Technology, University Transportation Centers Program.

The research team would also like to acknowledge funding from the U.S. Department of Agriculture's National Institute of Food and Agriculture Hatch Program (Project No. CA-R-ENS-5072-H, Accession No. 1015963). Niina Kuittinen acknowledges funding from Tampere University Graduate School and The American–Scandinavian Foundation. Niina Kuittinen and Topi Rönkkö acknowledge funding for the Black Carbon Footprint project, granted by Business Finland, Finnish authorities, and Finnish companies.

16. Abstract

A comprehensive study on the effects of photochemical aging on exhaust emissions from a vehicle equipped with a gasoline direct injection engine when operated over seven different driving cycles was assessed using an oxidation flow reactor. Both primary emissions and secondary aerosol production were measured over the Federal Test Procedure, LA92, New European Driving Cycle, US06, and the Highway Fuel Economy Test, as well as over two real-world cycles developed by the California Department of Transportation mimicking typical highway driving conditions. The research team showed that the emissions of primary particles were largely dependent on cold-start conditions and acceleration events. Secondary organic aerosol (SOA) formation also exhibited strong dependence on the cold-start cycles and correlated well with SOA precursor emissions (i.e., non-methane hydrocarbons [NMHCs]) during both cold-start and hot-start cycles (correlation coefficients 0.95–0.99), with overall emissions of about 68–94 mg SOA per g NMHC. SOA formation significantly dropped during the hot-running phases of the cycles, with simultaneous increases in nitrate and ammonium formation as a result of the higher nitrogen oxide (NOx) and ammonia emissions. The findings suggest that more SOA will be produced during congested, slow-speed, and braking events in highways.

Fuel type and composition also affect tailpipe emissions and secondary aerosol production from mobile sources. Therefore, the researchers assessed the influence of gasoline fuels with varying levels of aromatics and ethanol on the primary emissions and secondary aerosol formation from a flexible fuel vehicle equipped with a port fuel injection engine. The vehicle was exercised over the LA92 and US06 driving cycles using a chassis dynamometer. Secondary aerosol formation potential was measured using a fast oxidation flow reactor. Results showed that the high-aromatic fuels led to higher gaseous-regulated emissions, as well as particulate matter, black carbon, and total and solid particle number. The high ethanol content fuel (E78) resulted in reductions for the gaseous-regulated pollutants and particulate emissions. Secondary aerosol formation potential was dominated by the cold-start phase and increased for the high aromatic fuel. Secondary aerosol formation was seen in lower levels for E78 due to the lower formation of precursor emissions using this fuel. In addition, operating driving conditions and aftertreatment efficiency played a major role on secondary organic and inorganic aerosol formation, indicating that fuel properties,

driving conditions, and exhaust aftertreatment should be considered when evaluating the emissions of secondary aerosol precursors from mobile sources.			
17. Key Words Secondary aerosol, Gasoline vehicles, Smog chamber, Oxidation flow reactor, Driving cycles, Ethanol blends, Ammonium nitrate, Primary emissions		18. Distribution Statement No restrictions. This document is available to the public through the CARTEEH UTC website. http://carteeh.org	
19. Security Classif. (of this report) Unclassified	20. Security Classif. (of this page) Unclassified	21. No. of Pages 55	22. Price $0.00

Form DOT F 1700.7 (8-72) Reproduction of completed page authorized

Executive Summary

Secondary organic aerosol (SOA) is formed from the oxidation of diverse non-methane organic gases (NMOGs), ranging in volatility from volatile to intermediate volatility and semivolatile organic compounds (VOCs, IVOCs, and SVOCs, respectively) and comprising a large fraction of the total ambient organic aerosol mass. SOA is known to affect climate change, air quality, and public health. Gasoline motor vehicles are important sources of NMOGs of different volatility classes resulting from incomplete combustion, including aromatic VOCs and long-chain alkanes, which favor the formation of SOA. Both primary emissions and SOA formation are known to be strongly influenced by driving conditions and engine operation, as well as fuel type and composition. Driving operation can significantly affect vehicle emissions and SOA formation, especially from vehicles equipped with gasoline direct injection (GDI) engines, where fuel is directly injected into the combustion chamber leading to enhanced soot formation and other SOA precursor emissions. The effects of fuel type and composition (i.e., ethanol blends and gasoline fuels with varying aromatic contents) can also affect tailpipe emissions and SOA production.

There is limited information of the impacts of different driving operations on SOA formation, including cold-start and hot-start cycles, as well as more aggressive and milder driving cycles or more realistic cycles developed to better mimic actual driving conditions. In addition, there is also limited information available on the fuel effect of SOA formation from current GDI vehicles. The majority of studies with gasoline vehicle exhaust have been conducted with environmental chambers, which are batch reactors capable of capturing the emissions during an entire driving cycle. Less work has been performed with oxidation flow reactors, which are capable of capturing the SOA formation during the transient operation of a vehicle, including cold-start periods, aggressive accelerations and decelerations, idling, and high-speed driving.

This project was separated into two main exercises. The first exercise focused on the driving cycle effects on tailpipe emissions and SOA formation, while the second exercise focused on the fuel effect on primary emission SOA formation. Secondary aerosol was evaluated with a novel oxidation flow reactor, the Tampere Secondary Aerosol Reactor (TSAR). TSAR is an OFR254-type oxidation flow reactor consisting of a residence time chamber, an oxidation reactor, an ozone generator, and an expansion tube connecting the residence time chamber and oxidation reactor. TSAR has been designed to measure potential secondary aerosol formation from rapidly changing emission sources and it has nearly laminar flow conditions. For the first exercise, testing was conducted over several different driving cycles, including regulatory and non-regulatory driving schedules, such as the Federal Test Procedure, the New European Driving Cycle, the LA92, the US06 Supplemental Federal Test Procedure, the Highway Fuel Economy Test Cycle, as well as on two driving schedules developed by the California Department of Transportation to better represent typical driving patterns on California freeways. For the second exercise, testing was conducted over the LA92 and US06 cycles using a flexible fuel vehicle equipped with a port fuel injection engine. Emission measurements were made with three different fuels, including a U.S. Environmental Protection Agency Tier 3 E10 fuel, a high aromatic content E10 fuel, and a E78 blend (contained 78 percent of denatured ethanol). Testing for tailpipe emissions was conducted according to procedures specified in the Code of Federal Regulations, Title 40, Part 86.

For the first exercise, the research team found that the emissions of primary particles were largely dependent on cold-start conditions and acceleration events. During hot-running and hot-start operation, particle emissions dropped significantly as a result of the warmed engine and more efficient operation of the three-way catalyst (TWC). The cold-start period generated significant SOA mass, resulting in about 70–80 percent of the non-refractory mass being SOA. After the TWC warm-up, contribution of SOA decreased to about 5–12 percent of the non-refractory mass while that of nitrate increased from about 15 percent to roughly 60–73 percent. These observations suggest that the warming of the TWC is an important factor in reducing the emissions of SOA precursors. Furthermore, the influence of vehicle emissions on secondary particulate matter (PM) formation, both in terms of concentration and type, changes as the vehicle is driven farther/longer and the TWC is warmed up.

This trend suggests that under stagnant and cold conditions, PM exposure of neighborhood residents can be significantly different than for travelers who are outside the neighborhood. Also, the results suggest that more SOA will be produced during congested, slow-speed, and braking events in highways. For most driving cycles, total nitrate emission factors were 4–14 times higher than SOA. Given the semivolatile nature of ammonium nitrate and its equilibrium with gas-phase ammonia and nitric acid, ambient levels of ammonium nitrate may never reach concentrations significantly higher than SOA unless the ambient temperature and relative humidity levels are favorable. Regardless, since ammonium nitrate formation is suspected to be nitric-acid-limited, controls that further reduce NOx emissions will reduce the formation of inorganic PM and improve regional air quality.

For the second exercise, the primary emission results showed mixed trends across the different fuel and driving cycles. In general, the high-aromatic fuels led to higher gaseous-regulated emissions, as well as PM, black carbon, and total and solid particle number. The use of E78 led to increases in total hydrocarbon (THC), non-methane hydrocarbon (NMHC), carbon monoxide (CO), and nitrogen oxide (NOx) emissions over the LA92 compared to E10 fuels, but decreases in these pollutants over the US06. Particulate emissions, including PM mass, black carbon, and total and solid particle number showed reductions with E78 compared to E10 fuels for both cycles. Secondary aerosol formation potential was strongly dependent on cold-start conditions and especially in the first 200–300 s of the cycle. A strong influence on the formation of secondary aerosol was also seen during the sharp acceleration events of the LA92 and US06 cycles. The higher aromatic E10 fuel produced greater concentrations of secondary aerosol compared to E10, whereas the E78 blend resulted in the least secondary aerosol formation. Ammonium nitrate formation was elevated for both test cycles and fuels, with the E78 blend leading to lower inorganic aerosol formation. Overall, this study showed the beneficial effects on secondary-aerosol-forming potential by using high-ethanol blends in gasoline vehicles and the adverse effects of high aromatic content fuels on primary emissions and secondary aerosol formation. The results in this report also revealed that during cold-start operation, fuel composition will likely play a key role on secondary aerosol production due to the higher generation of secondary aerosol precursors at the tailpipe, and highlighted the importance of using transient conditions and time-resolved characterization in research focusing on secondary aerosols linked with mobile sources.

Overall, this project shows the necessity to rethink and reevaluate the impacts of gasoline vehicles in air quality, by including a wider variety of real-world driving cycles, as well as the measurement of secondary aerosol production. Current technology gasoline vehicles have shown important advances resulting in low gaseous and particulate tailpipe emissions over certification driving cycles using a chassis dynamometer. However, the atmospheric transformation of the emissions leaving the tailpipe is significant, and sometimes secondary aerosol exceeds primary emissions by order of magnitude. It is important for the transportation industry and regulatory agencies to adopt new practices and regulations for a better understanding of secondary aerosols from mobile sources.

Acknowledgments

The authors would like to acknowledge funding from the U.S. Department of Agriculture's National Institute of Food and Agriculture Hatch Program (Project No. CA-R-ENS-5072-H, Accession No. 1015963). Niina Kuittinen would like to acknowledge funding from the Tampere University Graduate School and The American–Scandinavian Foundation. Niina Kuittinen and Topi Rönkkö would like to acknowledge funding for the Black Carbon Footprint project, granted by Business Finland, Finnish authorities, and Finnish companies. The authors would like to thank the late Kurt Bumiller for helping set up the experiment and would like to dedicate this publication to his memory. The authors would also like to thank Mark Villela and Daniel Gomez of The University of California, Riverside, for their contribution in conducting testing for this research program.

Table of Contents

List of Figures

List of Tables

Introduction

On-road gasoline vehicles are an important source of both gaseous and particulate emissions, including nitrogen oxides (NOx), volatile organic compounds (VOCs), black carbon, and particulate matter (PM). Tailpipe emissions of gasoline vehicles also include intermediate volatility organic compounds (IVOCs) and semivolatile organic compounds (SVOCs), including light-molecular-weight monoaromatic hydrocarbons, which are precursors for the production of secondary organic aerosol (SOA) through photooxidation reactions in the atmosphere (Kroll and Seinfeld, 2008; Robinson et al., 2007; Drozd et al., 2019). It has been demonstrated that SOA is the largest component of ambient organic aerosol (OA), followed by primary organic aerosol (POA) emitted as PM from anthropogenic and biogenic sources (Robinson et al., 2007; Jimenez et al., 2009). Previous studies suggest that gasoline vehicles dominate SOA formation in urban areas and significantly exceed the contribution of modern technology diesel vehicles (Gentner et al., 2017; Bahreini et al., 2012; Jathar et al., 2017; Platt et al., 2017).

Vehicle emissions are significantly influenced by driving conditions (Maricq et al., 2017; Herrington et al., 2012). This influence is especially true for vehicles equipped with gasoline direct injection (GDI) engines, where fuel is directly injected into the combustion chamber leading to fuel impingement and localized pool fires, causing diffusive combustion and soot generation (Duronio et al., 2020). These phenomena are more important during cold-start operation, which favors the formation of unburned hydrocarbons from the fuel and lubricating oil, as well as compounds that can act as SOA precursors upon atmospheric dilution and evaporation (Karjalainen et al., 2016). Recent studies have shown elevated tailpipe SVOC emissions from gasoline vehicles during cold-start operation compared to highway cruise conditions (Herrington et al., 2012; Miersch et al., 2019; Zimmerman et al., 2019).

Several studies have investigated the impact of gasoline vehicles on SOA formation using environmental smog chambers, either using transient driving cycles on a chassis dynamometer (Saliba et al., 2017; Vu et al., 2019; Zhao et al., 2017; Platt et al., 2013; Roth et al., 2020) or steady-state and idling driving conditions (Nordin et al., 2013; Liu et al., 2015; Kari et al., 2019; Zhang et al., 2020). The general consensus among these studies is that SOA mass exceeds POA mass (Vu et al., 2019; Nordin et al., 2013; Roth et al., 2020; Gordon et al., 2014). Vu et al. (2019) reported elevated levels of inorganic aerosol formation in the form of ammonium nitrate and several orders of magnitude higher SOA mass than primary PM after introducing the exhaust of four current GDI vehicles operated on the LA92 cycle into a chamber. Zhang et al. (2020) found that during idling conditions representing traffic congestion, higher concentrations of reactive aromatics and alkenes were present in the exhaust resulting in higher SOA formation potential compared to steady-state cruising conditions. Gordon et al. (2014) tested gasoline vehicles of a wide variety of model years and emission certification levels using a smog chamber and showed greater SOA formation for the cold-start tests than the hot-start tests. They also showed lower SOA formation from newer vehicles compared to older technology vehicles. Other studies have shown that more volatile and semivolatile aromatic hydrocarbons present in gasoline are major emitted precursors for SOA formation from GDI vehicles (Roth et al., 2020; Nordin et al., 2013; Du et al., 2018; Peng et al., 2017).

An alternative methodology to batch chamber reactors for the characterization of SOA formation from combustion sources is the potential aerosol mass (PAM) oxidation flow-through reactor, which was developed to simulate concurrent SOA forming potential from highly transient conditions (Kang et al., 2007; Lambe et al., 2011). Oxidation flow reactors can be used in vehicle chassis dynamometer studies to capture the rapidly changing driving conditions during a driving cycle, as well as in field experiments (Cao et al., 2020; Tkacik et al., 2014). A recent investigation of a Euro 6 GDI vehicle using an oxidation flow reactor showed elevated levels of SOA mass during the cold-start New European Driving Cycle (NEDC) compared to the hot-start NEDC, especially during the first 200 s of the urban phase of the test cycle (Simonen et al., 2019). They also showed a comparable amount of ammonium nitrate formation to SOA formation, which is consistent with previous chamber studies of GDI vehicles. Other studies of GDI vehicles utilizing oxidation flow reactors have also shown a strong contribution of cold-start

conditions on SOA formation (Karjalainen et al., 2016; Pieber et al., 2018; Simonen et al., 2017). Zhao et al. (2018) tested 16 gasoline vehicles, including GDI and port fuel injection (PFI) vehicles, over the cold-start LA92 cycle using a PAM reactor and found more SOA formation during cold-start operation because of the substantially higher gaseous organic emissions. They also showed similar SOA formation from GDI and PFI vehicles certified to the same emission standards.

Primary emissions and SOA formation from precursors emitted by motor vehicles can be significantly affected by gasoline composition and properties (Yang et al., 2019a; Yang et al., 2019b; Fushimi et al., 2016; Peng et al., 2017; Roth et al., 2020a). The widespread use of ethanol, the biofuel of choice in the United States, Europe, and other parts of the world, has been shown to reduce the most harmful emissions from gasoline vehicles that have historically utilized multipoint PFI systems and in vehicles with the more efficient GDI engines (Karavalakis et al., 2014a; Maricq et al., 2012; Hays et al., 2013; Durbin, 2007; Clairotte et al., 2013; Timonen et al., 2017). In particular, higher ethanol concentrations used in flexible fuel vehicles (FFVs) designed to run with any ethanol blend up to 83 percent have been shown to offer large reductions in PM and black carbon emissions, as well as reductions in mobile-source air toxic pollutants, such as benzene, toluene, ethylbenzene, xylene (BTEX), and polycyclic aromatic hydrocarbon (PAH) (Karavalakis et al., 2014b; Suarez-Bertoa et al., 2015a; Yang et al., 2019c; McCaffery et al., 2020; Jin et al., 2017; Timonen et al., 2017). Other studies have also demonstrated that the total content and volatility distribution of aromatic hydrocarbons in gasoline will influence tailpipe emissions (Fushimi et al., 2016; Yang et al., 2019a; Yao et al., 2017). High molecular weight and less volatile aromatic hydrocarbons will promote the formation of a wide volatility organic compound range (i.e., semivolatile and intermediate volatility) and primary PM emissions during combustion, and especially during cold-start conditions (Fushimi et al., 2016; Yang et al., 2019a; Yang et al., 2019b; Aikawa et al., 2010).

While considerable attention has been received on the impacts of fuel composition on primary emissions, little is known about the fuel effects on secondary aerosol formation from gasoline vehicles. In addition, the extent to which fuel composition and properties affect SOA formation is not always clear. Studies have looked into the direct evaporation of fuels to better understand the effect of fuel properties on SOA formation (Jathar et al., 2013; He et al., 2020). While this approach is useful, it often neglects the complex combustion processes, including the formation pathways of SOA precursors that are not necessarily present in the fuel in considerable amounts, or the potential interactions of fuel properties that can affect the emissions of these species. Roth et al. (2020a) and Yang et al. (2019a) showed that match-blended ethanol fuels in low concentrations with high levels of heavier aromatics will likely increase VOC precursor emissions from GDI vehicles operated on the LA92 cycle, and subsequently SOA production due to the higher heat of the vaporization of ethanol, which will lead to the cooling of the cylinder environment, slowing fuel evaporation and increasing fuel impingement. Peng et al. (2017) also reported that gasoline fuels with higher aromatic levels will increase VOC precursor emissions and contribute to higher SOA production when they introduced the exhausts of PFI and GDI vehicles into an environmental chamber. Different studies, however, utilizing higher ethanol blends have reported reductions in SOA production from FFVs (Suarez-Bertoa et al., 2015b; Roth et al., 2020b; Gramsch et al., 2018; Timonen et al., 2017). For example, Roth et al. (2020b) proposed that the oxygen content and the dilution of aromatics in E30 and E78 blends were the dominant factors for the lower precursor emissions and the reduced SOA formation from the aged emissions from two FFVs operated over the LA92 cycle when introduced into an environmental chamber. Similarly, Timonen et al. (2017) found reductions in precursor emissions and SOA formation as the ethanol content increased from E10 to E85 and E100 on a FFV operated over the NEDC with the use of a PAM reactor.

For the first part of this study, the primary emissions and SOA formation potential from a current GDI vehicle were assessed, after introducing its dilute exhaust into an oxidation flow reactor and when operating on different driving cycles. A mixture of cold-start and hot-start certification driving cycles used in the United States and Europe was employed, as well as real-world non-regulatory driving cycles that were developed to mimic driving conditions

in California highways. This study is one of very few studies focusing on the effects of multiple driving conditions, including cold start, hot start, aggressive driving, and high-speed driving, on SOA formation from a GDI vehicle.

For the second part of this study, it was identified that while numerous studies utilized oxidation flow reactors to investigate SOA formation from motor vehicles (Kuittinen et al., 2021; Cao et al., 2020; Simonen et al., 2019; Pieber et al., 2018; Karjalainen et al., 2016; Zhao et al., 2018), there is only one vehicle study using an oxidation flow reactor that investigated the effects of ethanol blending on SOA formation (Timonen et al., 2017). The purpose of this study is the transient characterization of the potential for secondary aerosol formation from exhaust emitted by a modern PFI FFV fueled with two E10 fuels with different aromatic contents and a E78 blend when operated over the LA92 and US06 cycles. This study also reports the primary gaseous and particulate emissions, as well as the secondary aerosol formation potential as a function of fuel type and driving conditions.

Effects of Driving Conditions on Secondary Aerosol Formation from a GDI Vehicle Using an Oxidation Flow Reactor

Methodology

Test Vehicle and Driving Cycles

Testing was performed on a 2016 model year passenger car equipped with a 2.4-liter, 4-cylinder, wall-guided fuel injection system, and a three-way catalyst (TWC), and operated with an overall stoichiometric air-fuel ratio. The engine had a rated horsepower of 185 hp at 6000 rpm, a torque of 178 ft-lb at 4000 rpm, and a compression ratio of 10:1. The vehicle was certified to meet the California LEVIII SULEV 30 emission standard and had accumulated 31406 miles. Testing was performed with a typical California E10 fuel.

The vehicle was exercised in duplicate runs over several different driving cycles, including regulatory and non regulatory driving schedules. Testing was conducted over the Federal Test Procedure (FTP), the NEDC, the LA92, the US06 Supplemental FTP, and the Highway Fuel Economy Test (HWFET) cycle. In addition, two driving schedules developed by the California Department of Transportation (Caltrans) to better represent typical driving patterns on California freeways were employed. The cycles (referred to as Caltrans 1 and Caltrans 2) were derived from field driving data representative of freeway, arterial, collector road, and local driving, and traffic congestion levels typically found on Los Angeles freeways. More information about these test cycles are provided in the Supplementary Material (SM) (Figure SM1).

Emission Testing

Gaseous and particulate emission measurements were conducted in The University of California, Riverside, (UCR) Bourns College of Engineering's Center for Environmental Research and Technology's (CE-CERT's) Vehicle Emissions Research Laboratory (VERL), on a Burke E. Porter 48-inch single-roll electric dynamometer. A Pierburg Positive Displacement Pump-Constant Volume Sampling (PDP-CVS) system was used to obtain standard bag measurements for total hydrocarbons (THCs), carbon monoxides (CO), nitrogen oxides (NOx), non-methane hydrocarbons (NMHCs), and carbon dioxides (CO_2). All gaseous emissions were determined according to U.S. Environmental Protection Agency (EPA) protocols for light-duty emission testing as given in the Code of Federal Regulations (CFR), Title 40, Part 86. Tailpipe real-time soot or black-carbon emissions were measured using an AVL Micro-Soot Sensor (MSS), which was further diluted by an additional dilutional tunnel. Particle size distributions were obtained using an Engine Exhaust Particle Sizer (EEPS) spectrometer in parallel with the MSS. The EEPS (TSI 3090, firmware version 8.0.0) was used to obtain real-time, second-by-second size distributions between 5.6 and 560 nm. Particles were sampled at a flow rate of 10 L/min, which is considered high enough to minimize diffusional losses. The dilution factor in the constant volume sampling (CVS) compared to the raw exhaust was a factor of 8.2–15.5.

Photooxidation Experiments

A novel oxidation flow reactor, the Tampere Secondary Aerosol Reactor (TSAR) was installed to the setup following an ejector diluter and was utilized to study secondary aerosol formation potential during transient driving conditions. TSAR is an OFR254-type oxidation flow reactor consisting of a residence time chamber, an oxidation reactor, an ozone generator, and an expansion tube connecting the residence time chamber and oxidation reactor. Mass flow controllers were applied for flow control. TSAR has been designed to measure potential secondary aerosol formation from rapidly changing emission sources and it has nearly laminar flow conditions. In TSAR, the diluted exhaust is mixed with ozone, and the relative humidity (RH) of the sample is increased by mixing it with humidified air. The CVS and ejector diluter combined with dilution by ozone and humidified air flows resulted in total dilution of the sample by factors of 45–172 before entering the TSAR. The sample then passed through a residence time tube before entering an oxidation region where it was exposed to 254 nm ultraviolet (UV) radiation, which induced the production of hydroxyl (OH) radicals through the photolysis of ozone in the presence

of H_2O. The precursor gases present in the exhaust reacted with OH or O_3 to produce lower volatility molecules that then transferred to particle phase and produced secondary aerosol. The experimental setup with the TSAR is described in detail in SM, and detailed information about the TSAR is provided by Simonen et al. (2017, 2019).

An average photooxidation timescale of 6.4 days was explored in this study (Table SM1, SM). The photooxidation timescale falls within the timescales found to simulate peak SOA formation by Tkacik et al. (2014) of 2–3 days, Ortega et al. (2016) of 1–11 days, Saha et al. (2018) of 2–10 days, and Liu et al. (2019) of 1–3 days. Because the photooxidation timescale varied within a drive cycle (lowest during cold starts, see SM) and because adjusting the conditions was not possible within a cycle, the same conditions were applied for all cycles. The OH exposure and corresponding atmospheric age of the sample after oxidation were estimated by applying a chemical reaction model, which considers OH suppression in the TSAR, similarly to Simonen et al. (2017).

The mini Aerodyne Aerosol Mass spectrometer (mAMS), equipped with a compact time-of-flight mass spectrometer mass resolution (i.e., m/Δm with m being the nominal m/z and Δm the full width at half-maximum) of about 1100 and mass accuracy better than 20 ppm, sampled downstream of the flow reactor to determine the non-refractory (NR) composition (OA, sulfate, nitrate, and ammonium) of the submicron aerosol particles (Jayne et al., 2000; Vu et al., 2016). Aerosol particles were sampled only in the mass spectrum mode, with a 7–8 s time resolution. Data from the mAMS were analyzed using Wavemetrics Igor Pro (squirrel ToF-AMS analysis toolkit version 1.60 with PIKA module 1.20) following standard procedures outlined in previous studies (Bahreini et al., 2012b). Given the variable concentration of CO_2 in the vehicle exhaust, gas-phase background CO_2 was subtracted from the OA mass spectra using the measured gas-phase CO_2 concentrations from the CVS and the recommendation by Collier and Zhang (2013). Except for ammonium, high-resolution analysis of the mass spectra was used to generate the mass concentration of the other species. A composition-dependent collection efficiency factor was used to correct for particle bounce on the vaporizer (Middlebrook et al., 2012). Information about the methods used to determine the hydrocarbon-like organic aerosol (HOA) and the oxidation state of OA is shown in SM. In this study, SOA was determined as the difference between total measured organics and the estimated HOA by mAMS. It is impossible to distinguish between SOA that is formed from oxidation of primary HOA and those formed from gas-to-particle partitioning of low-volatility gaseous oxidation products.

The particulate mass of the aged aerosol (i.e., the aerosol sample treated with TSAR) was measured by electrical low-pressure impactor (ELPI+, Dekati Ltd.). The aerosol mass was calculated by integrating the size distribution over stage 3–7, corresponding to particle aerodynamic cut-off diameters between 30 and 604 nm. In the absence of full composition measurements of the primary aerosols, unit density of 1 g/cm^3 was used in the mass calculations, similar to the approach taken previously (Simonen et al., 2017; Simonen et al., 2019).

Results

Particle Size Distributions

Figure 1 presents the average particle size distributions and real-time soot mass emissions for the test vehicle when operated on the NEDC, LA92, Caltrans 1, and Caltrans 2 cycles. The particle size distribution data for the FTP are shown in Figure SM4 (SM). Particle size data for the US06 and HWFET cycles were not available, but their soot mass emissions are shown in Figure SM5 (SM). For the FTP, LA92, and NEDC cycles, the cold-start phase dominated the soot mass emissions and accumulation mode particle concentrations. During the first 50 s of these cycles, accumulation mode particle populations ranged between 40–200 nm in diameter, with geometric mean diameter (GMD) of the number size distribution varied between 20–110 nm. For the FTP and NEDC, particles gradually shifted to lower sizes (GMD of 30–60 nm) and concentrations after 100 s in the cycle. Overall, the cold-start cycles exhibited a decidedly bimodal particle size distribution across all phases. The accumulation mode dominated the particle size distribution, with lower concentrations of nucleation mode particle peaks centered around 20–30 nm in diameter. The elevated accumulation mode particle concentrations and soot mass emissions during the cold-start period can be attributed to the incomplete fuel vaporization when directly injected into the cold

combustion chamber surfaces and the cold piston crown, which can lead to increased fuel impingement and localized pockets of liquid fuel (pool fires) (Duronio et al., 2020; Cheng et al., 2001; Yang et al., 2019). This fuel will burn in diffusion flames where soot formation initially takes place. Further, incomplete combustion byproducts, such as semivolatile hydrocarbon fragments, will be less efficiently oxidized, due to the TWC being below its light-off temperature. Accumulation mode particles in GDI engines consist of carbonaceous chain agglomerates formed in local rich-fuel zones. The results agree with previous studies with GDI vehicles that have shown substantially higher accumulation mode particles and soot mass emissions during cold-start conditions (Yang et al., 2019; Chen et al., 2017).

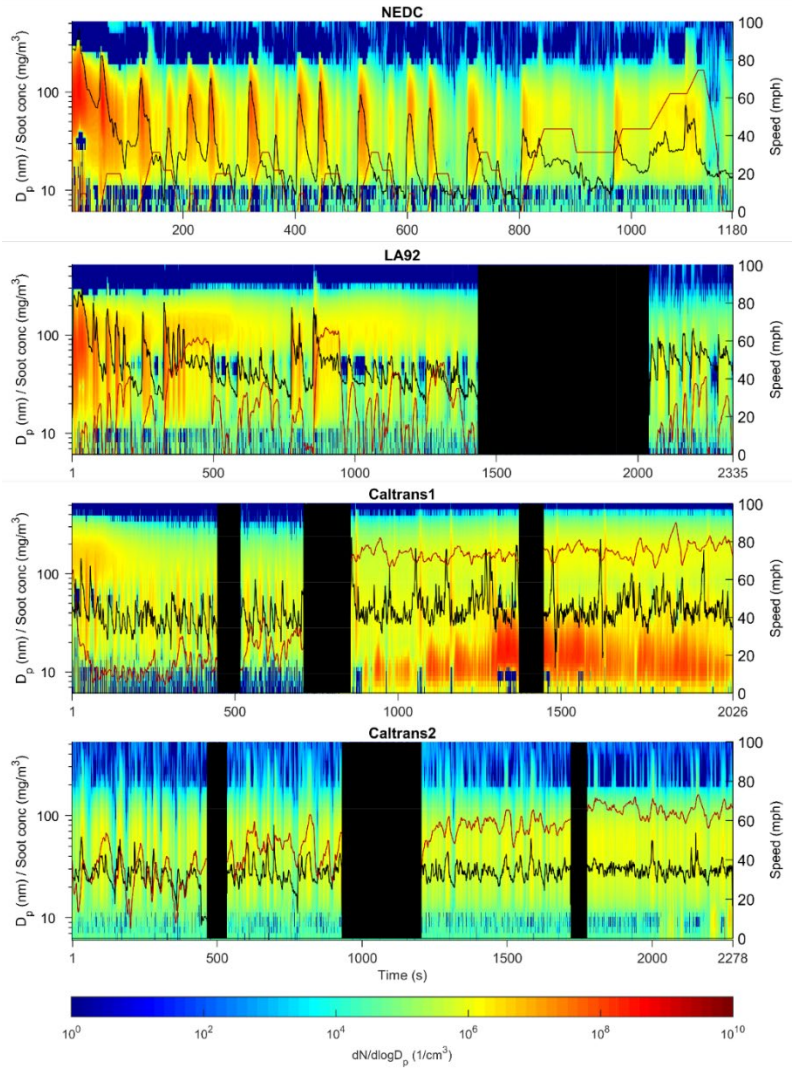

Note: Particle size distributions measured by EEPS are shown as a heatmap together with soot concentrations measured by MSS (black line, left y-axis; note the logarithmic scale), and vehicle speed (red line, right y-axis). The values are corrected to represent tailpipe concentrations. Transition and soak periods between different phases of the cycle have been omitted. The concentrations shown have been corrected by dilution to represent tailpipe concentrations. The results are averages from repeatable duplicate runs, except for Caltrans 1, which was a single run.

Figure 1. Heatmap of particle size distributions measured by EEPS, soot concentrations measured by MSS, and vehicle speed.

Accumulation mode particle concentrations and soot mass emissions significantly decreased during the urban and hot-start phases of the FTP and LA92, but not during the entire duration of the urban driving cycle (UDC) segment of NEDC. For the UDC segment, accumulation mode particles were clearly found in relatively high concentrations during the acceleration hills of the UDC, with broader sizes ranging from 40–110 nm. Nucleation mode particles in modal sizes of 5–15 nm were also present throughout the duration of the UDC, owing their formation to the acceleration events, as transients disrupt the control of the global air-fuel ratios and exacerbate the heterogeneity of the cylinder charge. For the extra-urban driving cycle (EUDC) segment, both nucleation and accumulation mode particles were observed in lower concentrations than the UDC, with the major peaks appearing at the two main acceleration hills of the EUDC. Nucleation mode particles were likely derived mostly from semivolatile hydrocarbon species via condensation; however, nucleation mode particles can also have non-volatile fraction. Previous studies have indicated that GDI engines can emit small non-volatile particles that can act as condensation nuclei for semivolatile exhaust compounds (Pirjola et al., 2015; Sgro et al., 2012). For the FTP and LA92 cycles, accumulation mode particle concentrations dropped for the urban and hot-start phases as a result of the engine warm-up, which led to steadily higher combustion temperatures and better fuel vaporization, avoiding pool fires responsible for soot formation. While accumulation mode particle populations were found in lower levels than those of the UDC, they spiked during the steeper acceleration periods of both the FTP and LA92 urban and hot-start phases. For the LA92, the GMD of the distribution remained between 50–120 nm until the hot-start phase during which GMD was generally at 40–50 nm. For the hot-start Caltrans cycles, particle concentrations across all size ranges were lower than the cold-start cycles. For the Caltrans 1 cycle, the nucleation mode dominated the particle size distribution profile, showing excessive populations of smaller nucleation mode particles in the 5–30 nm size range over the high-speed phase (GMD of around 20 nm) compared to the low-speed phase (GMD decreased from 150 nm to 40 nm). Higher populations of accumulation mode particles were seen for Caltrans 2, with the nucleation mode particles being practically eliminated, except for some spikes during accelerations towards the end of the high-speed phase and GMD varied between 15–45 nm over the cycle. The intense nucleation burst during the high-speed and load conditions was likely due to the higher exhaust gas temperature and the enhanced formation of sulfuric acid (Karjalainen, 2014). Maricq et al. (2017) suggested that at high-speed conditions of GDI vehicles, the time available for soot maturation is reduced, since the engine runs slightly rich to produce soot. These conditions could also promote the formation of small nanoparticles from semivolatile hydrocarbons instead of their condensation onto soot particles (Maricq et al., 2017).

Aged Aerosol

Figure 2 and Figure 3 show the real-time evolution of aged aerosol PM, OA, HOA, and sulfate, nitrate, and ammonium ions, as well as tailpipe NOx and NMHC emissions during operation over the LA92, NEDC, Caltrans 1, and Caltrans 2 cycles, respectively. Results for the FTP, HWFET, and US06 cycles are shown in Figure SM6–SM8, SM. For comparison purposes, primary PM corrected with time-delay of the signal in the TSAR reactor are also presented. For both the LA92 and NEDC, aged PM were significantly higher than primary PM during the entire duration of the test cycle. The cold start, and especially the first 150–200 s, showed a pronounced influence on the formation of aged PM, being more than two times higher in concentration than primary PM. The cold-start period also showed significantly higher concentrations of both primary and aged PM when compared to the hot-running phases of both cycles, with aged PM formation being affected by vehicle acceleration events. Both hot-start Caltrans cycles followed the same patterns as the cold-start cycles and showed substantially higher aged PM concentrations than primary PM. The larger difference between primary and aged PM was likely due to the absence of a cold-start period for these cycles, which led to more complete combustion and lower formation of in-cylinder soot emissions, as seen in Figure 1. Overall, the results agree with previous studies on gasoline vehicles that have reported higher aged PM than primary PM emissions (Karjalainen et al., 2016; Vu et al., 2019; Simonen et al., 2019; Pieber et al., 2018; Zhao et al., 2018). For Caltrans 1, the low-speed phase that represents congested highway driving resulted in elevated concentrations of aged PM compared to the relatively steady-state high-speed highway driving conditions. Similar findings with the TSAR have been previously reported, where lower concentrations of aged PM were found during long steady-state driving (Simonen et al., 2017). For the more

aggressive Caltrans 2 cycle, overall aged PM were seen in higher concentrations than those of Caltrans 1, as a result of the heavier acceleration conditions of this cycle. The lower speed but more aggressive first phase of Caltrans 2 generated more aged PM than the higher speed but less aggressive phase 2. Phase 4 with the highest speed profile showed generally more aged PM than phase 3 that had slightly lower speed conditions.

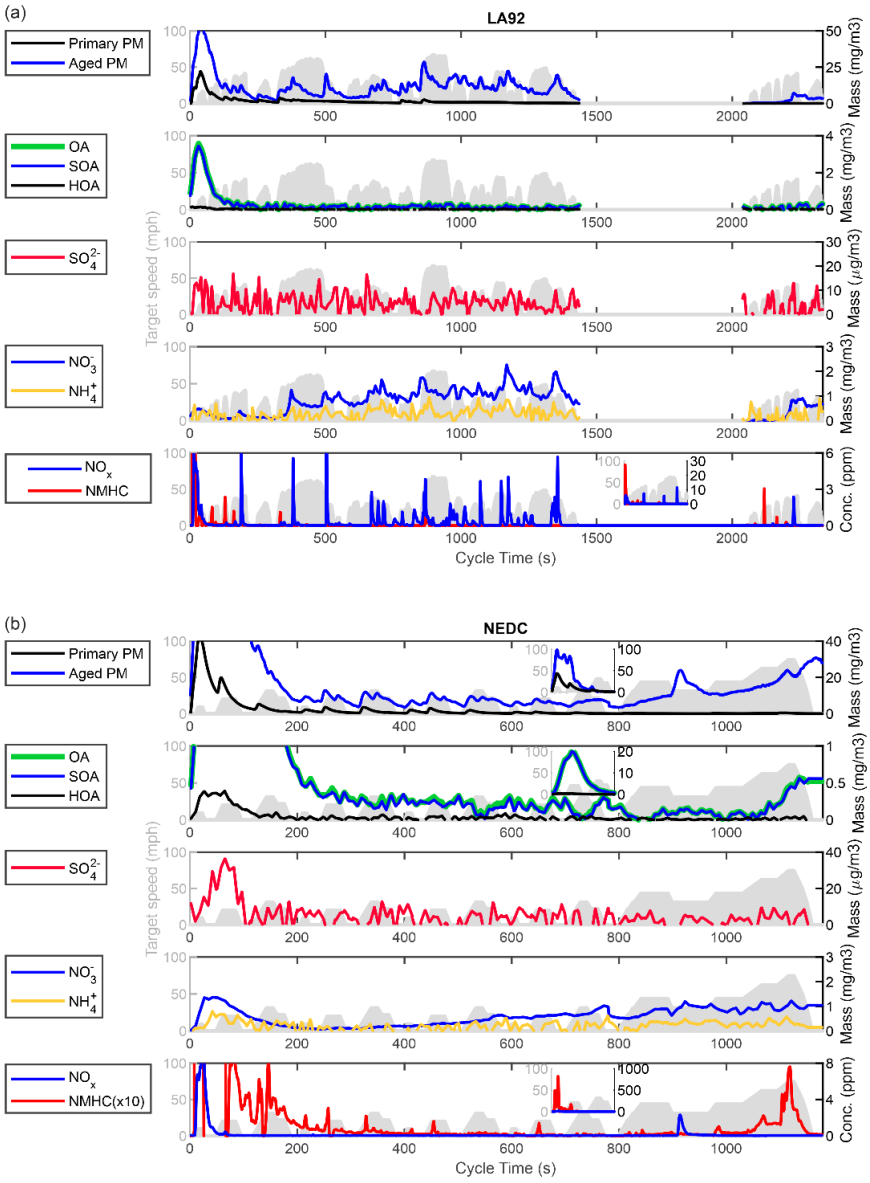

Note: This figure presents the time-series of primary (measured by EEPS) and aged (measured by ELPI+) PM, SOA, sulfate, ammonium, and nitrate ions (measured by mAMS), and tailpipe NMHC and NOx concentrations over the LA92 and NEDC cycles. For comparison, primary PM measured by EEPS are shown corrected with time convolution caused by residence time in the TSAR chamber. Subfigures inside the plots show concentrations during the cold starts, for NEDC during the first 200 s, and for LA92 during the first 600 s of the cycle. The concentrations shown have been corrected by dilution to represent tailpipe concentrations. The results are averages from repeatable duplicate runs, except for Caltrans 1, which was a single run.

Figure 2. Time-series of primary and aged PM, SOA, sulfate, ammonium, and nitrate ions, and tailpipe NMHC and NOx concentrations over the LA92 and NEDC cycles.

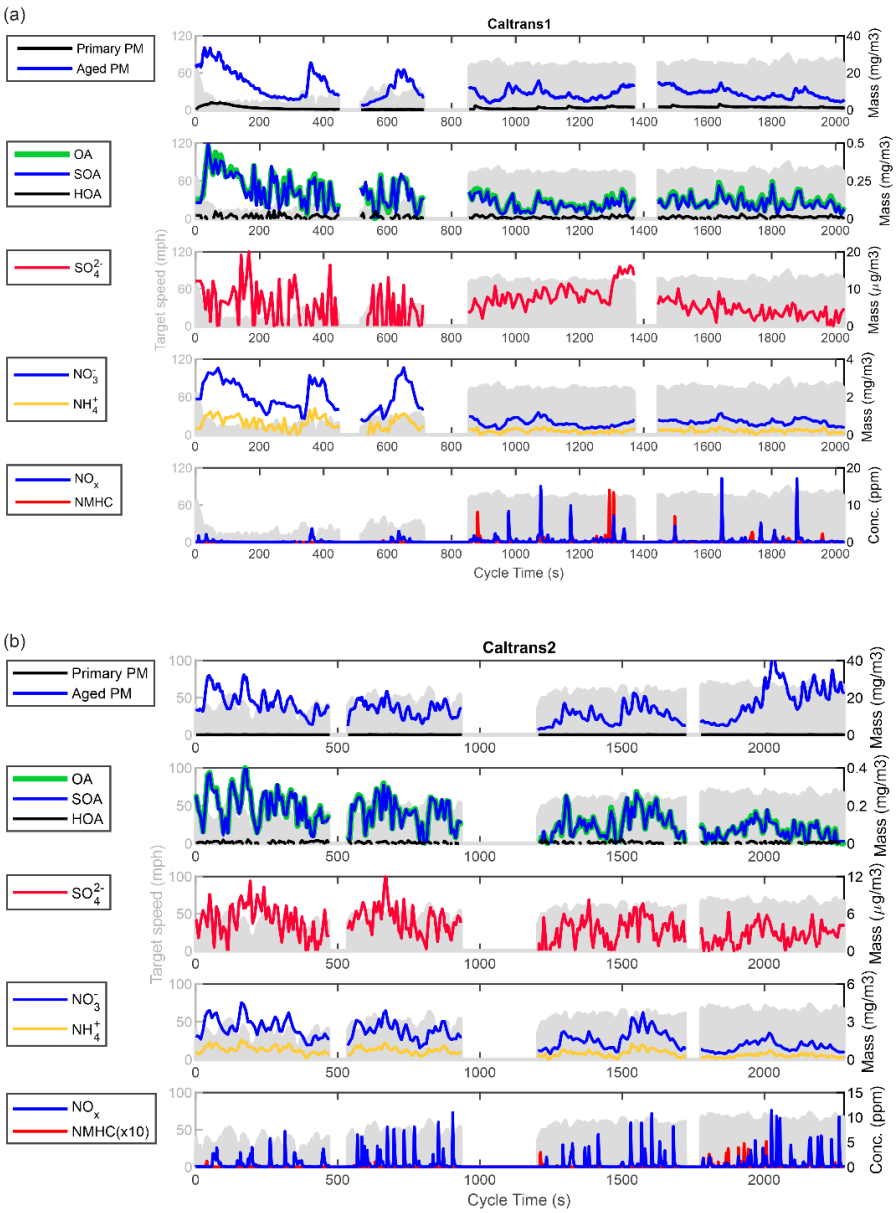

Note: This figure presents the time-series of primary (measured by EEPS) and aged (measured by ELPI+) PM, SOA, sulfate, ammonium, and nitrate ions (measured by mAMS), and tailpipe NMHC and NOx concentrations over the Caltrans 1 and Caltrans 2 cycles. For comparison, primary PM measured by EEPS are shown corrected with time convolution caused by residence time in the TSAR chamber. The concentrations shown have been corrected by dilution to represent tailpipe concentrations. The results are averages from repeatable duplicate runs, except for Caltrans 1, which was a single run.

Figure 3. Time-series of primary and aged PM, SOA, sulfate, ammonium, and nitrate ions, and tailpipe NMHC and NOx concentrations over the Caltrans 1 and Caltrans 2 cycles.

The driving cycle showed a strong influence on the time-series of SOA formation. The largest contributor to SOA production was the first 200 s of the cold-start periods. During the cold-start period for both the LA92 and NEDC cycles, as well as for the FTP (Figure SM6, SM), SOA mass was considerably higher than during the hot-running phases, and correlated well (correlation coefficient of 0.99) with the tailpipe NMHC emissions (Figure SM9) despite the fact that not all species of the NMHCs are SOA precursors. Cold-start measurements indicated an average

formation of 86 mg SOA/g NMHC while the overall weighted SOA formation in these cycles was lower at 68 mg SOA/g NMHC. Higher SOA formation from gasoline vehicles during the cold-start operation has been reported in other studies using oxidation flow reactors (Karjalainen et al., 2016; Simonen et al., 2019; Pieber et al., 2018). The higher SOA formation during the cold-start period can be ascribed to the TWC as being below its light-off temperature and therefore not efficient in oxidizing unburned fuel and lubricant oil hydrocarbon fragments and other VOCs, which are all known as SOA precursor emissions (Drozd et al., 2019). Similar observations were made by Saliba et al. (2017) when they found that cold-start THC emissions from super-ultra-low emission vehicles (SULEVs) equaled on average 101.5 mi of hot-stabilized driving. Typical gasoline fuels are dominated by single-ring aromatics in the range of C6–C12, with benzene, toluene, ethylbenzene, and xylenes being the predominant species, as well as straight-chain and branched alkanes (smaller than C8). Emissions of the small aromatic species can be attributed to unburned fuel or partially burned heavier aromatics, which are usually more difficult to evaporate than other hydrocarbon compounds (i.e., paraffins, olefins, etc.) during cold-start conditions in GDI combustion (Yang et al., 2019b). The detailed composition of the NMHC was not measured; however, consistent with previous studies, the results suggest a greater contribution of light aromatics in SOA formation during cold-start conditions that led to higher SOA formation per mass of NMHC (Roth et al., 2020; Nordin et al., 2013; Peng et al., 2017).

Although the maximum OA values changed during the cold-start period depending on the drive cycle, the oxidation characterization of OA remained similar. As seen in Figure SM10a, f_{44} (fraction of ions related to highly oxygenated organic species, CO_2^+) and f_{43} (fraction of ions predominantly related to mildly oxygenated ions, $C_2H_3O^+$) values during this period in all three cycles occupy a similar space, previously attributed to SV-OOA and LV-OOA (Ng et al., 2010). At the peak of the emissions, the average oxidation state of carbon (OS_c) was in the range of about -0.84 to -0.21, while at lower OA concentrations, OS_c reached values as high as about 0.5 (Figure SM10b). These average OS_c are significantly higher than what has been observed for fresh and primary vehicle exhaust (with OS_c of around -1.65), indicating that OA sampled through TSAR were not similar in composition to that of primary OA (Kroll et al., 2011; Aiken et al., 2008). The OS_c values in the peak of OA concentrations from the FTP and NEDC cycles are, however, consistent with ambient values in Mexico City, as well as the SV-OOA factor in the ambient data (Kroll et al., 2011; Aiken et al., 2008), suggesting that during the cold-start period of these driving cycles, oxidation conditions of TSAR led to formation of SOA that is representative of those found in urban environments. During the LA92, average OS_c was higher (-0.5 to 0.5), consistent with the more aged ambient OA and LV-OOA factor of the ambient data (Kroll et al., 2011; Aiken et al., 2008). These observations are consistent with a slightly higher OH exposure during the cold-start phase of LA92 compared to the corresponding phase in the FTP and NEDC cycles due to relatively lower emissions of NMHC in LA92 (5 equivalent days in LA92 versus 3.9–4.3 equivalent days in FTP and NEDC, assuming a daily average OH of 1.5×10^6 molecule/cm^3) (Figure SM2b).

For all the cold-start cycles, SOA formation, as well as SOA precursor emissions (i.e., NMHC), were at least an order of magnitude lower for the hot-running phases compared to the cold-start phase. Higher combustion and exhaust temperatures, and the higher catalytic activity of the TWC, resulted in reduced formation and the more efficient oxidation of the emitted precursors for the hot-running phases. A sharp peak of SOA formation was detected at the end of the NEDC during the last acceleration that correlates well with the peak of tailpipe NMHC emissions. Similar results were observed in previous studies with gasoline vehicles over the NEDC (Simonen et al., 2019; Simonen et al., 2017).

For both Caltrans cycles, SOA formation was found to depend on driving conditions and oxidation conditions. For Caltrans 1, SOA formation per miles driven was factors of 1.4–3.2 higher during the first two phases that primarily represented slow driving in congested highways than the phases representing steady-state high-speed driving, despite the lower NMHC emissions for the first two phases. However, as shown in Figure SM2 (SM), the steady-state high-speed phase had significantly lower OH exposure due to higher CO emissions (Figure SM11), which likely contributed to the lower SOA formation. Similar to Caltrans 1, the first two phases of Caltrans 2 that

were characterized by more aggressive, frequent braking, and lower-speed driving resulted in factors of 2.2–3.6 more SOA formation compared to the higher speed and free-flow driving of the last two phases of the cycle. Because of the similarity in OH exposure between different phases of Caltrans 2, the higher SOA formation in the more aggressive driving phases suggests higher emissions of SOA precursors during such driving conditions.

Time-series plots of aerosol sulfate indicate relatively low concentrations for all driving cycles and generally its formation was associated with vehicle accelerations. The sulfate aerosol comprised a rather small portion of the total secondary aerosol (less than 1 percent). This small portion is primarily a consequence of the very tight sulfur standards for gasoline fuels and the very low sulfur levels in lubricant oils. However, even low levels of sulfur in the fuel and the lubricant oil can be stored in the TWC and subsequently released as SO_2 to prompt the formation of SO_3 and the further production of sulfate complexes (Simonen et al., 2019; Maricq et al., 2002). For the LA92 and NEDC, sulfate was seen in higher concentrations (about a factor of two) than the Caltrans cycles, as a result of the cold-start period, which negatively affects fuel impingement and evaporation and increases lubricant oil viscosity, leading to more PM and unburned hydrocarbons. This phenomenon was particularly noticeable over the NEDC, where sulfate aerosol showed elevated concentrations during the first 100 s of the cycle. It is therefore assumed that lubricant oil, in addition to fuel fragments, may have an important role in the emissions of secondary aerosol precursors during the cold-start operation of GDI engines. For the Caltrans cycles, sulfate aerosol was higher during the lower speed and load conditions, suggesting higher fuel and lubricant oil consumption during congested highway conditions.

There was substantial formation of nitrate for all driving cycles, which exceeded the SOA formation except during the cold-start periods. This finding is in good agreement with previous studies on gasoline vehicles that have reported elevated secondary inorganic aerosol production using either smog chambers or oxidation flow reactors (Vu et al., 2019; Roth et al., 2020; Tkacik et al., 2014). For example, Vu et al. (2019) showed higher inorganic aerosol mass than SOA when they tested four GDI vehicles over the LA92 using an environmental chamber, whereas Tkacik et al. (2014) demonstrated an increased production of ammonium nitrate by a factor of two compared to SOA when they deployed a PAM reactor in a highway tunnel in Pittsburgh. The measured nitrate in the current study could stem from the presence of inorganic (i.e., ammonium nitrate) and organic nitrates; therefore, it is of interest to understand the contribution of either class of species to the measured aerosol nitrate. The observed ratios of two main fragments of nitrate in mAMS, NO^+/NO_2^+ (R_{obs}), during the cold-start cycles, were predominantly in the range of expected values for ammonium nitrate (RAN), suggesting that most of the times, and especially when the nitrate mass fraction relative to OA was greater than about 20 percent, the observed nitrate was due to the formation of ammonium nitrate (Figure 4a). However, as seen in Figure 4b, at moderate absolute concentrations of nitrate and high concentrations of OA (i.e., larger markers in Figure 4(a-b)) during the cold-start, R_{obs} was significantly higher than RAN. This observation suggests that in the beginning of the cold-start cycles, conditions were conducive for an organonitrate formation given the high co-emission of NOx and NMHCs. During the Caltrans cycles, the overall concentrations of OA were significantly lower than during the first phase of the cold-start cycles, and the nitrate mass fractions relative to OA reached values greater than 70 percent. During these times, R_{obs} was predominantly in the range of RAN, indicating that the fate of the emitted NOx during high-speed driving of the hot cycles was dominated by oxidation to nitric acid (instead of reactions with peroxy radicals to form organonitrates) and eventual partitioning to aerosols as inorganic nitrate (Figure 5). Overall, there is a good agreement between tailpipe NOx emissions during acceleration and high-speed conditions and nitrate formation. Acceleration events and dynamic driving resulted in higher combustion temperatures and enhanced formation of NOx. Therefore, high-speed highway conditions and aggressive urban driving will likely affect the formation of secondary nitrate aerosol. An exception was observed for the low-speed phase of Caltrans 1, where nitrate showed significantly higher formation compared to the high-speed phase of the cycle despite tailpipe NOx emissions being low.

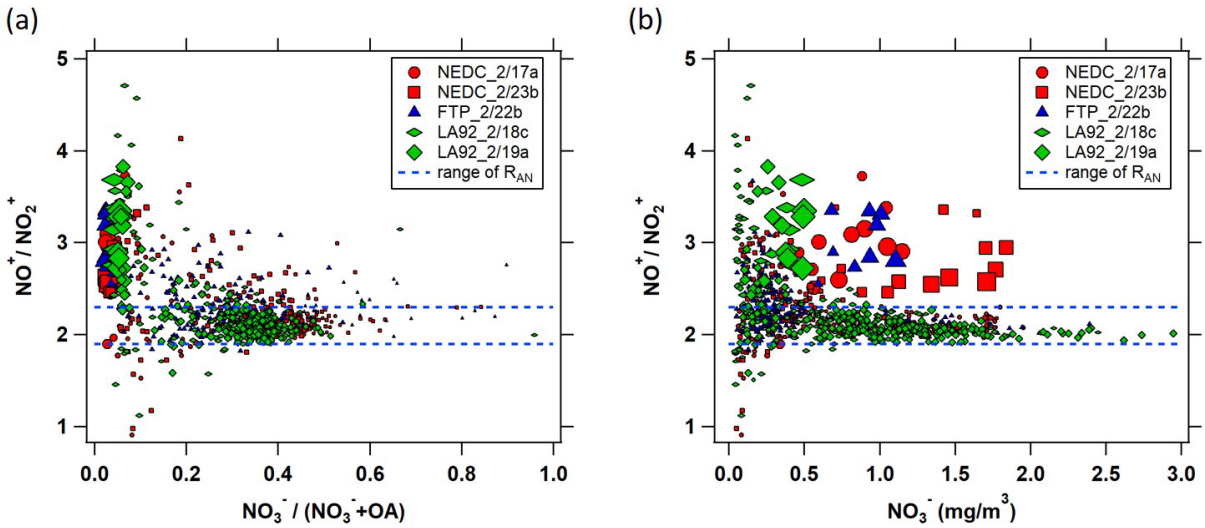

Note: The data points are sized to the maximum OA value in each run.

Figure 4. Observed high-resolution NO^+/NO_2^+ ratio during the full cold-start cycles of NEDC, FTP, and LA92 runs, as a function of (a) nitrate fraction relative to OA and (b) total measured nitrate.

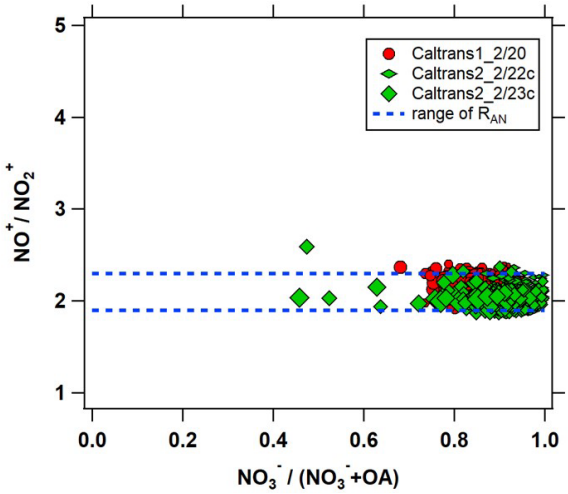

Note: The data points are sized to the maximum OA value in each run.

Figure 5. Observed high-resolution NO^+/NO_2^+ ratio during the hot-start Caltrans 1 and Caltrans 2 runs, as a function of nitrate fraction relative to OA.

Ammonium nitrate is not emitted directly from gasoline exhaust. However, secondary ammonium nitrate can be formed in the TSAR from the oxidation of NOx emissions to nitric acid, which then react with gaseous ammonia (NH_3). The limiting reagents in the atmospheric transformation of ammonium nitrate are nitric acid or NH_3 (Link et al., 2017). Although NH_3 emissions were not measured for this vehicle, an attempt was made to correlate ammonium nitrate formation with CO emissions since it is usually positively correlated with NH_3 emissions in spark ignition engines (Suarez-Bertoa et al., 2014). Ammonia can be formed during rich operations in the TWC from NO reduction by elemental H_2 during the water gas shift reaction of CO and hydrocarbon steam reforming (Suarez-Bertoa et al., 2014). A clear correlation between CO emissions and ammonium nitrate was not observed (Figure SM11), since in some cases CO emissions were low when at the same time ammonium nitrate production was elevated. These findings indicate that ammonium nitrate formation was largely driven by NOx emissions and limited by nitric acid formation rather than ammonia emissions.

Emission Factors

The emission factors (EFs), expressed in mg/mi, are shown in Figure 6 and Figure SM12. SOA formation for the cold-start cycles was significantly higher than that for the hot-start cycles, with the milder driving conditions of NEDC generating 2.8 and 7.6 times more SOA than LA92 and FTP, respectively. Cold-start SOA EFs were 31, 13, and 57 times higher than SOA EFs obtained during the hot-running phases of the NEDC, LA92, and FTP, respectively (Table SM1). As previously discussed, SOA EFs were on average 2.3 and 2.9 times higher for the first two phases of Caltrans 1 and Caltrans 2 cycles, respectively, that primarily represent congested highway driving conditions compared to the last two phases that represent high-speed, free-flow highway driving. Nitrate EFs contributed to the largest portion of total secondary aerosol, followed by ammonium. The hot-start Caltrans cycles showed the largest contribution of inorganic aerosol compared to the cold-start cycles, as a result of the higher NOx and NH_3 emissions. Analogous to SOA EFs, nitrate and ammonium EFs were on average 3.9 and 3.6 times higher for the first two phases of Caltrans 1 and 2.5 and 2.6 times higher for the first two phases of Caltrans 2 compared to the last two phases of the Caltrans cycles. The results in this report suggest that more secondary organic and inorganic aerosol will be formed from GDI vehicles when operated under highway congested traffic conditions.

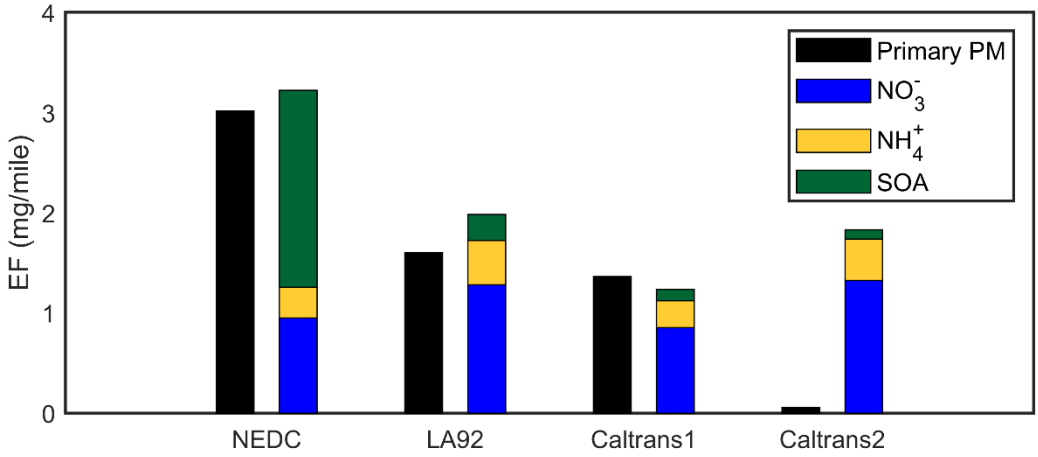

Note: The results are averages from repeatable duplicate runs, except for Caltrans 1, which was a single run.

Figure 6. Emission factors for primary PM measured by EEPS and aged NO_3^-, NH_4^+, and SOA measured by AMS for NEDC, LA92, Caltrans 1, and Caltrans 2 cycles.

Using an Oxidation Flow Reactor to Understand the Effects of Gasoline Aromatics and Ethanol Levels on Secondary Aerosol Formation

Methodology

Vehicle and Driving Cycles

A 2017 model year light-duty vehicle with a flex fuel 3.6-liter, 6-cylinder, naturally aspirated PFI, and spark ignition engine was employed in this study. The engine had a rated horsepower of 283 hp at 6400 rpm, a torque of 260 ft-lb at 4400 rpm, and a compression ratio of 10.2:1. The vehicle was equipped with a TWC and was certified under U.S. EPA Tier 3 B110 or California ULEVII emission standards.

The vehicle was tested on each fuel over the LA92 and US06 cycles. The LA92 is a dynamometer driving schedule for light-duty vehicles developed by the California Air Resources Board (CARB). It consists of three phases or three bags representing cold-start, hot-running, and hot-start driving conditions. Average emission data were calculated by incorporating weighting factors of 0.43, and 1, respectively, for representing the cold-start, hot-running, and hot-start LA92 phases. The LA92 has a total distance of 9.8 mi and an average speed of 24.6 mi/hr. The US06 Supplemental FTP (SFTP or US06) was developed to reflect aggressive, high-speed, and high-acceleration driving behavior. It has a total distance of 8.01 mi with an average speed of 48.4 mi/hr. Testing on the LA92 cycle was performed as a cold start, while testing on the US06 was a hot start with two back-to-back preconditioning US06 cycles to ensure the engine was warmed up.

Test Fuels

Three fuels were employed for this study that were manufactured and supplied by Gage Products Company (Ferndale, Michigan). The baseline fuel was a U.S. EPA Tier 3 E10 fuel (denoted as E10) with total aromatic content of 28.1 volume percent. A higher aromatic content E10 fuel (36.7 volume percent) was used to compare the impact of aromatics on primary emissions and aged PM (hereinafter denoted as E10HA). The third fuel contained 78 percent of denatured ethanol (denoted as E78) and was blended following the U.S. EPA Tier 3 and the CARB certification requirements for E85 fuels. The ethanol concentration of 78 volume percent was selected to meet the American Society for Testing and Materials (ASTM) D5798 Reid vapor pressure (RVP) target. The composition of each compound family for the test fuels is shown in Figure 7, while the main fuel properties are shown in Table SM2, SM.

Figure 7. Fuel composition as a function of the major compound family.

Emission Testing

Emission measurements were conducted in CE-CERT's VERL, on a Burke E. Porter 48-inch single-roll electric dynamometer. A PDP-CVS system was used to obtain standard bag measurements for THCs, CO, NOx, NMHCs, and CO_2. Gaseous emissions were determined according to the U.S. EPA protocols for light-duty emission testing as specified in the CFR, Title 40, Part 86. Cumulative tailpipe PM mass emissions were measured following the procedures in 40 CFR 1065. Total particle number concentrations were measured using a TSI 3776 ultrafine Condensation Particle Counter (CPC) with a 2.5 nm cut point. The instrument operated at a flowrate of 1.5 L/min. Solid particle number counts were measured with the use of a catalytic stripper. The particles were counted downstream of the catalytic stripper with a TSI 3776 ultrafine CPC at a flow rate of 1.5 L/min. An ejector diluter was used to collect particle number samples from the CVS tunnel. Particle size distributions were obtained using an EEPS spectrometer. The EEPS (TSI 3090, firmware version 8.0.0) was used to obtain real-time second-by-second size distributions between 5.6 and 560 nm. Particles were sampled at a flow rate of 10 L/min, which is considered high enough to minimize diffusional losses.

Photooxidation Experiments

Diluted exhaust (by dilution factors of about 200–350) from the vehicle was introduced into an oxidation flow reactor, which was designed and developed by Tampere University (hereinafter denoted as TSAR). More details about the TSAR are shown by Kuittinen et al. (2021) and Simonen et al. (2017, 2019), while details of the photooxidation setup are provided in SM. Briefly, the TSAR is an OFR254-type oxidation flow reactor that consists of a residence time chamber, an oxidation reactor, an ozone (O_3) generator, and an expansion tube connecting the residence time chamber and oxidation reactor. It was designed to measure potential secondary aerosol formation from rapidly changing emission sources, such as vehicle exhaust, and it is characterized by nearly laminar flow conditions. The vehicle exhaust combined with dilution by ozone and humidified air passes through the residence time chamber where it is exposed to 254 nm UV radiation, producing OH radicals from ozone photolysis. Precursors react with OH or O_3 to produce lower volatility molecules that then transfer to particle phase and produce secondary aerosol. The average photooxidation timescales (Table SM3) varied between 6.3 and 7.4 days of atmospheric aging, which are within the timescales previously found to simulate peak SOA formation (Kuittinen et al., 2021; Tkacik et al., 2014; Ortega et al., 2016). Figure SM1 shows the modeled OH exposure for all fuel/cycle combinations within TSAR. The photooxidation and corresponding OH exposures were calculated with a chemical reaction model considering CO suppression in the TSAR (Simonen et al., 2017).

Size-fractionated mass concentration of aerosols downstream of TSAR was measured by an ELPI+ (Dekati Ltd) at 1 Hz frequency while the bulk composition of the NR aerosols (OA, sulfate, nitrate, and ammonium) was measured by a mini aerosol mass spectrometer, equipped with a compact time-of-flight detector (mAMS, Aerodyne Research, Inc.), at 7–8 s intervals (Jayne et al., 2000; Vu et al., 2016). Given the mass accuracy of less than 20 ppm and mass resolution (i.e., m/Δm with *m* being the nominal m/z and *Δm* the full-width at half-maximum) of about 1100, high-resolution analysis of raw spectra was carried out using Wavemetrics Igor Pro (squirrel ToF-AMS analysis toolkit version 1.60 with PIKA module 1.20) to calculate the concentration of the inorganics (except ammonium), OA, and the main families of OA ($C_xH_y^+$, $C_xH_yO^+$, $C_xH_yO_{z>1}^+$) (Bahreini et al., 2012b). Given the variable concentration of CO_2 in the vehicle exhaust, gas-phase background CO_2 was subtracted from the OA mass spectra using the measured gas-phase CO_2 concentrations from the CVS and the recommendation by Collier and Zhang (2013). A composition-dependent collection efficiency factor was used to correct for particle bounce on the vaporizer (Middlebrook et al., 2012). Concentrations of the HOA were estimated based on a modification to the formula suggested by Ng et al. (2011) as outlined in Kuittinen et al. (2021), namely HOA is $13.4 \times C_{C4H9}^+$, where C_{C4H9}^+ is the concentration of the non-oxygenated, hydrocarbon-like ion at m/z 57. The remaining mass of OA was assigned as oxygenated and SOA.

Results

Primary Emissions over the LA92 and US06 Cycles

Table 1 shows the tailpipe gaseous and particulate emissions for the LA92 cycle. It was not possible to estimate the weighted emissions of E10 fuel over the LA92 cycle due to a failure in the chassis dynamometer controls during the hot-start phase (bag 3) of the LA92 cycle. However, a fuel comparison can be made based on the cold-start phase (bag 1) emissions of the LA92 cycle. While it was difficult to paint a complete picture for the weighted LA92 results, the cold-start phase showed higher THC, NMHC, CO, and NOx emissions for both E10HA and E78 fuels by factors of 1.5–4.7 and 4.2–6.8, respectively, compared to E10. Consistent with previous studies of PFI and GDI vehicles, THC, NMHC, and CO emissions will likely increase with higher aromatic content fuels (Zhu et al., 2017; Karavalakis et al., 2015; Yang et al., 2019a; Yang et al., 2019c). Cold-start conditions may have a significant impact on THC and NMHC emissions for fuels with high aromatics. Aromatic hydrocarbons have slower vaporization rates than paraffins, olefins, and alcohols, resulting in higher concentrations of heavier aromatics in E10HA that will affect fuel volatility (i.e., T80 and T90 values). These higher concentrations will cause incomplete evaporation during the cold-start conditions, leading to increased fuel impingement and higher formation of unburned in-cylinder hydrocarbon emissions. CO emissions also increased 4.7 times during the cold-start for E10HA relative to E10 fuel, similar to

previous findings of PFI and GDI vehicles (Yang et al., 2019a; Zhu et al., 2017; Karavalakis et al., 2015). The higher aromatic content of the E10HA fuel led to about 50 percent higher NOx emissions during the cold start, although previous studies have reported mixed results with mostly not statistically significant differences (Karavalakis et al., 2015; Yang et al., 2019a; Yang et al., 2019c).

Table 1. Cold Start and Weighted Gaseous and Particulate Emissions over the LA92 Cycle

Emissions	E10	E10HA	E78
cold-start-THC (g/mi)	0.42	1.94	2.33
weighted-THC (g/mi)	—	0.12	0.14
cold-start-NMHC (g/mi)	0.39	1.82	2.07
weighted-NMHC (g/mi)	—	0.11	0.11
cold-start-CO (g/mi)	2.05	7.54	8.57
weighted-CO (g/mi)	—	1.21	0.89
cold-start-NOx (g/mi)	0.08	0.13	0.57
weighted-NOx (g/mi)	—	0.03	0.05
cold-start-CO_2 (g/mi)	884.7	854.7	794.1
weighted-CO_2 (g/mi)	—	490.96	471.20
PM mass (mg/mi)	—	1.13	0.49
black-carbon (mg/mi)	—	0.36	0.12
cold-start-total-particle-number (#/mi)	1.55E+13	8.36E+13	3.40E+12
total-particle-number (#/mi)	1.03E+12	5.47E+12	4.77E+11
cold-start-solid-particle-number (#/mi)	1.23E+13	1.06E+13	1.51E+12
solid-particle-number (#/mi)	7.49E+11	1.13E+12	2.71E+11

Note: — means not applicable.

For the LA92 cycle, the use of E78 resulted in factors of 4.2–5.7 increase in THC, NMHC, and CO emissions relative to E10 during the cold phase. Previous works have also demonstrated higher THC and CO emissions with higher ethanol blends (Karavalakis et al., 2012; Costagliola et al., 2013; Suarez-Bertoa et al., 2015a; Iodice et al., 2016; Timonen et al., 2017). It is theorized that the higher heat of vaporization of E78 possibly led to cooler conditions in the combustion chamber and suppressed fuel evaporation. During cold-start conditions, more liquid fuel will likely be trapped in the crevice, which would enhance THC emissions. Additionally, NOx emissions increased significantly (factor of 6.8) for the cold phase of LA92 on E78 compared to E10. Higher NOx emissions with increasing ethanol content were also seen in previous studies of older PFI vehicles (Durbin et al., 2007; Karavalakis et al., 2012; Costagliola et al., 2013).

The US06 cycle showed different trends than the LA92 cycle, exhibiting slight (less than 1 percent for NMHC) to moderate (about 15 percent for THC and CO and 27 percent for NOx) decreases in these emissions with E10HA compared to E10 (Table 2). The impact of higher ethanol content was particularly pronounced. Emissions of THC, NMHC, and CO decreased by 95 percent, 87 percent, and 33 percent, respectively, with E78 compared to E10. The reductions in THC, NMHC, and CO emissions were primarily due to the oxygen content of ethanol, which contributed to more oxygen in locally fuel-rich regions and to more complete combustion (Catapano et al., 2016; Yang et al., 2019c). NOx emissions showed some increase (30 percent) with E78 compared to E10 fuel, similar to the LA92 cycle.

Table 2. Gaseous and Particulate Emissions over the US06 Cycle

Emissions	E10	E10HA	E78
THC (g/mi)	0.07	0.06	0.00
NMHC (g/mi)	0.04	0.04	0.01
CO (g/mi)	2.35	2.00	1.58
NOx (g/mi)	0.09	0.07	0.12
CO_2 (g/mi)	342.13	328.69	325.17
PM mass (mg/mi)	2.99	2.56	5.61
Black carbon (mg/mi)	0.41	0.47	0.46
Total particle number (#/mi)	7.17E+12	3.55E+05	1.16E+12
Solid particle number (#/mi)	8.40E+11	—	6.84E+11

Note: — means not applicable.

While no comparisons can be made between the PM mass and black carbon emissions for the E10 fuel over the LA92 cycle, the weighted PM mass and black carbon EFs were reduced by 57 percent and 66 percent, respectively, for E78 compared to E10HA (Table 1). For the LA92, total and solid particle number emissions for E78 showed large reductions of 54 percent and 64 percent compared to E10, and reductions of 91 percent and 76 percent compared to E10HA, respectively. The E10HA fuel showed more than a factor of 5 and 1.5 higher total and solid particle number emissions, respectively, relative to E10. The ratios of total particle number to solid particle number emissions were also increased for E10HA (7.89 for cold start and 4.84 for weighted) compared to E10 (1.26 for cold start and 1.38 for weighted) and E78 (2.25 for cold start and 1.76 for weighted). The results in this report for the LA92 agree with other works demonstrating PM and particle number emission reductions with higher ethanol blends (Yang et al., 2019c; Karavalakis et al., 2014a; Maricq et al., 2012; Jin et al., 2017). These reductions can be attributed to the higher oxygen content in the fuel, resulting in higher soot oxidation rates by the induction of HO_2 and OH-free radicals, and the aromatic dilution hindering the formation of soot precursors during combustion and lowering the rates of soot surface growth via the hydrogen abstraction acetylene addition (HACA) mechanism (Khosousi et al., 2015; Lemaire et al., 2010; Yang et al., 2019c).

For the US06, the particulate emissions were higher than the LA92 as a result of the more aggressive nature and the higher speeds and accelerations of the US06 cycle, which likely caused inefficient fuel vaporization and diffusive combustion during these driving conditions (Table 2). For the US06 cycle, slight changes in the black carbon EFs (-3 percent to more than 13 percent) were observed for E78 compared to E10HA and E10 fuels, while the total PM mass was increased by factors of 1.9–2.2 in E78. In contrast to the PM mass, the use of E78 led to total and solid particle number emission reductions by 84 percent and 19 percent, respectively, compared to E10. These findings likely suggest that the higher combustion temperature E78 fuel (as denoted by the higher NOx emissions) led to higher exhaust temperatures (not measured in this study), which probably led to desorption of carbon material from the exhaust transfer system and the subsequent contamination of the PM filter. A recent study has demonstrated that some degree of desorption would occur during aggressive driving (and high exhaust temperatures) experienced in the US06 cycle (Yang et al., 2020).

Figure 8 depicts the average number size distributions of the emitted particles for the LA92 and US06 cycles. For the LA92, all fuels showed a dominant accumulation mode with a less distinctive nucleation mode. Particle populations in the accumulation mode were higher for E10HA and substantially lower for E78, consistent with the PM mass for these fuels over the LA92. Particle size distribution for E10HA shifted towards a larger diameter (about 53 nm), while E10 and E78 peaked at around 34 nm and 30 nm, respectively. For the US06, particle size distributions were decisively bimodal, with E10 showing higher particle populations in the nucleation mode (about 10 nm). Accumulation mode particles dominated the size distribution for E78, with sizes centered at 60 nm compared to 70 nm for E10, particle populations similar to those of E10. The E78 particle sizing data over the US06

do not support the higher gravimetric PM mass for this fuel compared to E10, suggesting that other mechanisms may have played a role in PM mass emissions, including the possible desorption of contaminants in the CVS tunnel that were released during the high temperature conditions over US06.

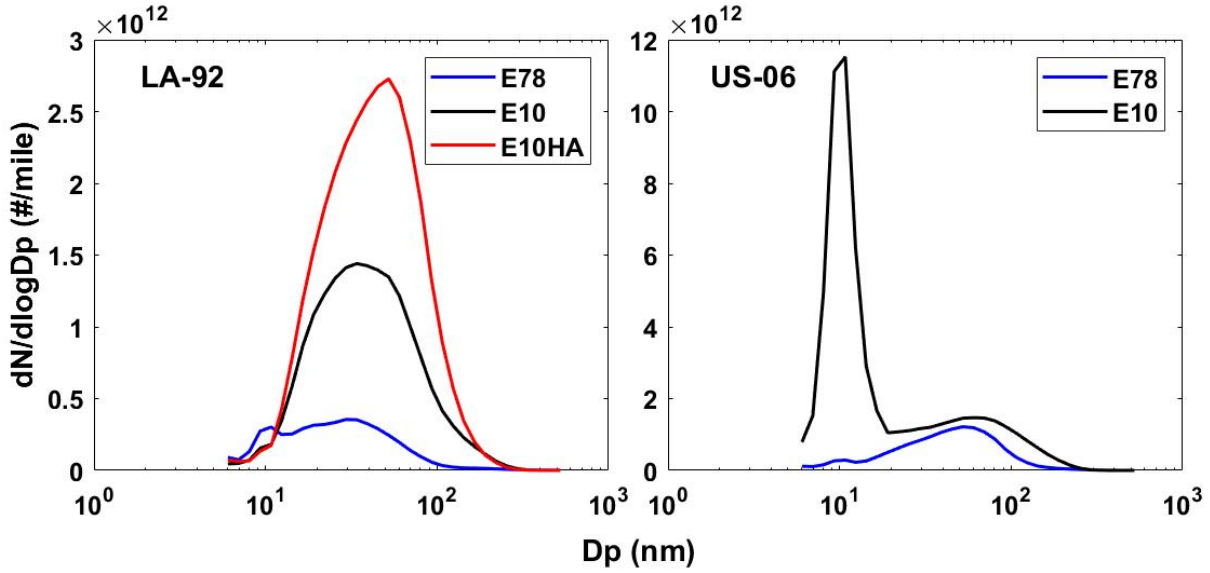

Figure 8. Average particle number size distributions over the LA92 (left-hand side) and US06 (right-hand side) cycles.

Secondary and Aged PM over the LA92 Cycle

Figure 9 shows the transient aged PM, SOA, aerosol nitrate, NOx, and NMHC emissions over the LA92 cycle for E10, E10HA, and E78 fuels. The NR composition data from mAMS are not available from E10 runs. Real-time primary PM emissions and sulfate and ammonium ions over the LA92 are shown in Figure SM14 in SM. For all fuels, aged PM were seen at least about two orders of magnitude higher than primary PM emissions during the entire duration of the LA92 cycle. When focusing on the details of the time-resolved data, it was seen that the cold start and acceleration events had the strongest influence on aged PM formation. Both E10 fuels resulted in higher concentrations and 5.7–8.1 times higher EFs of aged PM relative to E78, with E10HA showing more aged PM than E10 (Table SM4, SM). Thus, the findings are consistent with previous studies of high ethanol blends (Timonen et al., 2017; Roth et al., 2020b; Suarez-Bertoa et al., 2015; Gramsch et al., 2018), but show more clearly the crucial role of driving conditions in the emissions of secondary aerosol precursors. Analogous to primary emissions, the presence of the oxygen atom in ethanol and the dilution of aromatics were the main factors for the reduced SOA formation. Ethanol promotes the formation of oxygenated species, such as carboxylic, carbonyl, and low-molecular-weight ester compounds, which can seldomly act as SOA precursors. For example, this observation is supported by the results of a recent study that showed an abundance of alcohol, aldehydes, ketones, and ester compounds in primary aerosol from the exhaust of a GDI vehicle operated with E20 fuel over the LA92 cycle prior to irradiation in an environmental chamber (Roth et al., 2020a).

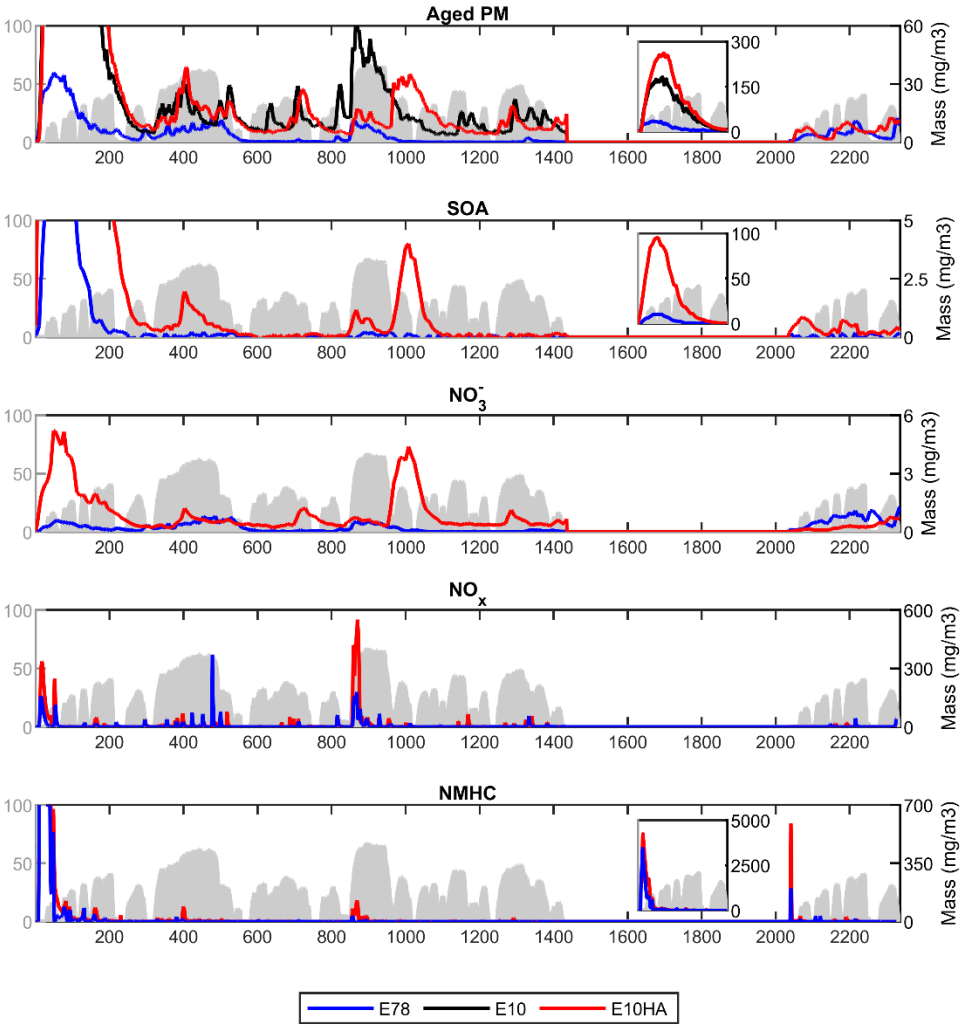

Note: For E10 fuel, only the aged PM data are available over the cold-start and hot-running phases. The subfigures show the first 300 s of the cold-start phase. The concentrations shown have been corrected to represent tailpipe concentrations.

Figure 9. Aged PM, SOA, nitrate, NOx, and NMHC concentration over the LA92 cycle with E10, E10HA, and E78.

SOA formation was significantly affected by the cold-start period of the LA92 cycle, especially for E10HA fuel, which exhibited about 30 times more SOA mass during the first 200 s compared to the second large spike for this fuel at around 400 s. The cold-start EF of SOA with E10HA was higher than E78 by a factor of 11, as shown in Table SM4, SM. The results agree with previous studies reporting on the dominance of the cold-start period on SOA formation from gasoline vehicles (Kuittinen et al., 2021; Karjalainen et al., 2016; Simonen et al., 2019; Pieber et al., 2018; Zhao et al., 2018; Saliba et al., 2017; Roth et al., 2020b). The substantially higher SOA mass for E10HA during the cold start was largely due to the presence of heavier aromatics for this fuel, which likely generated more IVOCs and SVOCs. Previous studies have proposed that IVOC emissions are important SOA precursors from gasoline vehicles (Robinson et al., 2007; Gentner et al., 2017; Drozd et al., 2019; Peng et al., 2017). McCaffery et al. (2020) showed that PFI FFVs when operated with alcohol fuels can be major contributors to aromatic IVOC emissions, with lower emission rates as the alcohol content increased in gasoline. Aromatics are more difficult to evaporate during cold-engine operation compared to other hydrocarbons, resulting in more liquid fuel wetting in the cylinder walls and increased formation of VOC precursors (Yang et al., 2019a). Roth et al. (2020b) demonstrated an important influence of heavier aromatics with high double-bond equivalents on SOA formation from a gasoline vehicle over the LA92 cycle. Drozd et al. (2019) reported that BTEX compounds

contribute to about 40 percent of SOA formation from gasoline vehicles. Other studies have also shown the important contribution of BTEX species on SOA formation (Roth et al., 2020a; Nordin et al., 2013; Gordon et al., 2014; Timonen et al., 2017).

Overall, SOA formation was reduced significantly during the hot-running and hot-start phases of LA92 (by two orders of magnitude for E10HA and four orders of magnitude for E78), and coincided with the sharp acceleration events, as well as the tailpipe NMHC emissions. The higher SOA formation during the cold start was primarily attributed to the TWC being below its light-off temperature and therefore inefficient to oxidize SOA precursors (i.e., aromatic VOCs and other NMHCs), leading to their higher emissions. In addition, the inefficient TWC also contributed to the semivolatile fraction of nanoparticles, which can act as seeds for further reactions in the TSAR, resulting in enhanced SOA mass. For the hot-running and hot-start phases, the higher intake air temperature, fuel temperature, and piston surface temperature aided improved fuel vaporization and resulted in lower SOA precursor emissions, which were also more efficiently oxidized in the TWC. The detailed composition of SOA (Figure 10) shows higher contribution from non-oxygenated $C_xH_y^+$ and intermediately oxygenated $C_xH_yO^+$ family of ions to OA compared to highly oxygenated $C_xH_yO_{z>1}^+$ (38–45 percent versus 13–15 percent) during the cold-start phase of both E78 and E10HA while during the hot-running and hot-start phases, the contribution of $C_xH_yO_{z>1}^+$ was more comparable to or even higher than those of the less oxygenated fragments (Figure 10). During the cold-start phase, the contribution of each family of ions to OA was not significantly different between E78 and E10HA, suggesting that given the oxidation extent of the exhaust, similar types of OA functional groups were present in the SOA regardless of the fuel type. However, in the hot-running and hot-start phases, contribution of the intermediately oxygenated family ($C_xH_yO^+$) was significantly lower with E78 compared to E10HA.

Consistent with previous studies, inorganic secondary aerosol in the form of ammonium nitrate was found in elevated levels (Kuittinen et al., 2021; Vu et al., 2019; Roth et al., 2020a; Roth et al., 2020b; Gordon et al., 2014; Link et al., 2017). The total weighted EF of NO_3 was higher for E10HA compared to E78 (1.62 mg/mi versus 0.47 mg/mi) (Table SM4, SM). The much lower NO_3 EF observed for E78 is counterintuitive since higher NOx emissions were observed for E78, especially during the cold-start phase. One possible explanation may be the lower OH exposure during the cold start and subsequently lower nitric acid production during the E78 runs; however, the researchers do not have an estimate of the OH exposure during the LA92 run with E10HA.

Aerosol sulfate was found in much lower concentrations than nitrate and ammonium and was associated with cold-start and vehicle accelerations (Table SM3, SM). For E78, it comprised less than 0.2 percent of the total secondary aerosol, as a consequence of the very low sulfur levels in the test fuels, while with E10HA, its contribution increased to 1.1 percent during the cold start. The sulfate EF during the cold-start phase of LA92 on E10HA was 65 times higher than with E78. Furthermore, its total weighted EF was 20 times higher with E10HA compared to E78.

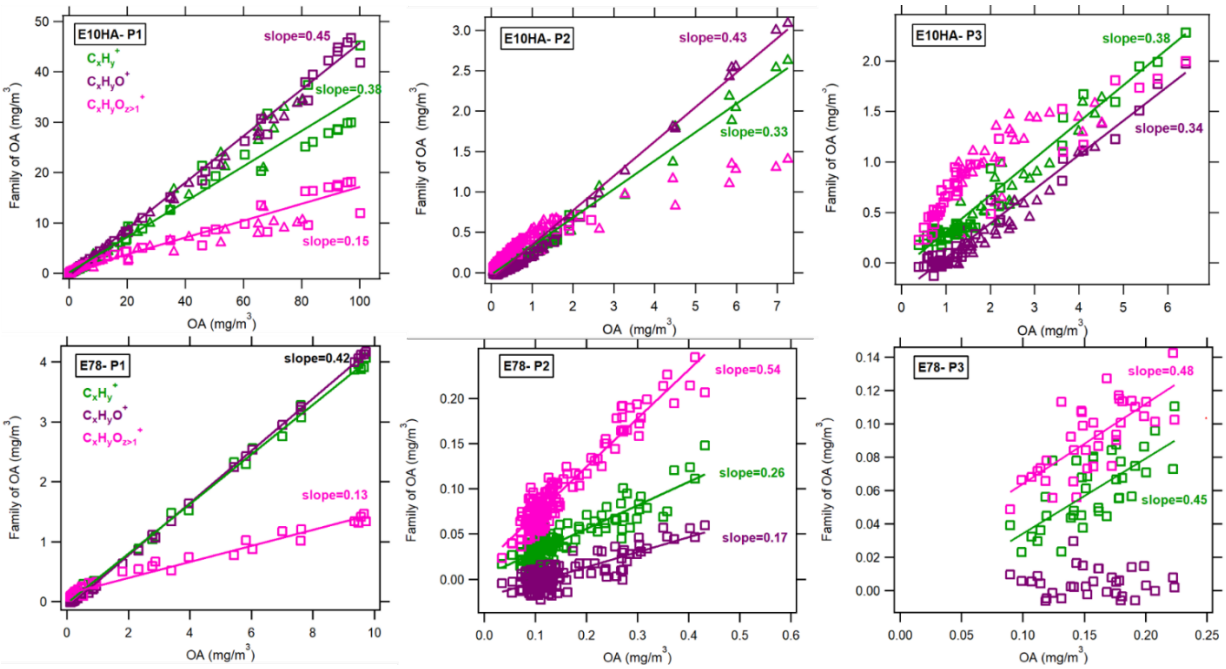

Note: P1 is the cold-start phase, and P2 and P3 are the hot-running and hot-start phases, respectively.

Figure 10. Relative contribution of different ion families to total **OA for the LA92 cycle using E10HA and E78 fuels.**

Secondary and Aged PM over the US06 Cycle

Figure 11 shows the transient aged PM, SOA, aerosol nitrate, NOx, and NMHC emissions over the US06 cycle for E10, E10HA, and E78 fuels. Real-time primary PM emissions and sulfate and ammonium ions over the US06 cycles are shown in Figure SM15, SM. Similar to LA92, for E10 fuel, aged PM were seen at least two orders of magnitude higher than primary PM emissions during the entire duration of the US06 cycle (a comparison for E10HA fuel could not be carried out due to lack of EEPS measurements). Compared to both E10 fuels, aged PM EFs for E78 were lower by 44–54 percent. When comparing the US06 and LA92, EFs of aged PM compared differently with the weighted EFs of aged PM during the LA92 cycle depending on the fuel; the EF of aged PM during US06 was comparable to that during LA92 on E10HA, 33 percent lower on E10, and a factor of 3.3 higher on E78. However, EFs of aged PM on US06 were consistently lower than during the cold-start phase of LA92 for each fuel.

For the US06 cycle and similar to LA92, E10HA led to more SOA formation followed by E10 and E78. Consistently, measured OA relative to emitted CO was highest with E10HA and lowest with E78, as shown in Figure 12. Additionally, SOA EFs on E10 were 50 percent lower than on E10HA and 3.5 times higher than on E78. Compared to LA92, SOA EFs were 13–62 percent lower than the weighed SOA EFs, with the largest difference observed for E10HA. SOA formation was favored during acceleration events, with lower SOA during periods with steady high speed and no rapid accelerations (i.e., about 200–300 s and about 350–480 s). This occurrence was noticeable within the period of steady high-speed driving at about 300 s, where a rapid acceleration led to more NMHC emissions and SOA formation. The E10HA fuel contained higher levels of BTEX and heavier aromatics than E10. Aromatic VOC emissions were likely to occur during acceleration events and high-speed driving, which affected SOA production. This likelihood is due to the fact that higher boiling point aromatics will require a longer time to evaporate, especially during the high-speed and power conditions of the US06 when longer fuel injection duration is demanded, resulting in higher precursor emissions. Assuming the relative composition of the monoaromatics, naphthalenes, and naphtheno/olefin benzenes of the exhaust is similar to those in the fuels, the research team can compare the SOA formation potential of these compounds using different fuels. In this exercise, contributions of other hydrocarbons from the fuel (namely, paraffins, napththenes, olefins, and oxygenates) are ignored since the

weighted carbon number in each class was C2 to less than C8, making them on average too small in size and insignificant for SOA formation. By scaling the literature-based SOA yield values of various aromatic species (based on carbon number and compound class [Gentner et al., 2012]) with the corresponding carbon weight fraction in the fuel, the researchers estimated the corresponding weighted cumulative SOA yield values for E78, E10, and E10HA to be 0.53, 2.96, and 3.87, respectively. The yield values are dominated by C7–C10 monoaromatic species (Table SM2, SM). Although these values do not necessarily reflect the actual SOA yield of the exhaust emissions, they support the observation that SOA formations from E10 and E10HA are significantly higher than from E78. In fact, because of the higher aromatic (C6–C12) content of E10HA, its cumulative SOA formation potential is estimated to be 30 percent and a factor of 7.3 higher than that of E10 and E78, respectively, assuming hydrocarbon emissions in the exhaust follow the same composition as the fuel itself (Table SM2, SM). To a first approximation, the differences between the observed EFs of SOA for different fuels during US06 operation are consistent with this simple calculation; the EF on E10HA was 51 percent and a factor of 5.3 higher than E10 and E78, respectively. Despite differences in the extent of SOA formation from these different fuels, and consistent with the observations from the LA92 runs, the overall composition of OA was similar between US06 runs with different fuels (Figure SM16, SM).

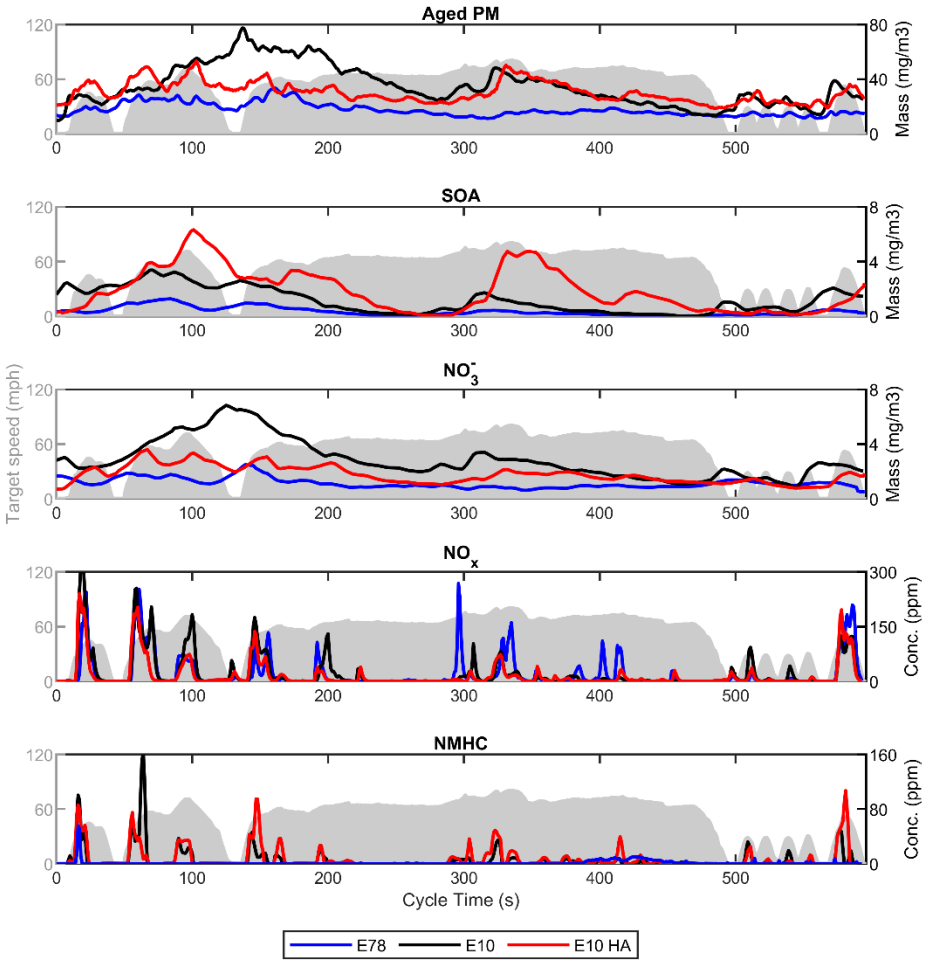

Note: NMHC concentrations for E78 were multiplied by a factor of 10. The concentrations shown have been corrected to represent tailpipe concentrations.

Figure 11. Aged PM, SOA, nitrate, NOx, and NMHC concentration **over the US06 cycle with E10, E10HA, and E78.**

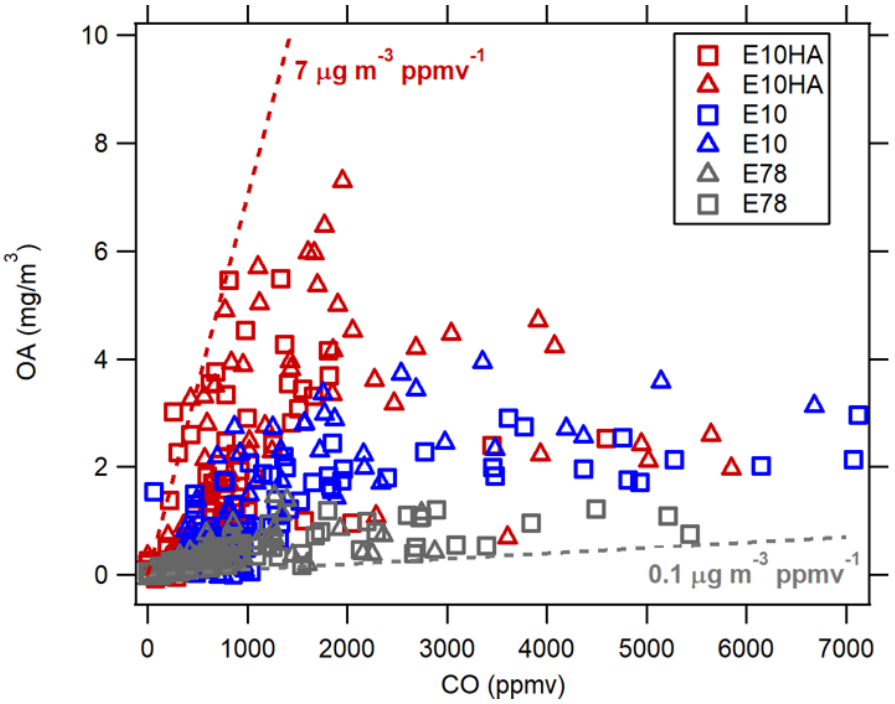

Note: Different symbols of similar color present data from duplicate runs. The dashed lines represent the extreme boundaries of the data.

Figure 12. Correlation between measured OA and emitted CO for US06 runs on E10HA, E10, and E78 fuels.

Similar to LA92, nitrate EFs decreased in US06 in the following order: E10>E10HA>E78. However, for the US06, nitrate EFs were higher than LA92 by factors of 1.5 and 3.3 for E10HA and E78, respectively, despite slightly lower overall OH exposures in US06 versus LA92 runs on E78 (6.7 days versus 7.0 days; OH exposure on E10HA for LA92 not available). The changes in factors can be explained by the higher combustion temperature and the enhanced generation of NOx emissions during the more dynamic driving of US06 as seen by about twice as high NOx emissions on E10HA and E78 compared to LA92 (NOx emissions on US06 with E10 are not available), which favor secondary nitrate aerosol formation. For the E10 fuel, the EF of NO_3 was lower during US06 than LA92 by 33 percent. While nitrate aerosol was produced throughout the entire duration of US06, large nitrate spikes were only seen during the sharp accelerations of LA92 and during the cold start. For both cycles, nitrate aerosol was lower for E78, suggesting that the introduction of higher ethanol blends in the light-duty vehicle market will potentially result in nitrate aerosol reductions.

The use of E78 led to lower ammonium aerosol concentrations relative to both E10 fuels for both US06 and LA92 cycles, indicating beneficial ethanol effects on inorganic aerosol formation. Consistent with the trend for nitrate, ammonium aerosol concentrations were also higher for the US06 compared to LA92 on E10HA (by 56 percent) and E78 (by a factor of 5.3). Ammonium nitrate formation is usually favored by tailpipe ammonia (NH_3) emissions formed in the TWC from NO reduction by hydrogen produced from the water gas shift reaction of CO or via hydrocarbon steam reforming (Link et al., 2017; Suarez-Bertoa et al., 2015b). NH_3 emissions largely depend on rich-fuel conditions, typical of accelerations and dynamic driving where elevated CO concentrations also occur. Although NH_3 emissions were not measured in this study, CO EFs correlated positively with that of ammonium for US06 (Figure SM17, SM). Similar findings were reported by Link et al. (2017) when they tested gasoline vehicles using an oxidation flow reactor. The results suggest that ammonium nitrate production was primarily driven by NH_3 emissions rather than NOx emissions.

For the US06 cycle, aerosol sulfate mostly peaked during accelerations and high-speed driving conditions. Similar to LA92, the use of the lowest sulfur content E78 fuel led to the lowest concentrations of sulfate. In fact, the EF of aerosol sulfate during US06 using E78 was half of those of each E10 fuel. Sulfate is usually sourced from fuel and lubricant oil sulfur compounds stored in the TWC and eventually released as SO_2 prompting the formation of sulfate aerosol, especially during accelerations and high-speed conditions (Simonen et al., 2019; Karjalainen et al., 2014). Thus, it is expected that more aerosol sulfate is generated during cold starts due to the partially evaporated fuel and lubricant oil components, and dynamic driving conditions due to the higher fuel and lubricant oil consumption. This increase in aerosol sulfate explains why sulfate EFs on E10HA were significantly (about 80 times) higher during the cold-start phase of LA92 versus US06, whereas the EF for the cold start of LA92 on E10 was only 77 percent higher than US06 on E10.

Conclusions

For the first part of this study (Chapter 2), the results showed that the cold-start period generated significant SOA mass, resulting in about 70–80 percent of the NR mass being SOA. After the TWC warm-up, the contribution of SOA decreased to about 5–12 percent of the NR mass while that of nitrate increased from about 15 percent to about 60–73 percent. After the cold-start phase, however, the total NR mass was also significantly (up to five times) lower than during the cold-start phase. These observations suggest that warming of the TWC is an important factor in reducing emissions of SOA precursors. Furthermore, the influence of vehicle emissions on secondary PM formation, both in terms of concentration and type, changes as the vehicle is driven farther/longer and the TWC is warmed up. The observations suggest that under stagnant and cold conditions, PM exposure of neighborhood residents can be significantly different than for travelers who are outside the neighborhood.

A notable feature of the data is the significant emissions of nitrate (predominantly ammonium nitrate) in these drive cycles, except for NEDC and FTP runs, with total nitrate EFs being 4–14 times higher than SOA. Given the semivolatile nature of ammonium nitrate and its equilibrium with gas-phase ammonia and nitric acid, ambient levels of ammonium nitrate may never reach concentrations significantly higher than SOA unless the ambient temperature and RH levels are favorable. Regardless, since ammonium nitrate formation is suspected to be nitric-acid-limited, controls that further reduce NOx emissions will reduce formation of inorganic PM and improve regional air quality.

For the second part of this study (Chapter 3), the researchers examined the primary emissions and secondary aerosol formation potential from a FFV equipped with a PFI gasoline engine when operated with two E10 fuels of different aromatic contents and an E78 blend. Testing was conducted over the LA92 and US06 driving cycles using a chassis dynamometer. Primary emission results showed mixed trends across the different fuels and driving cycles. The use of E78 led to increases in THC, NMHC, CO, and NOx emissions over the LA92 compared to E10 fuels, but decreases in these pollutants over the US06. Particulate emissions, including PM mass, black carbon, and total and solid particle number showed reductions with E78 compared to E10 fuels for both cycles. An exception was the PM mass with E78 over the US06, which is believed to have been caused by the contamination of the exhaust transfer system during aggressive driving and high-exhaust temperature conditions.

Secondary aerosol formation potential measured with an oxidation flow reactor was strongly dependent on cold-start conditions and especially during the first 200–300 s of the cycle. A strong influence on the formation of secondary aerosol was also seen during the sharp acceleration events of the LA92 and US06 cycles. The higher aromatic E10 fuel produced greater concentrations of secondary aerosol compared to E10, whereas the E78 blend resulted in the least secondary aerosol formation. Ammonium nitrate formation was elevated for both test cycles and fuels, with the E78 blend leading to lower inorganic aerosol formation. Overall, this study showed the beneficial effects on secondary aerosol forming potential by using high ethanol blends in gasoline vehicles and the adverse effects of high aromatic content fuels on primary emissions and secondary aerosol formation. The results in this report also revealed that during cold-start operation, the fuel composition will likely play a key role on secondary aerosol production due to the higher generation of secondary aerosol precursors at the tailpipe, and highlighted the importance of using transient conditions and time-resolved characterization in research focusing on secondary aerosols linked with mobile sources.

Research Outputs, Outcomes, and Impacts

For this program, the research team published one journal paper and submitted an additional journal paper, which is under review:

- Kuittinen, N., McCaffery, C., Peng, W., Zimmerman, S., Roth, P., Simonen, P., Karjalainen, P., Keskinen, J., Cocker, D. R., Durbin, T. D., Rönkkö, T., Bahreini, R., and Karavalakis, G. Effects of driving conditions on secondary aerosol formation from a GDI vehicle using an oxidation flow reactor. *Environmental Pollution*, 2021, vol. 282, 117069. (Impact Factor: 6.792)
- Kuittinen, N., McCaffery, C., Zimmerman, S., Bahreini, R., Simonen, P., Karjalainen, P., Keskinen, J., Rönkkö, T., and Karavalakis, G. Using an oxidation flow reactor to understand the effects of gasoline aromatics and ethanol levels on secondary aerosol formation. Submitted to *Environmental Research*. (Impact Factor: 5.715)

Several presentations were made describing the results of this program in international conferences:

- Peng, W., Kuittinen, N., McCaffery, C., Zimmerman, S., Roth, P., Bahreini, R., Cocker, D. R., and Karavalakis, G. Secondary organic aerosol (SOA) formation from a light-duty gasoline direct injection (GDI) vehicle at different drive conditions. 37th American Association for Aerosol Research, October 14–18, 2019, Portland, Oregon, United States.
- Kuittinen, N., Peng, W., McCaffery, C., Zimmerman, S., Karjalainen, P., Roth, P., Simonen, P., Keskinen, J., Rönkkö, T., Cocker, D. R., Bahreini, R., and Karavalakis, G. Effect of high-speed driving conditions on SOA formation potential from GDI vehicle. 23rd International Transport and Air Pollution Conference, May 15–17, 2019, Thessaloniki, Greece.
- Kuittinen, N., Zimmerman, S., Peng, W., McCaffery, C., Roth, P., Simonen, P., Keskinen, J., Rönkkö, T., Bahreini, R., Cocker, D. R., and Karavalakis, G. An overview of UCR's research on secondary organic aerosol production from mobile sources: Discussions on the effects of high-speed driving conditions on SOA formation potential from GDI vehicles. Center for Advancing Research in Transportation Emissions, Energy, and Health. A USDOT University Transportation Center. Transportation, Air Quality, and Health Symposium. February 18–20, 2019, Austin, Texas, United States.
- Kuittinen, N., Zimmerman, S., Peng, W., McCaffery, C., Roth, P., Simonen, P., Keskinen, J., Rönkkö, T., Bahreini, R., Cocker, D. R., and Karavalakis, G. Effect of high-speed driving conditions on SOA formation potential from GDI vehicle. 2018 International Aerosol Conference, St. Louis, Missouri, United States.

Technology Transfer Outputs, Outcomes, and Impacts

For the purpose of this study, a strategic research partnership was developed between UCR and Tampere University in Finland. Within UCR, the lead for this project was assumed by CE-CERT, with major assistance from the Department of Chemical and Environmental Engineering and the Department of Environmental Sciences. The UCR team closely worked with the Faculty of Engineering and Natural Sciences at Tampere University. The researchers anticipate that this collaboration will continue in similar and other research topics between the two universities, which will benefit the research and academic community, as well as inform regulatory and environmental agencies in the United States and EU on new technologies and research outputs that will potentially affect decision-making policies.

Education and Workforce Development Outputs, Outcomes, and Impacts

For this study, several graduate students were actively involved in designing, setting up, and executing the experiments, data curation and analysis, and manuscript writing and review. During the duration of this project, a graduate student, Niina Kuittinen, from Tampere University visited UCR's CE-CERT under the supervision of Georgios Karavalakis (principal investigator of this project). In addition, three Ph.D. students from UCR, Cavan

McCaffery, Weihan Peng, and Patrick Roth, were actively involved in this program. A master's student, Stephen Zimmerman, was also involved with testing and data analysis.

References

Aikawa, K., Sakurai, T., and Jetter, J. J. Development of a predictive model for gasoline vehicle particulate matter emissions. *SAE International Journal of Fuels and Lubricants*, 2010, 3, 610–622.

Aiken, A. C., DeCarlo, P. F., Kroll, J. H., Worsnop, D. R., Huffman, J. A., Docherty, K. S., Ulbrich, I. M., Mohr, C., Kimmel, J. R., Sueper, D., Sun, Y., Zhang, Q., Trimborn, A., Northway, M., Ziemann, P. J., Canagaratna, M. R., Onasch, T. B., Alfarra, M. R., Prevot, A. S. H., Dommen, J., Duplissy, J., Metzger, A., Baltensperger, U., and Jimenez, J. L. O/C and OM/OC ratios of primary, secondary, and ambient organic aerosols with high-resolution time-of-flight aerosol mass spectrometry. *Environmental Science and Technology*, 2008, 42, 4478–4485.

Bahreini, R., Middlebrook, A. M., Brock, C. A., de Gouw, J. A., McKeen, S. A., Williams, L. R., Daumit, K. E., Lambe, A. T., Massoli, P., Canagaratna, M. R., Ahmadov, R., Carrasquillo, A. J., Cross, E. S., Ervens, B., Holloway, J. S., Hunter, J. F., Onasch, T. B., Pollack, I. B., Roberts, J. M., Ryerson, T. B., Warneke, C., Davidovits, P., Worsnop, D. R., and Kroll, J. H. Mass spectral analysis of organic aerosol formed downwind of the deepwater horizon oil spill: Field studies and laboratory confirmations. *Environmental Science and Technology*, 2012b, 46, 8025–8034.

Bahreini, R., Middlebrook, A. M., de Gouw, J. A., Warneke, C., Trainer, M., Brock, C. A., Stark, H., Brown, S. S., Dube, W. P., Gilman, J. B., Hall, K., Holloway, J. S., Kuster, W. C., Perring, A. E., Prevot, A. S. H., Schwarz, J. P., Spackman, J. R., Szidat, S., Wagner, N. L., Weber, R. J., Zotter, P., and Parrish, D. D. Gasoline emissions dominate over diesel in formation of secondary organic aerosol mass. *Geophysical Research Letters*, 2012a, 39, L06805, doi: 10.1029/2011GL050718.

Cao, J., Wang, Q., Li, L., Zhang, Y., Tian, J., Antony Chen, L. W., Hang-Ho, S. S., Wang, X., Chow, J. C., and Watson, J. G. Evaluation of the oxidation flow reactor for particulate matter emission limit certification. *Atmospheric Environment*, 2020, 224, 117086.

Catapano, F., Sementa, P., and Vaglieco, B. M. Air-fuel mixing and combustion behavior of gasoline-ethanol blends in a GDI wall-guided turbocharged multi-cylinder optical engine. *Renewable Energy*, 2016, 96, 319–332.

Chen, L., Liang, Z., Zhang, X., and Shuai, S. Characterizing particulate matter emissions from GDI and PFI vehicles under transient and cold start conditions. *Fuel*, 2017, 189, 131–140.

Cheng, Y., Wang, J., Zhuang, R., and Wu, N. Analysis of combustion behaviour during cold-start and warm-up process of SI gasoline engine. SAE Technical Paper, 2001, 2001-01-3557.

Clairotte, M., Adam, T. W., Zardini, A. A., Manfredi, U., Martini, G., Krasenbrink, A., Vicet, A., Tournie, E., and Astorga, C. Effects of low temperature on the cold start gaseous emissions from light duty vehicles fueled by ethanol-blended gasoline. *Applied Energy*, 2013, 102, 44–54.

Collier, S., and Zhang, Q. Gas-phase CO_2 subtraction for improved measurements of the organic aerosol mass concentration and oxidation degree by an aerosol mass spectrometer. *Environmental Science and Technology*, 2013, 47, 14324–14331.

Costagliola, M. A., De Simio, L., and Pratti, M. V. Combustion efficiency and engine out emissions of a S.I. engine fueled with alcohol/gasoline blends. *Applied Energy*, 2013, 111, 1162–1171.

Drozd, G. T., Zhao, Y., Saliba, G., Frodin, B., Maddox C., Chang, M. C. O., Maldonado, H., Sardar, S., Weber, R. J., Robinson, A. L., and Goldstein, A. H. Detailed speciation of intermediate volatility and semivolatile organic compound emissions from gasoline vehicles: Effects of cold-starts and implications for secondary organic aerosol formation. *Environmental Science and Technology*, 2019, 53, 1706–1714.

Du, Z., Hu, M., Peng, J., Zhang, W., Zheng, J., Gu, F., Qin, Y., Yang, Y., Li, M., Wu, Y., Shao, M., and Shuai, S. Comparison of primary aerosol emission and secondary aerosol formation from gasoline direct injection and port fuel injection vehicles. *Atmospheric Chemistry and Physics*, 2018, 18, 9011–9023.

Durbin, T. D., Miller, J. W., Younglove, T., Huai, T., and Cocker, K. Effects of fuel ethanol content and volatility on regulated and unregulated exhaust emissions for the latest technology gasoline vehicles. *Environmental Science and Technology*, 2007, 41, 4059–4064.

Duronio, F., De Vita, A., Montanaro, A., and Villante, C. Gasoline direct injection engines—A review of latest technologies and trends. Part 2. *Fuel*, 2020, 265, 116947.

Fushimi, A., Kondo, Y., Kobayashi, S., Fujitani, Y., Saitoh, K., Takami, A., and Tanabe, K. Chemical composition and source of fine and nanoparticles from recent direct injection gasoline passenger cars: Effects of fuel and ambient temperature. *Atmospheric Environment*, 2016, 124, 77–84.

Gentner, D. R., Isaacman, G., Worton, D. R., Chan, A. W. H., Dallmann, T. R., Davis, L., Liu, S., Day, D. A., Russell, L. M., Wilson, K. R., Weber, R., Guha, A., Harley, R. A., and Goldstein, A. H. Elucidating secondary organic aerosol from diesel and gasoline vehicles through detailed characterization of organic carbon emissions. Proceedings of the National Academy of Sciences of the United States of America, 2012, 109, 18318–18323.

Gentner, D. R., Jathar, S. H., Gordon, T. D., Bahreini, R., Day, D. A., Haddad, I. E., Haynes, P. L., Pieber, S. M., Platt, S. M., De Gouw, J., Goldstein, A. H., Harley, R. A., Jimenez, J. L., Prevot, A. S. H., and Robinson A. L. Review of urban secondary organic aerosol formation from gasoline and diesel motor vehicle emissions. *Environmental Science and Technology*, 2017, 51, 1074–1093.

Gordon, T. D., Presto, A. A., May, A. A., Nguyen, N. T., Lipsky, E. M., Donahue, N. M., Gutierrez, A., Zhang, M., Maddox, C., Rieger, P., Chattopadhyay, S., Maldonado, H., Maricq, M. M., and Robinson, A. L. Secondary organic aerosol formation exceeds primary particulate matter emissions for light-duty gasoline vehicles. *Atmospheric Chemistry and Physics*, 2014, 14, 4661–4678.

Gramsch, E., Papapostolou, V., Reyes, F., Vásquez, Y., Castillo, M., Oyola, P., López, G., Cadiz, A., Ferguson, S., Wolfson, M., Lawrence, J., and Koutrakis, P. Variability in the primary emissions and secondary gas and particle formation from vehicles using bioethanol mixtures. *Journal of the Air and Waste Management Association*, 2018, 68, 329–46.

Hays, M. D., Preston, W., George, B. J., Schmid, J., Baldauf, R., Snow, R., Robinson, J. R., Long, T., and Faircloth, J. Carbonaceous aerosols emitted from light-duty vehicles operating on gasoline and ethanol fuel blends. *Environmental Science and Technology*, 2013, 47, 14502–14509.

He, Y., King, B., Pothier, M., Lewane, L., Akherati, A., Mattila, J., Farmer, D. K., McCormick, R. L., Thornton, M., Pierce, J. R., Volckens, J., and Jathar, S. H. Secondary organic aerosol formation from evaporated biofuels: Comparison to gasoline and correction for vapor wall losses. *Environmental Science: Processes and Impacts*, 2020, 22, 1461–1474.

Herrington, J. S., Hays, M. D., George, B. J., and Baldauf, R. W. The effects of operating conditions on semivolatile organic compounds emitted from light-duty, gasoline-powered motor vehicles. *Atmospheric Environment*, 2012, 54, 53–59.

Iodice, P., Senatore, A., Langella, G., and Amoresano, A. Effect of ethanol–gasoline blends on CO and HC emissions in last generation SI engines within the cold-start transient: An experimental investigation. *Applied Energy*, 2016, 179, 182–190.

Jathar, S. H., Woody, M., Pye, H. O. T., Baker, K. R., and Robinson, A. L. Chemical transport model simulations of organic aerosol in southern California: Model evaluation and gasoline and diesel source contributions. *Atmospheric Chemistry and Physics*, 2017, 17, 1–18.

Jayne, J. T., Leard, D. C., Zhang, X., Davidovits, P., Smith, K. A., Kolb, C. E., and Worsnop, D. W. Development of an aerosol mass spectrometer for size and composition analysis of submicron particles. *Aerosol Science and Technology*, 2000, 33, 49–70.

Jimenez, J. L., Canagaratna, M. R., Donahue, N. M., Prevôt, A. S. H., Zhang, Q., Kroll, J. H., Decarlo, P. F., Allan, J. D., Coe, H., Ng, N. L., Aiken, A. C., Ulbrich, I. M., Grieshop, A. P., Duplissy, J., Wilson, K. R., Lanz, V. A., Hueglin, C., Sun, Y. L., Tian, J., Laaksonen, A., Raatikainen, T., Rautiainen, J., Vaattovaara, P., Ehn, M., Kulmala, M., Tomlinson, J. M., Cubison, M. J., Dunlea, E. J., Alfarra, M. R., Williams, P. I., Bower, K., Kondo, Y., Schneider, J., Drewnick, F., Borrmann, S., Weimer, S., Demerjian, K., Salcedo, D., Cottrell, L., Takami, A., Miyoshi, T., Shimono, A., Sun, J. Y., Zhang, Y. M., Dzepina, K., Sueper, D., Jayne, J. T., Herndon, S. C., Williams, L. R., Wood, E. C., Middlebrook, A. M., Kolb, C. E., Baltensperger, U., and Worsnop, D. R. Evolution of organic aerosols in the atmosphere. *Science*, 2009, 326, 1525–1529.

Jin, D., Cho, K., Myun, C. L., Lim, Y., Lee, J., and Park, S. The impact of various ethanol–gasoline blends on particulates and unregulated gaseous emissions characteristics from a spark ignition direct injection (SIDI) passenger vehicle. *Fuel*, 2017, 209, 702–712.

Kang, E., Root, M., Toohey, D. W., and Brune, W. H. Introducing the concept of potential aerosol mass (PAM). *Atmospheric Chemistry and Physics*, 2007, 7, 5727–5744.

Karavalakis, G., Durbin, T. D., Shrivastava, M., Zheng, Z., Villela, M., and Jung, H. Impacts of ethanol fuel level on emissions of regulated and unregulated pollutants from a fleet of gasoline light-duty vehicles. *Fuel*, 2012, 93, 549–558.

Karavalakis, G., Short, D., Russell, R. L., Jung, H., Johnson, K. C., Asa-Awuku, A., and Durbin, T. D. Assessing the impacts of ethanol and iso-butanol on gaseous and particulate emissions from flexible fuel vehicles. *Environmental Science and Technology*, 2014b, 48, 14016–14024.

Karavalakis, G., Short, D., Vu, D., Villela, M., Asa-Awuku, A., and Durbin, T. D. Evaluating the regulated emissions, air toxics, ultrafine particles, and black carbon from SI-PFI and SI-DI vehicles operating on different ethanol and iso-butanol blends. *Fuel*, 2014a, 128, 410–421.

Kari, E., Hao, L., Ylisirnio, A., Buchholz, A., Leskinen, A., Yli-Pirila, P., Nuutinen, I., Kuuspalo, K., Jokiniemi, J., Faiola, C. L., Schobesberger S., and Virtanen, A. Potential dual effect of anthropogenic emissions on the formation of biogenic secondary organic aerosol (BSOA). *Atmospheric Chemistry and Physics*, 2019, 19, 15651–15671.

Karjalainen, P., Rönkkö, T., Pirjola, L., Heikkilä, J., Happonen, M., Arnold, F., Rothe, D., Bielaczyc, P., and Keskinen, J. Sulfur driven nucleation mode formation in diesel exhaust under transient driving conditions. Environmental Science and Technology, 2014, 48, 2336–2343.

Karjalainen, P., Timonen, H., Saukko, E., Kuuluvainen, H., Saarikoski, S., Aakko-Saksa, P., Murtonen, T., Dal Maso, M., Ahlberg, E., Svenningsson, B., Brune, W. H., Hillamo, R., Keskinen, J., and Rönkkö, T. Time-resolved characterization of primary and secondary particle emissions of a modern gasoline passenger car. *Atmospheric Chemistry and Physics*, 2016, 16, 8559–8470.

Khosousi, A., Liu, F., Dworkin, S. B., Eaves, N. A., Thomson, M. J., He, X., Dai, Y., Gao, Y., Liu, F., Shuai, S., and Wang, J. Experimental and numerical study of soot formation in laminar coflow diffusion flames off gasoline/ethanol blends. *Combustion and Flame*, 2015, 162, 3925–3933.

Kroll, J. H., and Seinfeld, J. H. Chemistry of secondary organic aerosol: Formation and evolution of low-volatility organics in the atmosphere. *Atmospheric Environment*, 2008, 42, 3593–3624.

Kroll, J. H., Donahue, N. M., Jimenez, J. L., Kessler, S. H., Canagaratna, M. R., Wilson, K. R., Altieri, K. E., Mazzoleni, L. R., Wozniak, A. S., Bluhm, H., Mysak, E. R., Smith, J. D., Kolb, C. E., and Worsnop, D. R. Carbon oxidation state as a metric for describing the chemistry of atmospheric organic aerosol. *Nature Chemistry*, 2011, 3, 133–139.

Kuittinen, N., McCaffery, C., Peng, W., Zimmerman, S., Roth, P., Simonen, P., Karjalainen, P., Keskinen, J., Cocker, D. R., Durbin, T. D., Rönkkö, T., Bahreini, R., and Karavalakis, G. Effects of driving conditions on secondary aerosol formation from a GDI vehicle using an oxidation flow reactor. *Environmental Pollution*, 2021, 282, 117069.

Lambe, A. T., Ahern, J. P. D., Brune, W. H., Ng, N. L., Wright, J. P., Croasdale, D. R., Worsnop, D. R., Davidovits, P., and Onasch, T. B. Characterization of aerosol photooxidation flow reactors: Heterogeneous oxidation, secondary organic aerosol formation, and cloud condensation nuclei activity measurements. *Atmospheric Measurement Techniques*, 2011, 4, 445–461.

Lemaire, R., Therssen, E., and Desgroux, P. Effect of ethanol addition in gasoline and gasoline-surrogate on soot formation in turbulent spray flames. *Fuel*, 2010, 89, 3952–3959.

Link, M. F., Kim, J., Park, G., Lee, T., Park, T., Babar, Z. B., Sung, K., Kang, S., Kim, J. S., Choi, Y., Son, J., Lim, H. J., and Farmer, D. K. Elevated production of NH_4NO_3 from the photochemical processing of vehicle exhaust: Implications for air quality in the Seoul metropolitan region. *Atmospheric Environment*, 2017, 156, 95–101.

Liu, C., Liu, Y., Chen, T., Liu, J., and He, H. Rate constant and secondary organic aerosol formation from the gas-phase reaction of eugenol with hydroxyl radicals. *Atmospheric Chemistry and Physics*, 2019, 19, 2001–2013.

Liu, T., Wang, X., Deng, W., Hu, Q., Ding, X., Zhang, Y., He, Q., Zhang, Z., Lu, S., Bi, X., Chan, J., and Yu, J. Secondary organic aerosol formation from photochemical aging of light-duty gasoline vehicle exhausts in a smog chamber. *Atmospheric Chemistry and Physics*, 2015, 15, 9049–9062.

Maricq, M. M., Chase, R. E., Xu, N., and Podsiadlik, D. H. The effects of the catalytic converter and fuel sulfur level on motor vehicle particulate matter emissions: Gasoline vehicles. *Environmental Science and Technology*, 2002, 36, 276–282.

Maricq, M. M., Szente, J. J., Harwell, A. L., and Loos, M. J. Impact of aggressive drive cycles on motor vehicle exhaust PM emissions. *Journal of Aerosol Science*, 2017, 113, 1–11.

Maricq, M. M., Szente, J. J., and Jahr, K. The impact of ethanol fuel blends on PM emissions from a light-duty GDI vehicle. *Aerosol Science and Technology*, 2012, 46, 576–583.

McCaffery, C., Durbin, T. D., Johnson, K. C., and Karavalakis, G. The effect of ethanol and iso-butanol blends on polycyclic aromatic hydrocarbon (PAH) emissions from PFI and GDI vehicles. *Atmospheric Pollution Research*, 2020, 11, 2056–2067.

Middlebrook, A. M., Bahreini, R., Jimenez, J. L., and Canagaratna, M. R. Evaluation of composition-dependent collection efficiencies for the aerodyne aerosol mass spectrometer using field data. *Aerosol Science and Technology*, 2012, 46, 258–271.

Miersch, T., Czech, H., Stengel, B., Abbaszade, G., Orasche, J., Sklorz, M., Streibel, T., and Zimmermann, R. Composition of carbonaceous fine particulate emissions of a flexible fuel DISI engine under high velocity and municipal conditions. *Fuel*, 2019, 236, 1465–1473.

Ng, N. L., Canagaratna, M. R., Zhang, Q., Jimenez, J. L., Tian, J., Ulbrich, I. M., Kroll, J. H., Docherty, K. S., Chhabra, P. S., Bahreini, R., Murphy, S. M., Seinfeld, J. H., Hildebrandt, L., Donahue, N. M., DeCarlo, P. F., Lanz, V. A., Prevot, A. S. H., Dinar, E., Rudich, Y., and Worsnop, D. R. Organic aerosol components observed in Northern Hemispheric datasets from aerosol mass spectrometry. *Atmospheric Chemistry and Physics*, 2010, 10, 4625–4641.

Nordin, E. Z., Eriksson, A. C., Roldin, P., Nilsson, P. T., Carlsson, J. E., Kajos, M. K., Hellén, H., Wittbom, C., Rissler, J., Löndahl, J., Swietlicki, E., Svenningsson, B., Bohgard, M., Kulmala, M., Hallquist, M., and Pagels, J. H. Secondary organic aerosol formation from idling gasoline passenger vehicle emissions investigated in a smog chamber. *Atmospheric Chemistry and Physics*, 2013, 13, 6101–6116.

Ortega, A. M., Hayes, P. L., Peng, Z., Palm, B. B., Hu, W., Day, D. A., Li, R., Cubison, M. J., Brune, W. H., Graus, M., Warneke, C., Gilman, J. B., Kuster, W. C., de Gouw, J., Gutiérrez-Montes, C., and Jimenez, J. L. Real-time measurements of secondary organic aerosol formation and aging from ambient air in an oxidation flow reactor in the Los Angeles area. *Atmospheric Chemistry and Physics*, 2016, 16, 7411–7433.

Peng, J., Hu, M., Du, Z., Wang, Y., Zheng, J., Zhang, W., Yang, Y., Qin, Y., Zheng, R., Xiao, Y., Wu, Y., Lu, S., Wu, Z., Guo, S., Mao, H., and Shuai, S. Gasoline aromatics: A critical determinant of urban secondary organic aerosol formation. *Atmospheric Chemistry and Physics*, 2017, 17, 10743–10752.

Pieber, S. M., Kumar, N. K., Klein, F., Comte, P., Bhattu, D., Dommen, J., Bruns, E. A., Kilic, D., El Haddad, I., Keller, A., Czerwinski, J., Heeb, N., Baltensperger, U., Slowik, J. G., and Prévôt, A. S. H. Gas-phase composition and secondary organic aerosol formation from standard and particle filter-retrofitted gasoline direct injection vehicles investigated in a batch and flow reactor. *Atmospheric Chemistry and Physics*, 2018, 18, 9929–9954.

Pirjola, L., Karjalainen, P., Heikkilä, J., Saari, S., Tzamkiozis,T., Ntziachristos, L., Kulmala, K., Keskinen, J., and Rönkkö, T. Effects of fresh lubricant oils on particle emissions emitted by a modern gasoline direct injection passenger car. *Environmental Science and Technology*, 2015, 49, 3644−3652.

Platt, S. M., El Haddad, I., Pieber, S. M., Zardini, A. A., Suarez-Bertoa, R., Clairotte, M., Daellenbach, K. R., Huang, R. J., Slowik, J. G., Hellebust, S., Temime-Roussel, B., Marchand, N., de Gouw, J., Jimenez, J. L., Hayes, P. L., Robinson, A. L., Baltensperger, U., Astorga, C., and Prévôt, A. S. H. Gasoline cars produce more carbonaceous particulate matter than modern filter-equipped diesel cars. *Scientific Reports*, 2017, 7, 4926, doi: 10.1038/s41598-017-03714-9.

Platt, S. M., El Haddad, I., Zardini, A. A., Clairotte, M., Astorga, C., Wolf, R., Slowik, J. G., Temime-Roussel, B., Marchand, N., Ježek, I., Drinovec, L., Močnik, G., Möhler, O., Richter, R., Barmet, P., Bianchi, F., Baltensperger, U., and Prévôt, A. S. H. Secondary organic aerosol formation from gasoline vehicle emissions in a new mobile environmental reaction chamber. *Atmospheric Chemistry and Physics*, 2013, 13, 9141–9158.

Robinson, A. L., Donahue, N. M., Shrivastava, M. K., Weitkamp, E. A., Sage, A. M., Grieshop, A. P., Lane, T. E., Pierce, J. R., and Pandis, S. N. Rethinking organic aerosols: Semivolatile emissions and photochemical aging. *Science*, 2007, 315, 1259–1262.

Roth, P., Yang, J., Fofie, E., Cocker, D. R., Durbin, T. D., Brezny, R., Geller, M., Asa-Awuku, A., and Karavalakis, G. Catalyzed gasoline particulate filters reduce secondary organic aerosol production from gasoline direct injection vehicles. *Environmental Science and Technology*, 2019, 53, 3037–3047.

Roth, P., Yang, J., Peng, W., Cocker, D. R., Durbin, T. D., Asa-Awuku, A., and Karavalakis G. Intermediate and high ethanol blends reduce secondary organic aerosol formation from gasoline direct injection vehicles. *Atmospheric Environment*, 2020b, 220, 117064.

Roth, P., Yang, J., Stamatis, C., Barsanti, K. C., Cocker, D. R., Durbin, T. D., Asa-Awuku, A., and Karavalakis, G. Evaluating the relationships between aromatic and ethanol levels in gasoline on secondary aerosol formation from a gasoline direct injection vehicle. *Science of The Total Environment*, 2020a, 737, 140333.

Saha, P. K., Reece, S. M., and Grieshop, A. P. Seasonally varying secondary organic aerosol formation from in-situ oxidation of near-highway air. *Environmental Science and Technology*, 2018, 52, 7192–7202.

Saliba, G., Saleh, R., Zhao, Y., Presto, A. A., Lamber, A. T., Frodin, B., Sardar, S., Maldonado, H., Maddox, C., May, A. A., Drozd, G. T., Goldstein, A. H., Russell, L. M., Hagen, F., and Robinson, A. L. Comparison of gasoline direct injection (GDI) and port fuel injection (PFI) vehicle emissions: Emission certification standards, cold-start, secondary organic aerosol formation potential, and potential climate impacts. *Environmental Science and Technology*, 2017, 51, 6542–6552.

Sgro, L. A., Sementa, P., Vaglieco, B. M., Rusciano, G., D'Anna, A., and Minutolo, P. Investigating the origin of nuclei particles in GDI engine exhausts. *Combustion and Flame*, 2012, 159, 1687–1692.

Simonen, P., Kalliokoski, J., Karjalainen, P., Rönkkö, T., Timonen, H., Saarikoski, S., Aurela, M., Bloss, M., Triantafyllopoulos, G., Kontses, A., Amanatidis, S., Dimaratos, A., Samaras, Z., Keskinen, J., Dal Maso, M., and Ntziachristos, L. Characterization of laboratory and real driving emissions of individual Euro 6 light-duty vehicles—Fresh particles and secondary aerosol formation. *Environmental Pollution*, 2019, 255, 113175.

Simonen, P., Saukko, E., Karjalainen, P., Timonen, H., Bloss, M., Aakko-Saksa, P., Rönkkö, T., Keskinen, J., and Dal Maso, M. A new oxidation flow reactor for measuring secondary aerosol formation of rapidly changing emission sources. *Atmospheric Measurement Techniques*, 2017, 10, 1519–1537.

Suarez-Bertoa, R., Zardini, A. A., and Astorga, C. Ammonia exhaust emissions from spark ignition vehicles over the New European Driving Cycle. *Atmospheric Environment*, 2014, 92 43–53.

Timonen, H., Karjalainen, P., Saukko, E., Saarikoski, S., Aakko-Saksa, P., Simonen, P., Murtonen, T., Maso, M. D., Kuuluvainen, H., Bloss, M., Ahlberg, E., Svenningsson, B., Pagels, J., Brune, W. H., Keskinen, J., Worsnop, D. R., Hillamo, R., and Rönkkö, T. Influence of fuel ethanol content on primary emissions and secondary aerosol formation potential for a modern flex-fuel gasoline vehicle. *Atmospheric Chemistry and Physics*, 2017, 17, 5311–5329.

Tkacik, D. S., Lambe, A. T., Jathar, S., Li, X., Presto A. A., Zhao, Y., Blake, D., Meinardi, S., Jayne, J. T., Croteau, P. L., and Robinson, A. L. Secondary organic aerosol formation from in-use motor vehicle emissions using a potential aerosol mass reactor. *Environmental Science and Technology*, 2014, 48, 11235–11242.

Vu, D., Roth, P., Berte, T., Yang, J., Cocker, D., Durbin, T., Karavalakis, G., and Asa-Awuku, A. Using a new mobile atmospheric chamber (MACh) to investigate the formation of secondary aerosols from mobile sources: The case of gasoline direct injection vehicles. *Journal of Aerosol Science*, 2019, 133, 1–11.

Vu, K. T., Dingle, J. H., Bahreini, R., Reddy, P. J., Apel, E. C., Campos, T. L., DiGangi, J. P., Diskin, G. S., Fried, A., Herndon, S. C., Hills, A. J., Hornbrook, R. S., Huey, G., Kaser, L., Montzka, D. D., Nowak, J. B., Pusede, S. E., Richter, D., Roscioli, J. R., Sachse, G. W., Shertz, S., Stell, M., Tanner, D., Tyndall, G. S., Walega, J., Weibring, P., Weinheimer, A. J., Pfister, G., and Flocke, F. Impacts of the Denver cyclone on regional air quality and aerosol formation in the Colorado Front Range during FRAPPÉ 2014. *Atmospheric Chemistry and Physics*, 2016, 16, 12039–12058.

Yang, J., Roth, P., Durbin, T., and Karavalakis, G. Impacts of gasoline aromatic and ethanol levels on the emissions from GDI vehicles: Part 1. Influence on regulated and gaseous toxic pollutants. *Fuel*, 2019a, 252, 799–811.

Yang, J., Roth, P., Ruehl, C. R., Shafer, M. M., Antkiewicz, D. S., Durbin, T. D., Cocker, D., Asa-Awuku, A., and Karavalakis, G. Physical, chemical, and toxicological characteristics of particulate emissions from current gasoline direct injection vehicles. *Science of The Total Environment*, 2019a, 650, 1182–1194.

Yang, J., Roth, P., Zhu, H., Durbin, T. D., and Karavalakis, G. Impacts of gasoline aromatic and ethanol levels on the emissions from GDI vehicles: Part 2. Influence on particulate matter, black carbon, and nanoparticle emissions. *Fuel*, 2019b, 252, 812–820.

Yao, C., Dou, Z., Wang, B., Liu, M., Lu, H., Feng, J., and Feng, L. Experimental study of the effect of heavy aromatics on the characteristics of combustion and ultrafine particle in DISI engine. *Fuel*, 2017, 203, 290–297.

Zhang, Y., Deng, W., Hu, Q., Wu, Z., Yang, W., Zhang, H., Wang, Z., Fang, Z., Zhu, M., Li, S., Song, W., Ding, X., and Wang, X. Comparison between idling and cruising gasoline vehicles in primary emissions and secondary organic aerosol formation during photochemical aging. *Science of The Total Environment*, 2020, 722, 137934.

Zhao, Y., Lamber, A. T., Saleh, R., Saliba, G., and Robinson, A. L. Secondary organic aerosol production from gasoline vehicle exhaust: Effects of engine technology, cold start, and emission certification standard. *Environmental Science and Technology*, 2018, 52, 1253–1261.

Zhao, Y., Saleh, R., Saliba, G., Presto, A. A., Gordon, T. D., Drozd, G. T., Goldstein, A. H., Donahue, N. M., and Robinson, A. L. Reducing secondary aerosol formation from gasoline vehicle exhaust. Proceedings of the National Academy of Sciences of the United States of America, 2017, 114, 6984–6989.

Zhu, R., Hu, J., Bao, X., He, L., and Zu, L. Effects of aromatics, olefins, and distillation temperatures (T50 and T90) on particle mass and number emissions from gasoline direct injection (GDI) vehicles. *Energy Policy*, 2017, 101, 185–193.

Zimmerman, N., Rais, K., Jeong, C. H., Pant, P., Delgado-Saborit, J. M., Wallace, J. S., Evans, G. J., Brook, J. R., Godri, and Pollitt, K. J. Carbonaceous aerosol sampling of gasoline direct injection engine exhaust with an integrated organic gas and particle samples. *Science of The Total Environment*, 2019, 652, 1261–1269.

Supplementary Material A

Driving Cycles

The vehicle was exercised in duplicate runs over several different driving cycles, including regulated and non-regulated driving schedules. The FTP is the cycle for emission certification of light-duty vehicles in the United States. It includes three phases (i.e., cold-start, urban, and hot-start phases) with a maximum speed of 57 mi/hr. The NEDC has been used for emission certification of light-duty vehicles in Europe. The entire cycle includes four ECE segments (known as urban driving cycle [UDC]) repeated without interruption, followed by one extra-urban driving cycle (EUDC). UDC is characterized by low-speed and vehicle-load conditions (up to 31 mi/hr), whereas EUDC accounts for more aggressive, high-speed driving (up to 74.6 mi/hr). The LA92 cycle (also known as the California Unified Cycle) was developed by CARB to represent typical driving behavior in California. It has a similar three-phase structure as the FTP, but is a more aggressive driving cycle with higher speed and acceleration, fewer stops, and less idle time. The US06 Supplemental FTP (referred to as US06) represents aggressive, high-speed and high-acceleration driving behavior (maximum speed of 80.3 mi/hr). The HWFET is a chassis dynamometer driving schedule developed by U.S. EPA for the determination of the fuel economy of light-duty vehicles.

Two less known driving schedules were also employed in this study. These cycles were developed by Caltrans to better represent typical driving patterns in California freeways. Emission measurements from on-road vehicles are used to feed the EF model of CARB. In reality, these EFs can be subjected to high levels of uncertainty due to the absence of supporting measurement data, as well as due to the absence of data concerning the vehicle miles traveled (VMT) above 65 mi/hr. In California, more than 50 percent of freeway VMT is at a speed above 65 mi/hr, and more than 40 percent of the total VMT occurs on interstates and freeways (PeMS). The cycles (referred to as Caltrans 1 and Caltrans 2) derived from field driving data representative of freeway, arterial, collector, and local driving, and traffic congestion levels typically found on Los Angeles freeways. The mean and maximum speed are 53.8 mi/hr and 90 mi/hr for Caltrans 1 and 50.7 mi/hr and 73.2 mi/hr for Caltrans 2, respectively. Figure SM1 illustrates the speed-time profiles for all driving cycles.

Photooxidation Experimental Setup

The exhaust was drawn from the CVS to TSAR through an ejector diluter (nominal dilution ratio of 7:1) to provide additional dilution and bring exhaust concentration to suitable levels before the oxidation. Total phase-specific dilution factors before TSAR varied from 45 to 172. Additional dilution air was fed through a mass flow controller after TSAR to stabilize the flow through TSAR to 5 lpm, while still providing enough sample for the online instruments, resulting in an additional dilution ratio of 3.4:1. Propane tracer gas measurements were executed to verify the dilution ratios. In order to estimate the OH exposure in the TSAR oxidation flow reactor, the RH sensor was placed between the mixing tube and oxidation regions of the flow reactor. An ozone (O_3) analyzer (2B Dual Beam Ozone analyzer) was used to monitor O_3 concentrations of the sample before and after the UV lights were turned on. Before and after the driving cycles, background measurements were made from the CVS dilution air, with and without aging the sample. The background concentrations obtained from the oxidation of tracer gases in the dilution air were negligible and subtracted from aged aerosol mass concentrations.

The OH exposure and corresponding atmospheric age of the sample after oxidation were estimated by applying a chemical reaction model similarly to Simonen et al. (2017). The model has been adapted based on a model created for the PAM in the PAM users' manual (PAM_chem_v8 by William Brune, https://sites.google.com/site/pamusersmanual/7-pam-photochemistry-model/a-introduction). The model takes as an input the measured RH, temperature, and O_3 data as well as the measured concentrations of NOx, NMHC, and CO. Trace gas concentrations are corrected with a time convolution function as described in Simonen et al. (2017) to account for the residence time in the TSAR inlet and mixing regions. Because only total NOx was measured, it was assumed that 10 percent of the NOx was NO_2, as recently reported by Suarez-Bertoa et al. (2019), who reported that NO_2 comprised 2–10 percent of the NOx real driving emissions for GDI vehicles. In addition, the

detailed composition of organic precursors was not directly measured in this study, and it was assumed that the specific compounds adding up to NMHC followed the distribution of different hydrocarbon species measured by Timonen et al. (2017) for a gasoline vehicle operated on E10 during a cold-start UDC cycle. The initial OH reactivity for each time step in the model was then calculated from the concentrations and OH rate coefficients of the specific precursors. The OH exposures were calculated, and the cycle-averaged values along with equivalent oxidation days (assuming daily OH concentration of 1.5×10^6 molecule cm^{-3}) are shown in Table SM1. As shown in Figure SM2, the OH exposures and atmospheric ages varied within the cycles, typically at their lowest during the cold-start conditions.

In contrast to previous studies with the TSAR (Simonen et al., 2017; Timonen et al., 2017), for this study the unit was equipped with light-intensity control for the UV lamps. To monitor the light intensity, photodiodes sensitive to visible light were placed close to each UV lamp and their voltages were continuously logged. The photon flux at 254 nm was 1.92×10^{15} $cm^{-3}s^{-1}$ with the lamps set to 70 percent intensity. The water-mixing ratio calculated from RH stayed between 2.4–3.6 percent, except in one of the US06 runs, when high mixing ratios between 8.8–9.4 percent were achieved. According to the flow reactor operation regimes introduced by Peng and Jimenez (2017) and based on the modeled external OH reactivity (OHR_{ext}) and NO mixing ratios within TSAR (Figure SM3), oxidation conditions in the TSAR mostly remained within the Good-Low NO operation regime defined for the high water-mixing ratio and medium photon flux reactor (HM case).

mAMS Data Synthesis

Ng et al. (2011) provided a simple method to determine the concentration of HOA:

$$HOA \sim 13.4 \times (C_{57} - 0.1 \times C_{44})$$

where C_{57} and C_{44} are the unit-mass resolution concentrations at *m/z* 57 and *m/z* 44, respectively. As explained by Ng et al. (2011), a fraction of C_{44} is subtracted to correct for the contribution of oxygenated species at *m/z* 57 (e.g., $C_3H_5O^+$), which in ambient data is measurable but not significant. However, the high-resolution analysis of the spectra in the current experiments indicate that the concentration of $C_3H_5O^+$ overwhelmed that of $C_4H_9^+$; therefore, the researchers modified the equation above and estimated the HOA mass concentration using just the high-resolution-based concentration of the hydrocarbon-like ion at *m/z* 57 (i.e., $C_4H_9^+$) using the following equation:

$$HOA \sim 13.4 \times C_{C4H9+}$$

The remaining mass of OA was then assigned to SOA. Given the experimental setup in this work, the research team could only determine the concentration of HOA that remained after oxidation, and therefore could not estimate how much HOA was present in the exhaust.

To further gain insights into the oxidation extent of OA, fractional contribution of ions at *m/z* 43 (dominated by $C_2H_3O^+$ ion originating from carbonyl functional groups) and at *m/z* 44 (dominated by CO_2^+ ion originating from carboxylic acid, ester, or peroxide functional groups) to total OA are also presented (f_{43} and f_{44}, respectively). Additionally, these fractions are used in the following equations to calculate the elemental ratios of O:C and H:C (Canagatatna et al., 2015) so that an overall average carbon oxidation state (OS_c) can be estimated (Kroll et al., 2011):

$$O{:}C = 0.079 + 4.31 \times f_{44}$$
$$H{:}C = 1.12 + 6.74 \times f_{43} - 17.77 \times (f_{43})^2$$
$$OS_c \sim 2 \times O{:}C - H{:}C$$

Last, to distinguish between the nitrate mass originating from organonitrate functional groups versus inorganic nitrate, the high-resolution nitrate fragmentation ratio at *m/z* 30 and *m/z* 46 (i.e., NO^+ to NO_2^+) is explored, with

the understanding that organonitrates fragment more favorably to NO^+, leading to a higher NO^+/NO_2^+ ratio (R_{ON}) compared to that when sampling ammonium nitrate (R_{AN}). If R_{ON} for relevant pure organonitrates are known, one can determine the fraction of the measured nitrate that is due to organonitrate functional groups; however, the range of literature values for anthropogenic alkene-derived R_{ON} is large (about 1.8–4.6), preventing the researchers from determining the fraction confidently (Farmer et al., 2010). The research team therefore used the observed NO^+/NO_2^+ ratio qualitatively to identify conditions when the formation of organonitrates was likely.

Calculation of Emission Factors

EFs for primary PM and mAMS species were calculated by first correcting the measured concentrations by dilution to the CVS concentrations. Mass flows for each species were calculated based on the mixing volume in the CVS and integrated over each phase of the cycle and divided by the distance traveled to calculate phase-specific EFs per miles traveled. A similar method was applied to calculate the total EF, except in the case of the FTP and LA92 cycles, for which weighting factors were applied for the different phases of the cycles according to the CFR specifications: 0.43 for the cold-start transient phase, 1.0 for the stabilized phase, and 0.57 for the hot-start transient phase.

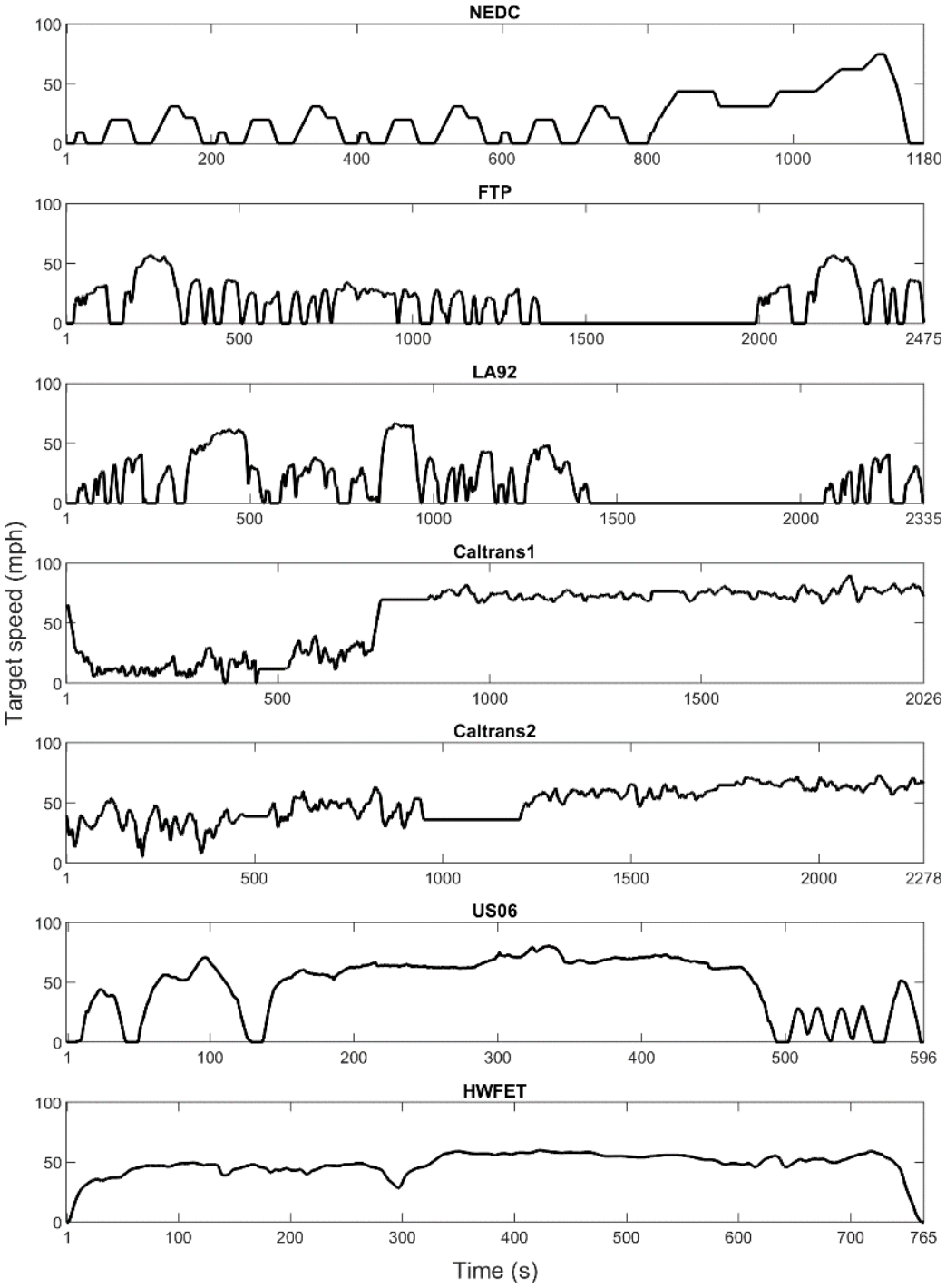

Figure SM1. Speed-time profiles of the driving cycles.

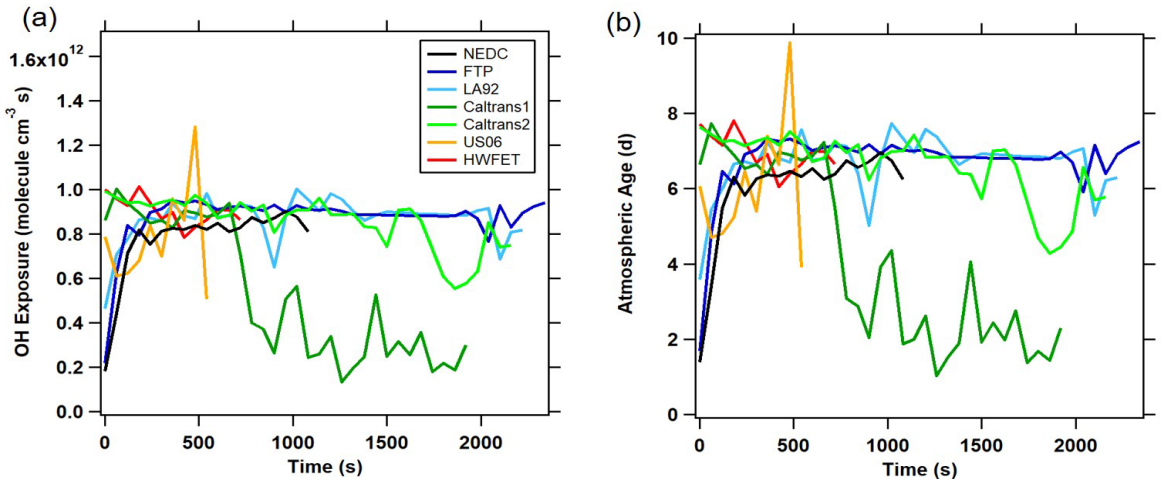

Figure SM2. Modeled OH exposure and equivalent atmospheric age assuming daily OH concentration of 1.5×10^6 molecule cm^{-3} (a), and within TSAR during different driving cycles (b).

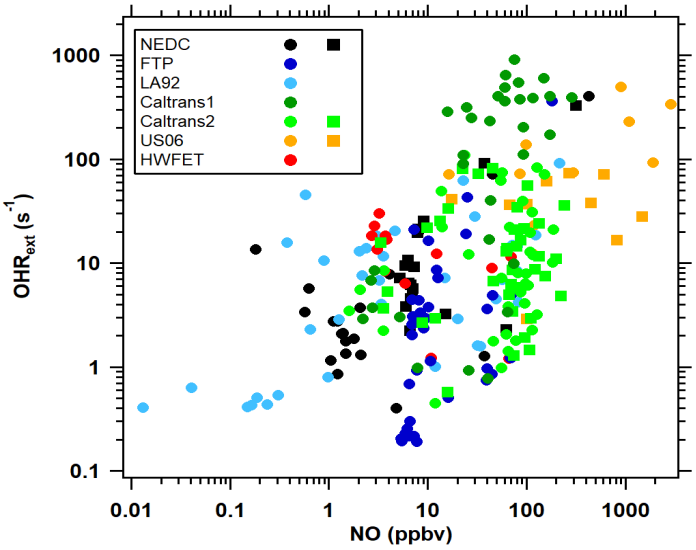

Figure SM3. Modeled external OH reactivity in TSAR during different driving cycles.

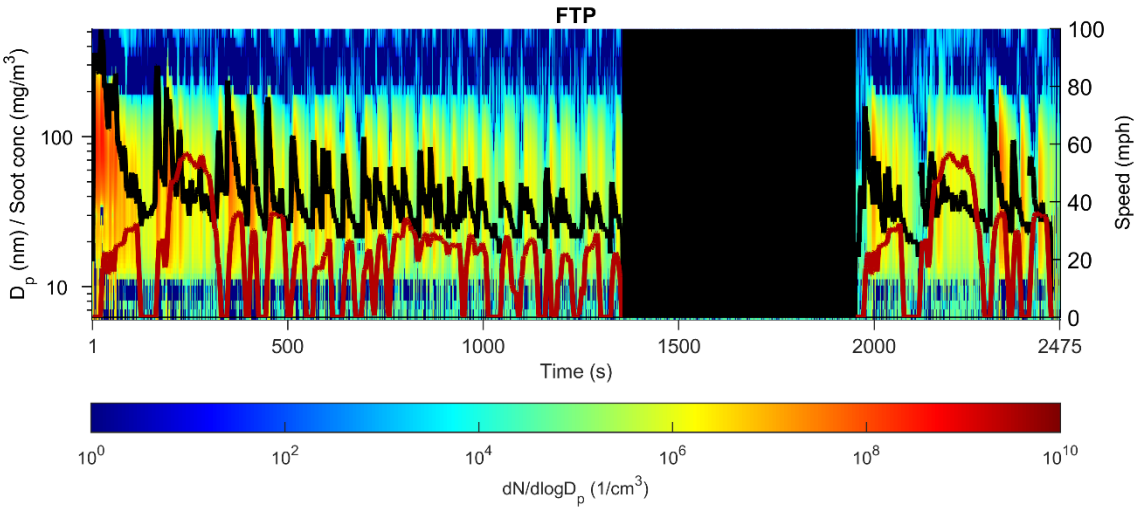

Note: The figure presents soot concentrations measured by MSS (black line, left y-axis; note the logarithmic scale), and vehicle speed (red line, right y-axis). The concentrations shown have been corrected by dilution to represent tailpipe concentrations. The FTP cycle was a single measurement.

Figure SM4. Particle size distribution and soot mass concentrations for the FTP cycle.

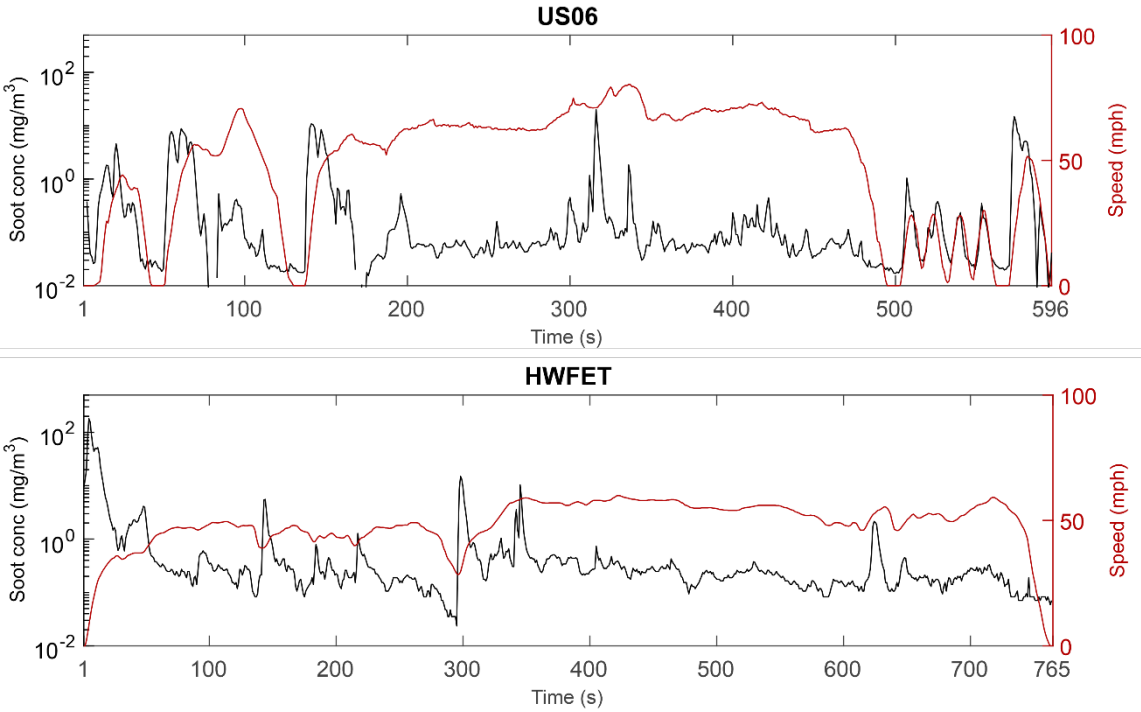

Note: The concentrations shown have been corrected by dilution to represent tailpipe concentrations. For US06, the results are averages for duplicate runs. The HWFET was a single test.

Figure SM5. Real-time soot mass concentrations over the US06 and HWFET cycles.

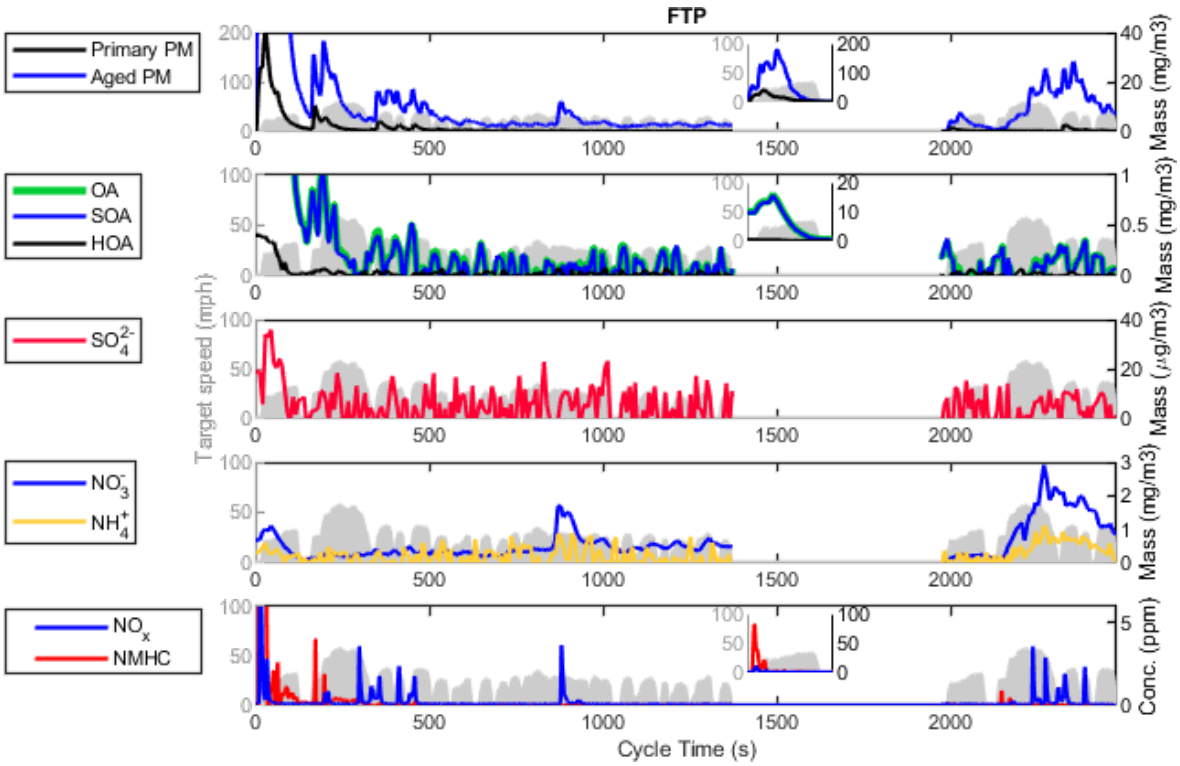

Note: For comparison, primary PM measured by EEPS are shown corrected with time convolution caused by residence time in the TSAR chamber. The subfigures inside the plots show concentrations during the first 150 s of the cold-start cycle. The concentrations shown have been corrected by dilution to represent tailpipe concentrations.

Figure SM6. Time-series of primary and aged PM, OA, SOA, HOA, sulfate, ammonium, and nitrate ions, and tailpipe NMHC and NOx concentrations over the FTP cycle.

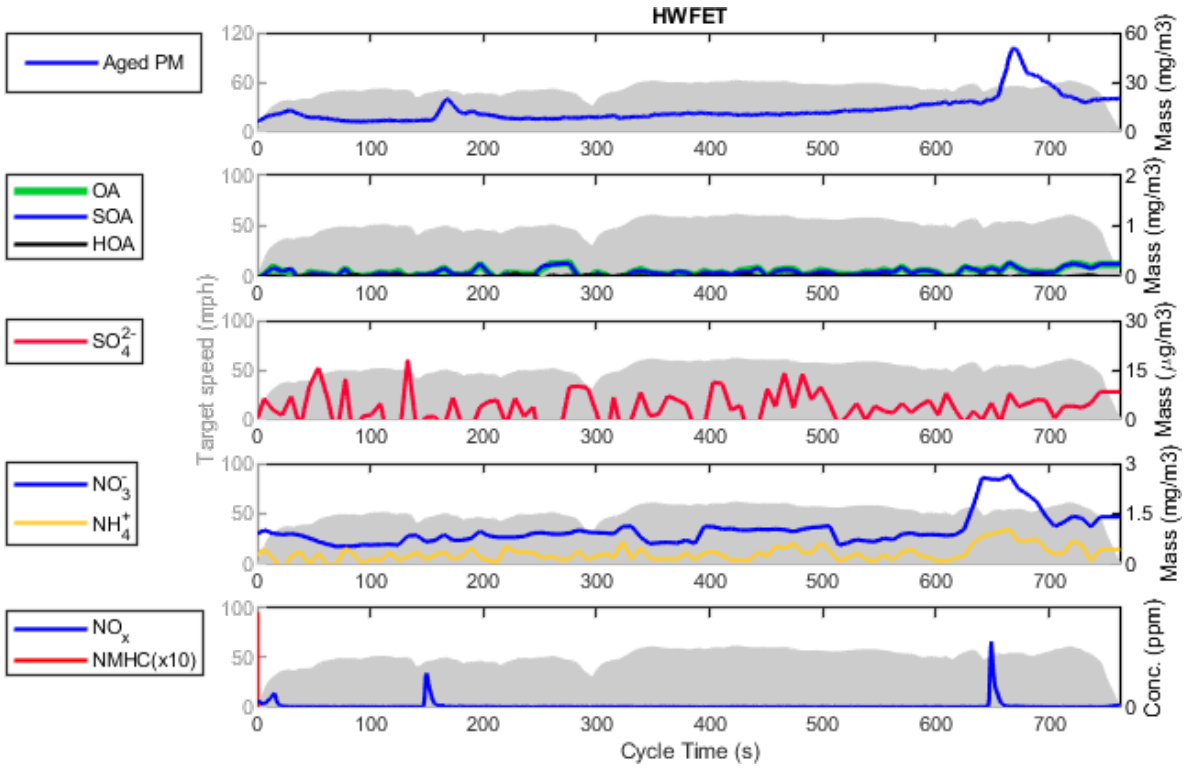

Note: The concentrations shown have been corrected by dilution to represent tailpipe concentrations.

Figure SM7. Time-series of primary and aged PM, OA, SOA, HOA, sulfate, ammonium, and nitrate ions, and tailpipe NMHC and NOx concentrations over the HWFET cycle.

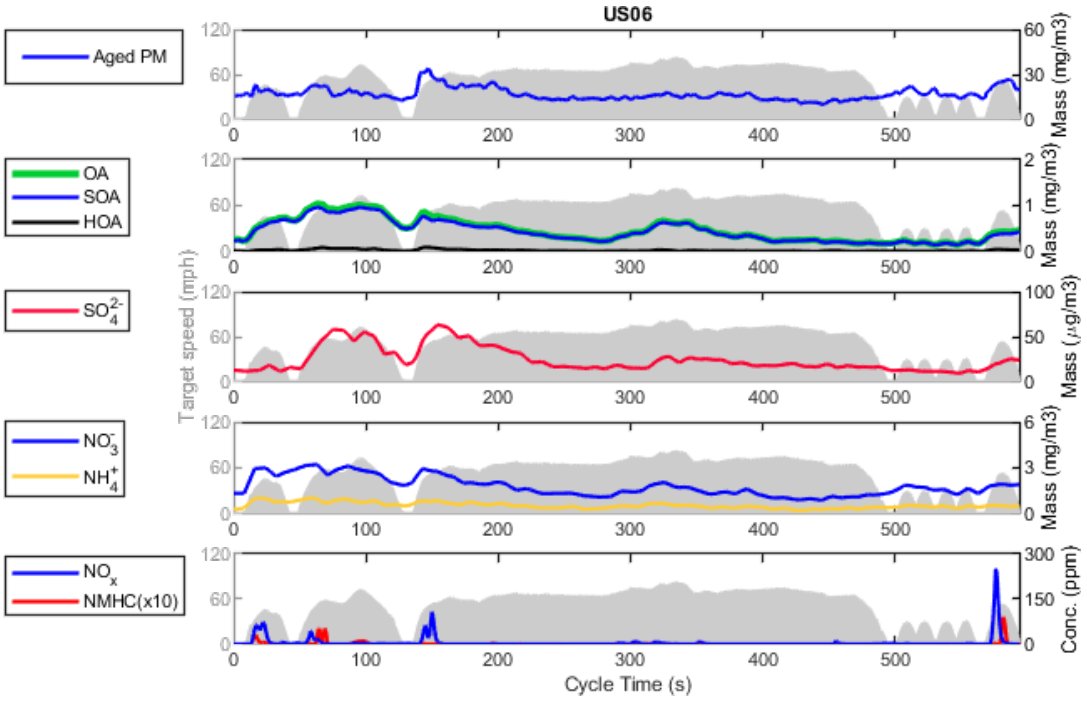

Note: The concentrations shown have been corrected by dilution to represent tailpipe concentrations.

Figure SM8. Time-series of primary and aged PM, OA, SOA, HOA, sulfate, ammonium, and nitrate ions, and tailpipe NMHC and NOx concentrations over the US06 cycle.

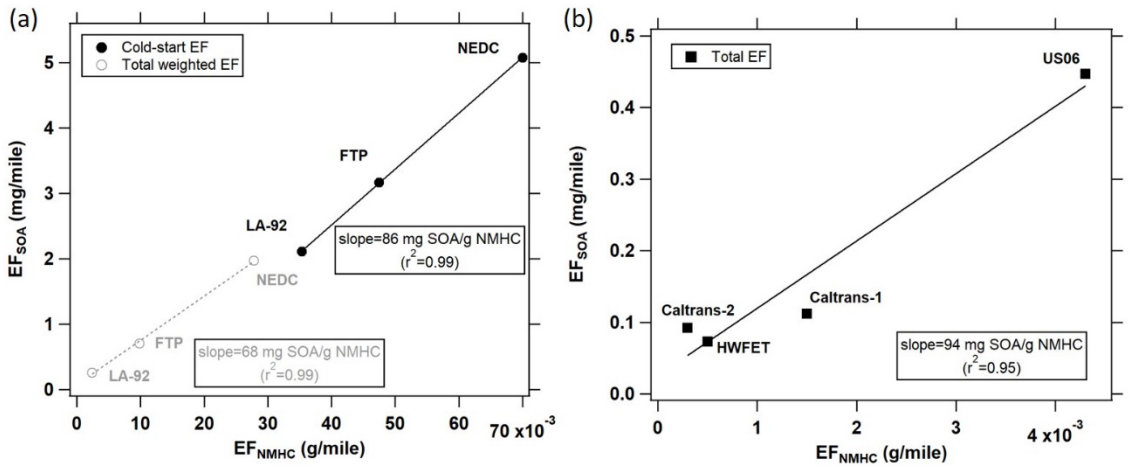

Figure SM9. Correlations between EFSOA and EFNMHC during (a) the cold-start phase and all phases of cold-start driving cycles and (b) the hot-start cycles.

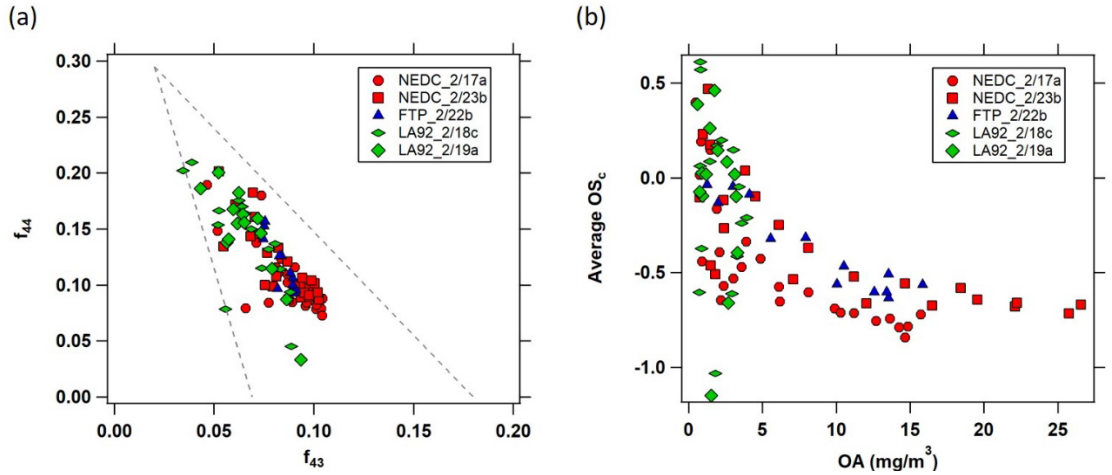

Note: The dashed lines in (a) display the boundary of previously observed ambient OOA data (Ng et al., 2010).

Figure SM10. (a) Scatter plot of the fraction of OA signal from m/z 44 (f_{44}) and m/z 43 (f_{43}) during the cold start of NEDC, FTP, and LA92 drive cycles and (b) estimated average carbon oxidation state (OSc) of OA during the cold start of NEDC, FTP, and LA92 drive cycles.

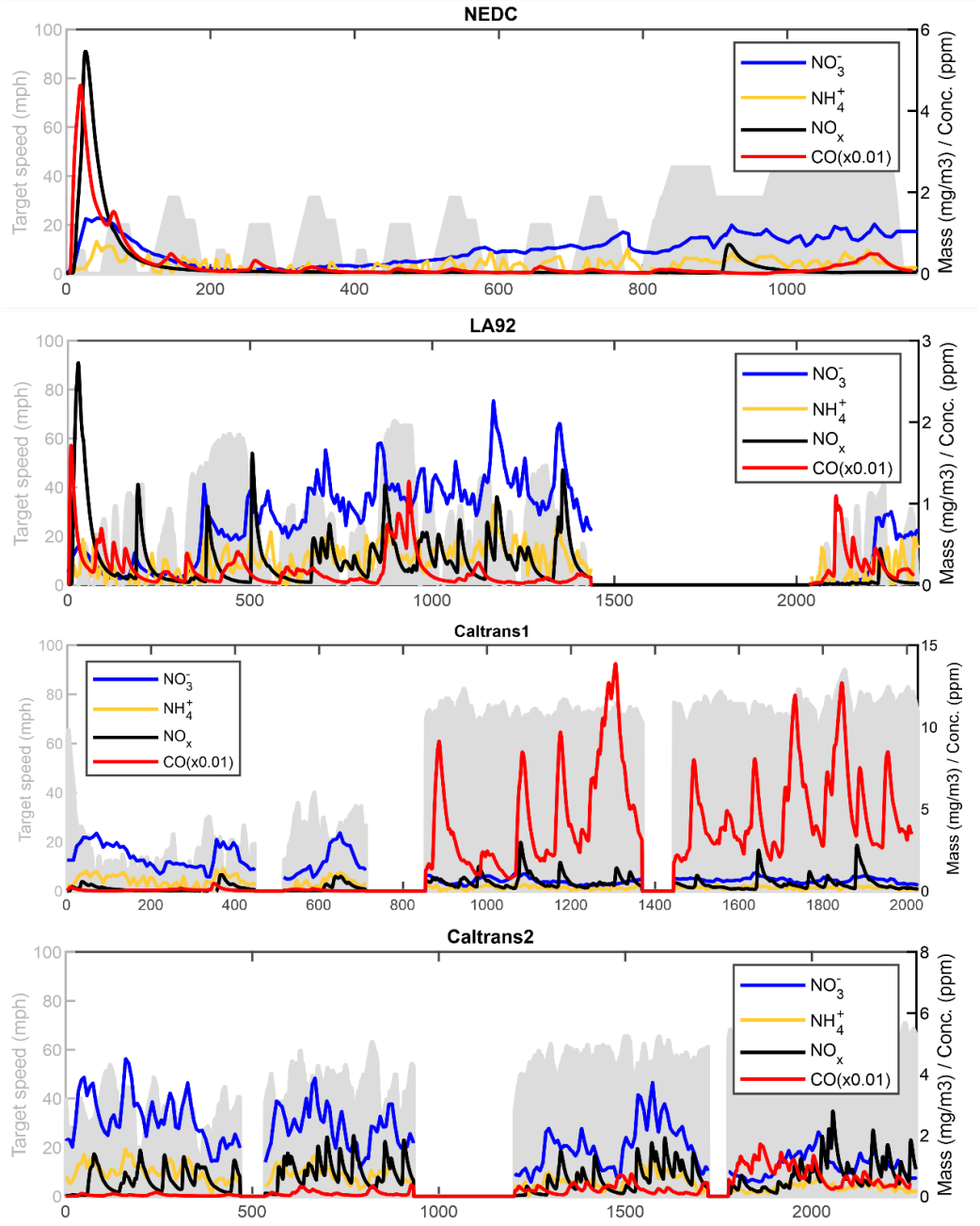

Figure SM11. Time-series of nitrate and ammonium ions, and tailpipe NOx and CO emissions over the NEDC, LA92, Caltrans 1, and Caltrans 2 cycles.

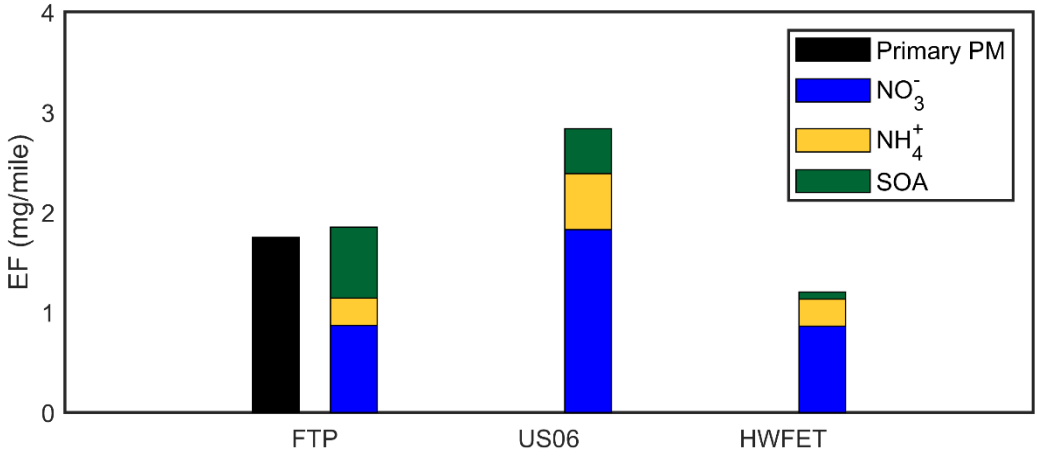

Note: EEPS data are not available for US06 and HWFET cycles.

Figure SM12. Emission factors for primary PM measured by EEPS and aged NO_3^-, NH_4^+, and SOA measured by mAMS for FTP, US06, and HWFET cycles.

Table SM1. Average OH Exposures and the Corresponding Photochemical Ages during the Different Test Cycles

Cycle	RH (%)	Temperature (°C)	UV Actinic Flux (cm^{-2} s^{-1})	Initial O_3 (ppm)	Cycle-Averaged OH Exposure (molecule cm^{-3})	Atmospheric Age (days)
Caltrans 1	27.0	19.8	1.92E+15	36.9	5.31E+11	4.10
Caltrans 2	27.0	20.1	1.92E+15	35.8	8.56E+11	6.61
FTP	23.8	19.9	1.92E+15	36.7	8.72E+11	6.73
HWFET	29.4	19.5	1.92E+15	34.0	9.04E+11	6.98
LA92	23.9	20.2	1.92E+15	38.4	8.65E+11	6.68
NEDC	23.3	19.7	1.92E+15	32.4	7.73E+11	5.96
US06	52.3	19.5	1.92E+15	27.6	7.84E+11	6.05

References

Caltrans Performance Measurement System (PeMS), http://pems.dot.ca.gov/

Canagaratna, M. R., Jimenez, J. L., Kroll, J. H., Chen, Q., Kessler, S. H., Massoli, P., Hildebrandt Ruiz, L., Fortner, E., Williams, L. R., Wilson, K. R., Surratt, J. D., Donahue, N. M., Jayne, J. T., and Worsnop, D. R. Elemental ratio measurements of organic compounds, using aerosol mass spectrometry: Characterization, improved calibration, and implications. *Atmospheric Chemistry and Physics*, 2015, 14, 253–272.

Farmer, D. K., Matsunaga, A., Docherty, K. S., Surratt, J. D., Seinfeld, J. H., Ziemann, P. J., Jimenez, J. L. Response of an aerosol mass spectrometer to organonitrates and organosulfates and implications for atmospheric chemistry. Proceedings of the National Academy of Sciences of the United States of America, 2010, 107, 6670–6675.

Kroll, J. H., Donahue, N. M., Jimenez, J. L., Kessler, S. H., Canagaratna, M. R., Wilson, K. R., Altieri, K. E., Mazzoleni, L. R., Wozniak, A. S., Bluhm, H., Mysak, E. R., Smith, J. D., Kolb, C. E., and Worsnop, D. R. Carbon oxidation state as a metric for describing the chemistry of atmospheric organic aerosol. *Nature Chemistry*, 2011, 3, 133–139.

Ng, N. L., Canagaratna, M. R., Jimenez, J. L., Zhang, Q., Ulbrich, I. M., and Worsnop, D. R. Real-time methods for estimating organic component mass concentrations from aerosol mass spectrometer data. *Environmental Science and Technology*, 2011, 45, 910–916.

Ng, N. L., Canagaratna, M. R., Zhang, Q., Jimenez, J. L., Tian, J., Ulbrich, I. M., Kroll, J. H., Docherty, K. S., Chhabra, P. S., Bahreini, R., Murphy, S. M., Seinfeld, J. H., Hildebrandt, L., Donahue, N. M., DeCarlo, P. F., Lanz, V. A., Prevot, A. S. H., Dinar, E., Rudich, Y., and Worsnop, D. R. Organic aerosol components observed in Northern Hemispheric datasets from aerosol mass spectrometry. *Atmospheric Chemistry and Physics*, 2010, 10, 4625–4641.

Peng, Z., and Jimenez, J. L. Modeling of the chemistry in oxidation flow reactors with high initial NO. *Atmospheric Chemistry and Physics*, 2017, 17, 11991–12010.

Simonen, P., Saukko, E., Karjalainen, P., Timonen, H., Bloss, M., Aakko-Saksa, P., Rönkkö, T., Keskinen, J., and Dal Maso, M. A new oxidation flow reactor for measuring secondary aerosol formation of rapidly changing emission sources. *Atmospheric Measurement Techniques*, 2017, 10, 1519–1537.

Suarez-Bertoa, R., Valverde, V., Clairotte, M., Pavlovic, J., Giechaskiel, B., Franco, V., Kregar, Z., and Astorga, C. On-road emissions of passenger cars beyond the boundary conditions of the real-driving emissions test. *Environmental Research*, 2019, 176, 108572.

Timonen, H., Karjalainen, P., Saukko, E., Saarikoski, S., Aakko-Saksa, P., Simonen, P., Murtonen, T., Maso, M. D., Kuuluvainen, H., Bloss, M., Ahlberg, E., Svenningsson, B., Pagels, J., Brune, W. H., Keskinen, J., Worsnop, D. R., Hillamo, R., and Rönkkö, T. Influence of fuel ethanol content on primary emissions and secondary aerosol formation potential for a modern flex-fuel gasoline vehicle. *Atmospheric Chemistry and Physics*, 2017, 17, 5311–5329.

Supplementary Material B

Fuel Properties

Table SM2. Main Physiochemical Properties of the Test Fuels

Property	Test Method	E10	E10HA	E78
Research Octane Number	ASTM D2699	92.1	93.5	
Motor Octane Number	ASTM D2700	84	83.9	
Octane Rating		88.1	88.7	
Sulfur Content (wt. %)	ASTM D5453	8	7.2	3
Total Aromatics (vol %)	ASTM D5769	28.1	36.7	5.5
C6 Aromatics (Benzene) (vol %)	ASTM D5769	0.599	0.565	0.2
C7 Aromatics (Toluene) (vol %)	ASTM D5769	7.583	9.143	1.4
C8 Aromatics (vol %)	ASTM D5769	6.548	7.266	1.2
C9 Aromatics (vol %)	ASTM D5769	6.124	10.229	1.8
C10+ Aromatics (vol %)	ASTM D5769	5.56	7.023	0.8
Olefins Content	ASTM D6550	8.498	10.634	1.5
Hydrogen Content (wt. %)	ASTM D5291	13.59	13.21	13.07
Carbon Content (wt. %)	ASTM D5291	82.77	83.19	59.41
Oxygen Content (wt. %)	ASTM D4815	3.63	3.59	27.52
C/H Ratio		6.09	6.297	4.545
Net Heat of Combustion (MJ/Kg)	ASTM D240	41.94	41.65	30.30
Density at 15.56°C (g/cc)	ASTM D4052	0.7494	0.7544	0.7830
RVP at 100°F (psi)	ASTM D5191	8.89	9.39	5.05
Distillation (°C)	ASTM D86			
IBP		35	34.5	49.9
10%		51.7	53.5	71.1
50%		94	96.3	77.4
70%		129.1	130	77.9
90%		163.5	165.9	78.6
95%		179.1	181.8	79.4
FBP		203.5	209.1	168.2
Ethanol Content (vol %)	ASTM D4815	9.86	9.85	78.27

Photooxidation Experiments

The TSAR chamber sampled exhaust from the CVS tunnel through an ejector diluter (nominal dilution ratio of 7:1). In addition, the sample was diluted before TSAR by flows of O_3 and humid air. Mass flow controllers were used to stabilize the flows, and additional dilution air (dilution ratio of 3.4:1) was fed after TSAR to provide suitable sample flows for mAMS and ELPI+. The dilution ratios were verified by propane trace gas measurements. The temperature and RH of the sample were monitored by a RH sensor upstream TSAR. An ozone (O_3) analyzer (2B Dual Beam Ozone analyzer) was used to monitor O_3 concentrations downstream TSAR before and after the UV lights were turned on. In TSAR, the sample was exposed to 254 nm UV radiation, which induced production of OH radicals through the photolysis of ozone in the presence of H_2O. In contrast to previous studies with the TSAR (Simonen et al., 2017; Simonen et al., 2019), for this study the unit was equipped with light-intensity control for the UV lamps. To monitor the light intensity, photodiodes sensitive to visible light were placed close to each UV lamp and their voltages were continuously logged. Background measurements were executed before and after each cycle and the mass concentrations born from the oxidation of precursors in the dilution air were found negligible but subtracted from the concentrations measured by ELPI+ and mAMS.

A chemical reaction model was applied to estimate the OH exposure and corresponding photooxidation timescale in TSAR, similarly to Simonen et al. (2017). The model is an adaptation of a model presented for the PAM reactor (PAM users' manual, PAM_chem_v8 by William Brune, https://sites.google.com/site/pamusersmanual/7-pam-photochemistry-model/a-introduction). The model inputs include the measured RH, temperature, and O_3 data as well as the measured concentrations of NOx, CO, and OH reactivity caused by the organic gases. The chemistry of individual organic compounds is not modeled, but instead SO_2 is used as their proxy so that the OH reactivity of SO_2 equals the OH reactivity of the organic gases. To account for the residence time in the TSAR inlet and mixing regions, the concentrations of the precursor gases are corrected with a time convolution function as described by Simonen et al. (2017). NO/NO_2 ratio was not measured directly in this study and thus NO_2 was assumed to comprise 10 percent of NOx in accordance with a previous study by Suarez-Bertoa et al. (2019). In order to calculate the OH reactivity of organic gases, accounting for the different compositions of organic precursors present in the exhaust during tests with varying fuels, it was assumed that the hydrocarbons followed the distributions measured by Timonen et al. (2017) for E10 and E85 fuels during CSUDC and EUDC cycles. The atmospheric ages were calculated in a 1-minute resolution, and cycle averages are shown in Table SM3. Figure SM 13 (A-B) shows the OH exposure as a function of time for the LA92 (A) and US06 (B) cycles, respectively.

Table SM3. Sample Conditions Together with OH Exposures and Atmospheric Age Averaged for the LA92 and US06 Cycles

Cycle/Fuel	RH (%)	Temperature (°C)	UV Actinic Flux (cm^{-2} s^{-1})	Initial O_3 (ppm)	OH Exposure (molecule $cm^{-3}s$)	Atmospheric Age (days)
LA92 Cycle						
E10	24.3	20.1	1.92E+15	38.4	9.02E+11	7.0
E10HA	24.6	19.8	1.92E+15	33.8	8.47E+11	6.5
E78	26.7	20.0	1.92E+15	37.0	9.59E+11	7.4
US06 Cycle						
E10	27.4	20.1	1.92E+15	36.6	8.20E+11	6.3
E10HA	28.4	19.7	1.92E+15	34.2	8.45E+11	6.5
E78	28.1	20.0	1.92E+15	35.1	8.68E+11	6.7

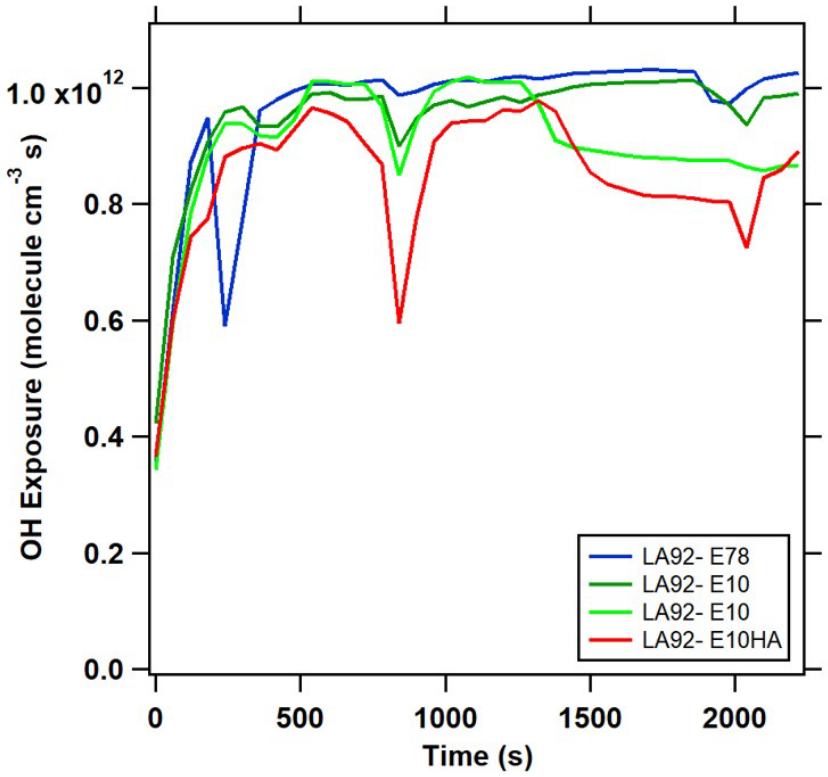

A

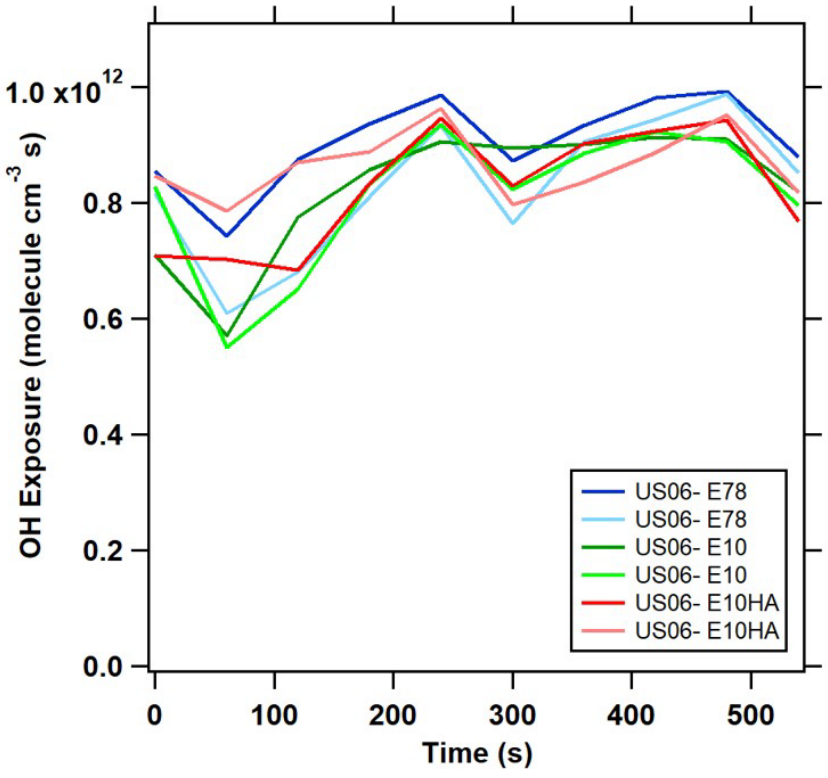

B

Figure SM13 (A-B). Modeled OH exposures for the LA92 (A) and US06 (B) cycles.

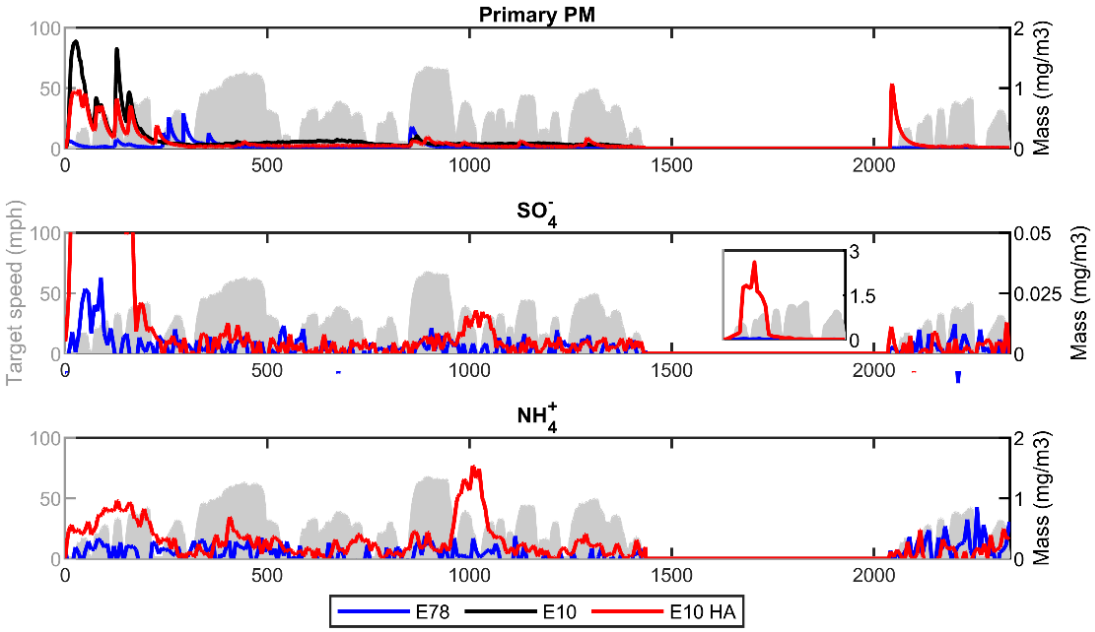

Note: For E10, only primary PM data are available during the cold-start and hot-running phases of the cycle.

Figure SM14. Primary PM, SO_4^-, and NH_4^+ concentrations over the LA92 cycle with E78, E10, and E10HA fuels.

Table SM4. Emission Factors for Aged PM, NO_3, SO_4, HOA, and SOA for PFI-FFV Operated with E10, E10HA, and E78 Blends over the LA92 and US06 Cycles

LA92			
(mg/mi)	**E10**	**E10HA**	**E78**
aged PM, cold-start	271.72	387.28	47.55
aged PM, weighted	76.41	41.64	7.24
NO_3, cold-start	—	7.09	0.86
NO_3, weighted	—	1.62	0.47
SO_4, cold-start	—	1.46	0.02
SO_4, weighted	—	0.08	0.00
NH_4, cold-start	—	1.93	0.32
NH_4, weighted	—	0.55	0.09
HOA, cold-start	—	0.86	0.12
HOA, weighted	—	0.06	0.01
SOA, cold-start	—	118.74	10.84
SOA, weighted	—	6.93	0.56
US06			
(mg/mi)	**E10**	**E10HA**	**E78**
aged PM	51.41	42.19	23.76
NO_3	4.20	2.45	1.55
SO_4	0.02	0.02	0.01
NH_4	1.39	0.86	0.50
HOA	0.02	0.02	0.01
SOA	1.72	2.60	0.49

Note: — means not applicable.

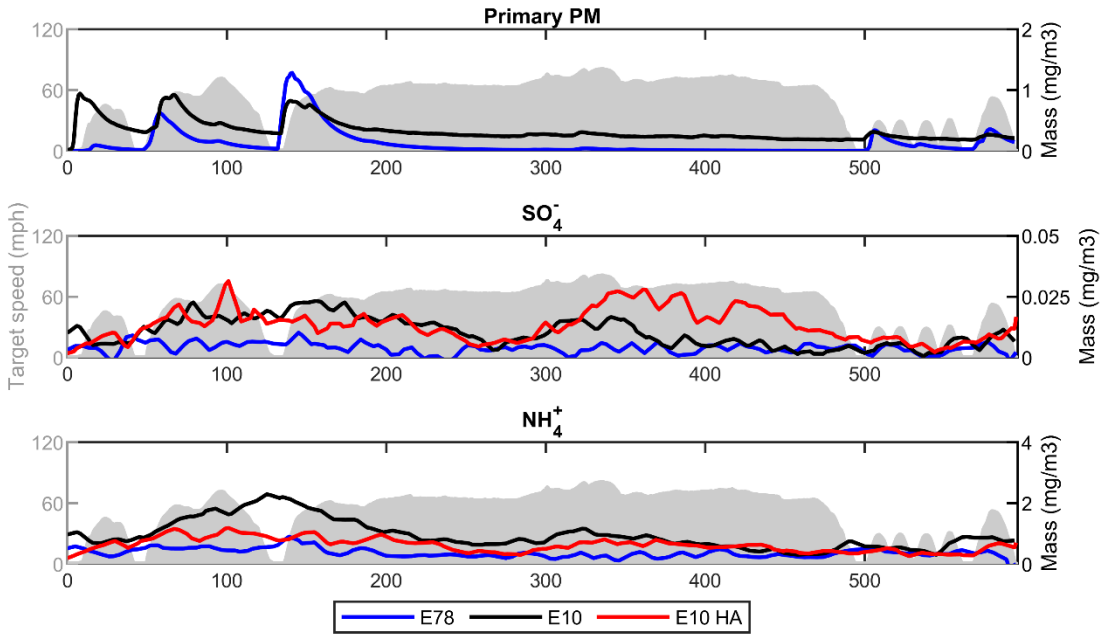

Figure SM15. Primary PM, SO_4^-, and NH_4^+ concentrations over the US06 cycle with E78, E10, and E10HA fuels.

Table SM5. Aromatic Composition of the Different Fuels and the Corresponding SOA Yield Based on Family Class and Carbon Number (adopted from Gentner et al., 2012)

E78	Carbon #	wt. %	SOA Yield	Weighted Yield
Mono-Aromatics	6	0.189	0.14	2.65E-02
	7	1.574	0.083	1.31E-01
	8	1.297	0.048	6.23E-02
	9	2.009	0.077	1.55E-01
	10	0.726	0.12	8.71E-02
	11	0.165	0.15	2.48E-02
	12	0.05	0.19	9.50E-03
Naphthalenes	10	0.007	0.17	1.19E-03
Naphtheno/Olefino-Benzs	9	0.049	0	0.00E+00
	10	0.173	0.17	2.94E-02
	11	0.004	0.23	9.20E-04
				Sum
				0.53
E10				
Mono-Aromatics	6	0.705	0.14	9.87E-02
	7	8.803	0.083	7.31E-01
	8	7.6	0.048	3.65E-01
	9	7.144	0.077	5.50E-01
	10	5.154	0.12	6.18E-01
	11	1.079	0.15	1.62E-01
	12	0.318	0.19	6.04E-02
	13	0.002	0.26	5.20E-04
Naphthalenes	10	0.156	0.17	2.65E-02
	11	0.407	0.23	9.36E-02
	12	0.16	0.28	4.48E-02
Naphtheno/Olefino-Benzs	9	0.216	0	0.00E+00
	10	1.098	0.17	1.87E-01
	11	0.052	0.23	1.20E-02
	12	0.048	0.28	1.34E-02
				Sum
				2.96
E10HA				
Mono-Aromatics	6	0.654	0.14	9.16E-02
	7	10.436	0.083	8.66E-01
	8	8.291	0.048	3.98E-01
	9	11.737	0.077	9.04E-01
	10	5.798	0.12	6.96E-01
	11	1.792	0.15	2.69E-01
	12	0.562	0.19	1.07E-01

	13	0.002	0.26	5.20E-04
Naphthalenes	10	0.213	0.17	3.62E-02
	11	0.504	0.23	1.16E-01
	12	0.199	0.28	5.57E-02
Naphtheno/Olefino-Benzs	9	0.278		0.00E+00
	10	1.678	0.17	2.85E-01
	11	0.093	0.23	2.14E-02
	12	0.081	0.28	2.27E-02
				Sum
				3.87

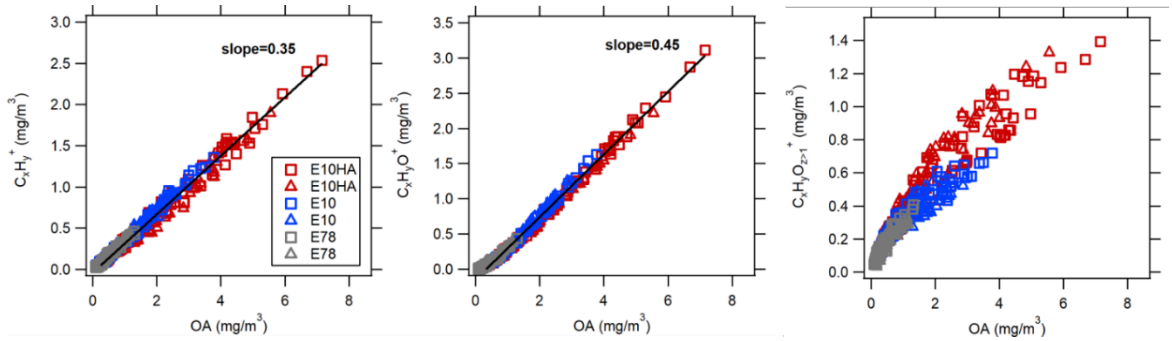

Figure SM16. Relative contribution of different ion families to total OA for the US06 cycle using E10, E10HA, and E78 fuels.

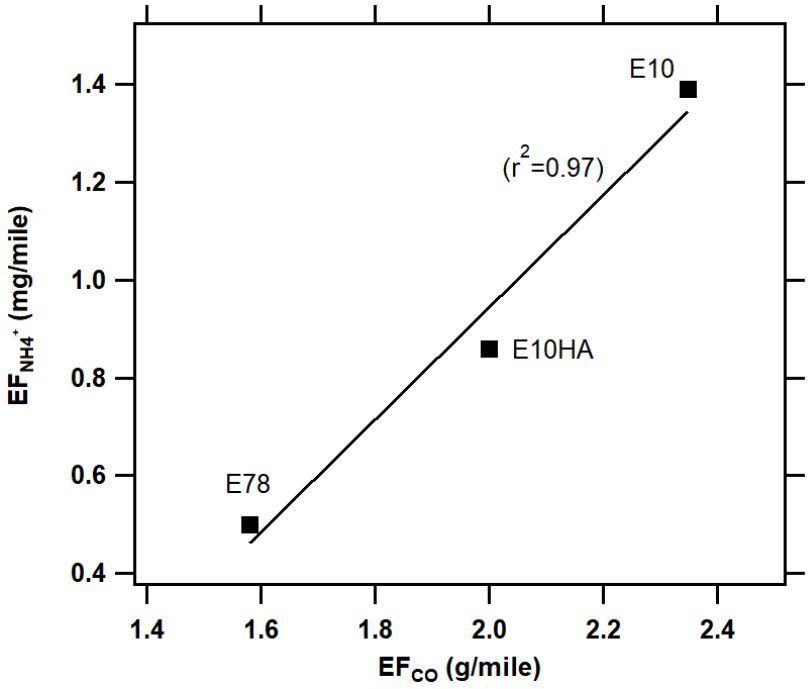

Figure SM17. Correlation between emission factors of NH_4^+ and CO for different fuels over the US06 cycles.

References

Gentner, D. R., Isaacman, G., Worton, D. R., Chan, A. W. H., Dallmann, T. R., Davis, L., Liu, S., Day, D. A., Russell, L. M., Wilson, K. R., Weber, R., Guha, A., Harley, R. A., and Goldstein, A. H. Elucidating secondary organic aerosol from diesel and gasoline vehicles through detailed characterization of organic carbon emissions. Proceedings of the National Academy of Sciences of the United States of America, 2012, 109, 18318–18323.

Simonen, P., Kalliokoski, J., Karjalainen, P., Rönkkö, T., Timonen, H., Saarikoski, S., Aurela, M., Bloss, M, Triantafyllopoulos, G., Kontses, A., Amanatidis, S., Dimaratos, A., Samaras, Z., Keskinen, J., Dal Maso, M., and Ntziachristos, L. Characterization of laboratory and real driving emissions of individual Euro 6 light-duty vehicles—Fresh particles and secondary aerosol formation. *Environmental Pollution*, 2019, 255, 113175.

Simonen, P., Saukko, E., Karjalainen, P., Timonen, H., Bloss, M., Aakko-Saksa, P., Rönkkö, T., Keskinen, J., and Dal Maso, M. A new oxidation flow reactor for measuring secondary aerosol formation of rapidly changing emission sources. *Atmospheric Measurement Techniques*, 2017, 10, 1519–1537.

Suarez-Bertoa, R., Valverde, V., Clairotte, M., Pavlovic, J., Giechaskiel, B., Franco, V., Kregar, Z., and Astorga, C. On-road emissions of passenger cars beyond the boundary conditions of the real-driving emissions test. *Environmental Research*, 2019, 176, 108572.

Timonen, H., Karjalainen, P., Saukko, E., Saarikoski, S., Aakko-Saksa, P., Simonen, P., Murtonen, T., Maso, M. D., Kuuluvainen, H., Bloss, M., Ahlberg, E., Svenningsson, B., Pagels, J., Brune, W. H., Keskinen, J., Worsnop, D. R., Hillamo, R., and Rönkkö, T. Influence of fuel ethanol content on primary emissions and secondary aerosol formation potential for a modern flex-fuel gasoline vehicle. *Atmospheric Chemistry and Physics*, 2017, 17, 5311–5329.